Fluid-Structure Dynamics for Extreme-Scale Offshore Wind Energy and Riverine Energy Harvesting

---

A Dissertation Presented to

The Faculty of The School of Engineering and Applied Science

University of Virginia

In Partial Fulfillment

of the Requirements for The Degree of

Doctor of Philosophy

in Mechanical and Aerospace Engineering

By

Michael Jeong

December 2024

APPROVAL SHEET

This

Dissertation

is submitted in partial fulfillment of the requirements
for the degree of

Doctor of Philosophy

Author: Michael Wu Jeong

This Dissertation has been read and approved by the examing committee:

Advisor: Eric Loth

Advisor:

Committee Member: Daniel Quinn

Committee Member: Hilary Bart-Smith

Committee Member: Joseph Zhu

Committee Member: Thomas Ward

Committee Member: Matthew Reidenbach

Committee Member:

Accepted for the School of Engineering and Applied Science:

Jennifer L. West, School of Engineering and Applied Science

December 2024

Abstract

As the need for energy increases globally, renewable energy has become the fastest growing segment of the energy sector, providing cleaner sources of energy that will have reduced impact on escalating environmental concerns. To achieve a carbon-free electric grid, no single form renewable energy can be relied upon due to the intermittency of renewables. To that end, two forms of renewable energy are explored to address energy generation capabilities at large and small scales.

The abundance of wind resources offshore and the decreasing costs associated with larger wind turbines supports the development of offshore turbines at unprecedented scales. Such large rotors pose structural challenges due the extreme size and weight the blades. A novel methodology for designing extreme-scale rotors was developed to optimize aerodynamics for maximum power production and minimum rotor weight and cost. The approach consists of three stages used to computationally design blade and rotor geometry while considering aeroelastic effects and steady state performance. To achieve this, a design space was identified based on novel empirical models of 2-D airfoil characteristics at extreme Reynolds numbers to help determine ideal lift coefficient and chord distributions for blades at these very large scales. The method was then applied to produce a 25 MW rotor, one of the largest ever to be designed.

Variable pitch capabilities are another crucial design consideration to maximize extreme-scale turbine performance. These pitch systems must be able to sufficiently actuate very long and heavy blade to handle the high wind speeds and turbulence levels expected offshore. However, a generalized approach for sizing the peak and average power of blade pitch systems is not publicly available. Thus, a method for estimating peak pitch requirements was developed herein and applied to reference turbines ranging from 5 MW to 50 MW in terms of rated power. In doing so, scaling laws were determined to estimate maximum blade root pitching moments, required actuator torque, and pitch power consumed based on the product of blade mass and average blade chord length. The results indicate that wind speeds slightly above rated conditions are the primary drivers for pitch system power requirements.

Small scale hydrokinetic devices can be installed in riverine environments to generate relatively consistent power from the incoming flow. However, conventional rotary turbines post threats to marine wildlife and are not ideal for operating in shallow riverine depths and handling seasonal changes in flow conditions. Oscillating hydrofoil systems can address these issues but require further development to improve the understanding of flow physics that lead to high power generation efficiencies. Experiments were conducted to investigate the impact of freestream turbulence on hydrofoil performance for a single hydrofoil at laboratory scale. The results indicate that elevated turbulence levels actually improve hydrofoil kinematics, forces, and thus power. A more in-depth analysis of the flow physics associated with this efficiency benefit is recommended for future work.

The relatively shallow depths of rivers also present an opportunity to further increase oscillating hydrofoil efficiency through flow confinement effects. A 2-D numerical approach was validated and utilized to assess the impact of horizontal confinement using a vertically stacked dual hydrofoil configuration. Both laboratory scale and field scale Reynolds numbers were considered and the results indicated that the confinement due to interactions between the hydrofoils and the free surface and riverbed provide significant enhancement of hydrodynamic efficiency. Confinement between two hydrofoils provide a smaller benefit, and, surprisingly, sometimes an efficiency reduction. Additional work is recommended to account for three-dimensional effects that are expected to negatively impact hydrofoil performance.

Acknowledgements

First and foremost, I want to thank my advisor Dr. Eric Loth for all of his support and guidance, not only throughout the course of my Ph.D., but also as an undergraduate student as well. I am incredibly fortunate to have had the opportunity to join his group back in 2019 and develop my interests in research and renewable energy throughout both my undergraduate and graduate careers. His expertise and experience as a researcher, a mentor, and a leader has been paramount in my successes as a student over the last several years. I would not be in the position I am today without his efforts.

Special thanks to Dr. Chris Qin, who has been a source of direction and knowledge throughout the full course of my Ph.D., especially during the pandemic when I first started graduate school. I also want to thank Dr. Edem Tetteh, who was instrumental in introducing me to research and Dr. Loth's group during my time as an undergraduate. I want to express gratitude to my committee members who have provided valuable feedback in improving my research skills and dissertation at each stage of my Ph.D. Furthermore, I would like to thank all of my FRIL lab mates (Kevin, De'Ajree, Cesar, Juliet) as well as the rest of the students in MEC 116. I have learned much from them and will treasure the times I've spent with them both inside and outside of the lab.

I also want to thank all of the team members of the Segmented Outboard Articulating Rotor (SOAR) and the Bio-Inspired Renewable Energy (BIRE) projects. From the SOAR project, a specific thanks to Dr. Michael Selig for his guidance on wind turbine aerodynamic design, Nick Johnson for his contributions on WISDEM blade structural optimization, and Dr. Lucy Pao, Manuel Pusch, and Mandar Phadnis for their contributions on wind turbine pitch control requirements. From the BIRE project, thanks to Dr. Hilary Bart-Smith for her leadership as well as Dr. Joseph Zhu, De'Ajree Branch, and Ethan Green for the many hours of support and troubleshooting on the hydrofoil experiments. Additionally, I want to acknowledge Dr. Keith Moored and his group at Lehigh University and Giorgio Bacelli at Sandia National Laboratories. Lastly, thanks to the members of the ARPA-E team, without whom neither of these projects would be possible. The research in this dissertation is much more impactful because the assistance from all.

Finally, my deepest gratitude to my friends and family who have been endlessly supportive throughout this journey. I truly appreciate everyone who has been there through both the challenges and celebrations. To my undergraduate friends, although you have all now long left UVA, your continued support has not gone unnoticed. To those I met as a graduate student, thank you for making these years all the more special. To my sister Emily, thanks for always being someone to confide in and sorry for the holidays (albeit just a couple) that I missed during graduate school. To my parents Jong-Hyeon Jeong and Chang-Sook Hong, your advice and encouragement during difficult periods made this dissertation possible. Thank you both for your love and support.

Table of Contents

List of Figures

List of Tables

Chapter 1

Introduction

1.1 Background and Motivation

As the need for energy increases globally, renewable energy has become the fastest growing segment of the energy sector, providing cleaner sources of energy that will have reduced impact on escalating environmental concerns. From a 2017 report by the International Energy Agency, in order to prevent global temperatures from increasing beyond 2°C compared to those from pre-industrialization (up to about 1900), approximately a 70% reduction of annual CO_2 emissions is predicted to be necessary by the year 2060 [1]. In the US, there has been a steady growth of renewable energy generating capacity over the past few decades with total capacity of around 300 GW as of 2024 with expected growth to exceed 400 GW by 2025 [2]. In 2024, this corresponds to about 21% of total utility scale energy generation comes from renewable sources, primarily from wind, hydro, and solar energy [3]. However, renewable energy sources face the disadvantage of intermittency when compared to natural gas and coal. Thus, energy harvesting from a wide range of resources should be explored.

Wind energy is currently one of the fastest growing renewable energy sources, currently contributing the largest proportion of renewable energy to the grid [3]. In the US, estimates predicted that 40 GW of offshore wind capacity could be installed by 2035 [4]. Offshore sites provide opportunities for increased energy production as the trends for turbine scale continue to increase in correlation with lower Levelized Cost of Energy (LCOE) [5]. To that end, the average rated power for installed offshore wind turbine in the US has grown by 2 MW from 2022 to 2023 with the introduction of offshore platforms >15 MW [4]. However, the increased energy production associated with extreme scale turbines is not without challenges. Structural limitations emerge due to blades becoming extremely long and heavy. Downwind facing rotors may be one part of the solution as the reduced potential for tower strike can allow for lighter, more flexible blades [6]. However, in designing such rotors, new robust design methods and an improved understanding of extreme scale turbine dynamics are necessary to optimize size, mass, and cost of turbine components.

While addressing rotor design methods aims to optimize the aerodynamic and structural design of extreme scale rotors, the rotor performance requires accurate control to maximally extract power in operation. Given the higher wind speeds, turbulence levels, and blade deflections that extreme scale turbines will experience in offshore sites, installing sufficient control actuation systems is a necessity. Pitch control has been historically used in wind turbine control to adjust the blade angle of attack for two main purposes: maximize lift forces on the blade and thus maximize power production in below rated wind conditions, and limit loads on the turbine structures and generator in above rated wind conditions [7]. Modern turbines use Individual Pitch Control (IPC) which allows for the pitch of each blade to be controlled separately [8, 9]. To effectively implement pitch control on blades that are longer, more flexible, and heavier than ever before, modern electric pitch systems must provide enough torque to overcome blade pitch inertia and loads while providing suitable control response frequencies. However, in sizing pitch actuation systems for these extreme scale turbines, little work has been done to understand the pitch dynamics that may limit pitch rates and accelerations of highly flexible extreme scale blades.

Although recent wind energy growth is promising for reducing fossil fuel consumption, the reliability of renewable energy generation should be bolstered with other forms of renewable to combat intermittency issues. Environments like rivers provide opportunities for more consistent power delivery to further increase renewable energy capacity at local and global scales. While turbine-based energy systems can also be used in these environments, rotary turbines pose risks to aquatic wildlife due to high tip speeds and can be challenging to deploy due to limited water depths in certain riverine environments [10, 11]. In such environments, oscillating hydrofoil systems inspired by highly efficient biological swimmers appear to be better suited [12]. These systems operate based on unsteady lift generated from the flow of the river to vertically displace a hydrofoil in an oscillatory motion by actively controlling angle of attack. Unlike hydrokinetic rotary turbines, such systems have lower tip speeds that result in minimally invasive devices and have an adaptable swept area that can handle seasonal variation in riverine flows. Despite promising research on oscillating hydrofoil systems, more work is needed to develop commercially viable systems.

To optimize the power generating performance of an oscillating hydrofoil system, parameters that influence and potentially increase hydrodynamic efficiency must be studied. A primary consideration is the flow conditions of riverine environments. Real world oscillating hydrofoil systems must deal with turbulence and shear and the implications of turbulence on power generation efficiency have yet to be published. While various studies have performed numerical simulations of flapping hydrofoils for energy production, only steady uniform flows have been used [13, 14]. Experimentally, much of the literature investigates hydrofoil performance under fully prescribed kinematics, meaning that the vertical displacement (heave) and pitch angle trajectories are defined mathematically [15]. Although fully prescribed kinematics provides a straightforward approach to understanding the impacts of various kinematic parameters on efficiency, in practice these systems require the heave degree of freedom to operate passively to net extract power from the flow (known as semi-passive or fully-passive systems) [16, 17].

There are a very limited number of studies that have considered semi-passive systems experimentally [12] and no studies (numerical or experimental) have yet been published on the impact of freestream turbulence on oscillating hydrofoil turbine performance.

In addition to freestream turbulence, flow confinement due to shallow riverine depths is another opportunity to improve power generation efficiency. Schooling fish have been shown to use ground effects to improve swimming efficiency [18]. Similarly, configurations of multiple hydrofoils can be considered to enhance performance. While many studies explore tandem configurations for two hydrofoils (one foil downstream of another) [19–21], vertically arranging two hydrofoils that oscillate out-of-phase can increase local flow confinement by effectively decreasing gaps between the hydrofoil and the free surface, riverbed, and the two foils. Vertically stacking of out-of-phase hydrofoil can also help balance the net force on a given foundation. Studies on confinement effects for power generating hydrofoils are currently limited and focus on single or tandem hydrofoil performance [22–25]. Additionally, these studies consider Reynolds numbers (Re) less than 100,000 (often as low as Re = 1100) whereas field scale Re are more likely in the range of 300,000 – 600,000 [10, 26]. No previous published studies have investigated vertically stacked out-of-phase dual hydrofoils, despite the practical benefits of such arrangements. Thus, such work is of strong interest to further improve efficiencies and thus energy extraction at real world scales.

1.2 Objectives

This dissertation attempts to expand upon the existing knowledge of these two renewable energy forms (wind energy and hydrokinetic energy) to address important energy harvesting challenges that can contribute to both global and local needs. The research presented on wind energy (Chapters 2 and 3) focuses on extreme scale wind turbine design while the research presented on oscillating hydrofoils (Chapters 4 and 5) focuses on improving hydrodynamic efficiency by investigating the fluid-structural interactions between hydrofoils and the incoming flow. Both computational and experimental methods are employed to accomplish this research. The specific aims of the following chapters are as follows:

Chapter 2: Develop a computational rotor design methodology for extreme scale wind turbines with the primary focus on maximizing power production through optimizing blade and rotor fluid/structure interaction and apply this methodology to design a 25 MW downwind rotor.

Chapter 3: Develop an approach to estimate peak pitch actuation requirements for extreme scale turbines using an integrated wind turbine simulation code and apply this method to estimate requirements for turbines ranging from 5 MW to 50 MW.

Chapter 4: Investigate the impact of freestream riverine turbulence on hydrodynamic efficiency of a single oscillating hydrofoil with experiments performed in a laboratory scale water channel.

Chapter 5: Numerically investigate the benefits of confinement on dual and single oscillating hydrofoil efficiency at field scale Reynolds numbers using two-dimensional Navier-Stokes simulations.

Chapters 2 – 5 are written as individual research articles and include a review of relevant literature at the beginning of each chapter. Finally, Chapter 6 presents conclusions, contributions of this dissertation, and recommended future work.

Chapter 2

Aerodynamic Rotor Design for a 25 MW Offshore Downwind Turbine

Abstract

Continuously increasing offshore wind turbine scales require rotor designs that maximize power and performance. Downwind rotors offer advantages in lower mass due to reduce potential for tower strike, and this is especially true at large scales, e.g., for a 25 MW turbine. In this study, three 25 MW downwind rotors, each with different prescribed lift coefficient distributions were designed (chord, geometry, and twist) and compared to maximize power production at unprecedented scales and Reynolds numbers, including a new approach to optimize rotor tilt and coning based on aeroelastic effects. To achieve this objective the design process was focused on high power coefficients, while maximizing swept area and minimizing blade mass. Maximizing swept area was achieved using pre-cone and shaft tilt angles to ensure the aeroelastic orientation when the blades point upwards was nearly vertical at nearly rated conditions. Maximizing the power coefficient was achieved by prescribing axial induction factor and lift coefficient distributions which were then used as inputs for an inverse rotor design tool. The resulting rotors were then simulated to compare performance and subsequently optimized for minimum rotor mass. To achieve these goals, a high Reynolds number design space was developed using computational predictions as well as new empirical correlations for flatback airfoil drag and maximum lift. Within this design space, three rotors of small, medium and large chords were considered for clean airfoil conditions (effects of premature transition were also considered but did not significantly modify the design space). The results indicated that the medium chord provided the best performance, producing the highest power in Region 2 from simulations while resulting in the lowest rotor mass, both of which support minimum LCOE. The methodology developed herein can be used for other extreme-scale (upwind and downwind) turbines.

2.1 Introduction

As the need for energy increases globally, renewable energy has become the fastest-growing segment of the energy sector, providing cleaner sources of energy that will have less impact on growing environmental problems. Wind energy is anticipated to become one of primary renewable energy sources. In 2008, the Department of Energy set a target for wind energy to contribute to 20% of U.S. energy by 2030 [27]. More recently in 2021, the Biden Administration announced a national offshore wind target of 30 GW by 2030 [28]. Currently, the largest commercial wind turbines are rated at 14 MW [29], but trends are going toward continuously increasing scales. Extreme-scale offshore wind turbines present an opportunity for even more energy production as offshore wind is more abundant than land-based wind. Increasing turbine sizes to extreme-scales also allow for more energy capture while having less levelized cost of energy (LCOE) [5, 27]. Downwind rotors offer advantages in lower mass due to reduce potential for tower strike, especially at the extreme-scales used in this study [6]. Offshore wind energy presents good opportunities to increase the amount of renewable energy in the grid and has been shown to have very suitable environments to implement in areas like the United States and Europe [12, 31]. However, these extreme-scales also pose certain structural limitations in blade loads and deflections due to longer blades and higher offshore wind speeds and turbulence. Using conventional rotor design methods for extreme-scale turbines could result in heavy rotors that negatively impact turbine costs and thus require a different approach to optimize the mass, size, and cost of turbine components. Therefore, robust design methods and an understanding of the dynamics of such extreme-scale wind turbines are necessary.

Various methods exist to design wind turbine rotors. Scaling has been used in the design of research turbines by using scaling factors to upscale existing smaller turbine designs. At the 25 MW scale, the SUMR-25 two-bladed downwind offshore coned rotor project used technological scaling to scale up the 13.2 MW SUMR-13 rotor in the first of three rotor versions created within that study [32]. Scaling also was used to design a 100 m blade by Sandia National Laboratories using a structural approach to scale up blade geometry and structural properties [33]. Rotors can also be designed without scaling by creating blade geometries (chord and twist distributions) that achieve a desired aerodynamic performance. A direct design approach, sometimes called a design-by-analysis approach, generates a blade geometry first which is then analyzed for performance and subsequently adjusted in an iterative process until a blade geometry that achieves the desired performance emerges. This approach, although often used in the past, is computationally involved and inefficient compared to the inverse design approach that is more commonly used now. With an inverse design approach, parameters for aerodynamic performance such as airfoil characteristics, tip-speed ratio (λ), axial induction factor (a), aerodynamic power (P), and rotor geometry are used as inputs instead of the blade geometry. The blade geometry can then be determined to achieve these desired parameters, eliminating the need to analyze a blade geometry each iteration as done in the direct design approach and saving computation resources. Using an inverse design approach is better suited for designing around a desired peak power production. The inverse approach has been used in the design of both research and commercial wind turbines and is used in this study. This was accomplished using the multipoint inverse design tool PROPID [34–36]. PROPID has been used for extreme scale rotor design in the SUMR-13i offshore rotor by Ananda *et al*. and in the aerodynamic redesign of the SUMR-25 rotor as part of the study by Qin et al. [32, 37].

Provided that the resulting rotor performs as desired, structural optimization can be performed to minimize mass and cost, and to meet load requirements. The National Renewable Energy Laboratory (NREL) has developed the Wind-Plant Integrated System Design & Engineering Model (WISDEM) framework that is capable of modeling entire turbines and turbine farms [38]. The WISDEM framework is applied in this study to optimize the blade structure given the blade geometry designed in PROPID. Higher fidelity simulations are also useful at this stage to predict the dynamic response and performance of the rotor. The OpenFAST wind turbine simulation framework developed by NREL is a tool that can simulate turbine dynamics using various computational modules for aerodynamics, hydrodynamics, controls, and structural dynamics [39]. Such higher fidelity aeroelastic simulations can provide insight into the loading and deflections a rotor may undergo which can inform rotor geometry design decisions like pre-cone and shaft tilt angles to maximize swept area and thus power production. Qin *et al*. performed OpenFAST simulations on the redesigned SUMR-25 rotor following a PROPID design phase [32]. Similarly, in this study, OpenFAST simulations of the resulting PROPID designs were run to investigate aeroelasticity.

Airfoil selection for wind turbines is another important part of the design process to maximize rotor performance. Ananda *et al*. used PROFOIL to create the F1 family of airfoils ranging from 18%–48% thickness [37]. These airfoils were based on a design for a 13.2 MW turbine which provide geometry as a function of the non-dimensional rotor radius (r/R). Characteristics of the F1 airfoils are shown below in Figure 2-1 and Table 2-1 at the airfoil design Reynolds number (Re) for the present 25 MW turbine, based on chord length and the relative upstream velocity (based on the combined freestream and rotational components) where the design value is based on rated conditions (to be described further in Section 2.2). As these airfoils move outboard (increasing r/R), they have increased aerodynamic efficiency as demonstrated by higher maximum lift-to-drag ratios $(L/D)_{max}$, as noted in Table 2-1. However, as these airfoils move inboard (decreasing r/R), they have increased thickness-to chord ratios (t_{max}/c), which results in increased maximum lift coefficients ($C_{l,max}$) at high angle of attack as noted in Figure 2-1. In addition, the inboard airfoils also have increased camber which results in higher lift coefficients at zero angle of attack (C_{l0}) as noted in Figure 2-1 and Table 2-1. Notably, the airfoil shapes for r/R <0.55 are flatback airfoils. This F1 family of airfoils is also applied in this study for a 25 MW turbine (resulting in larger

Reynolds numbers) but with a more formalized optimization based on both aerodynamics and structures, including considering aeroelastic deflections for rotor tilt and coning.

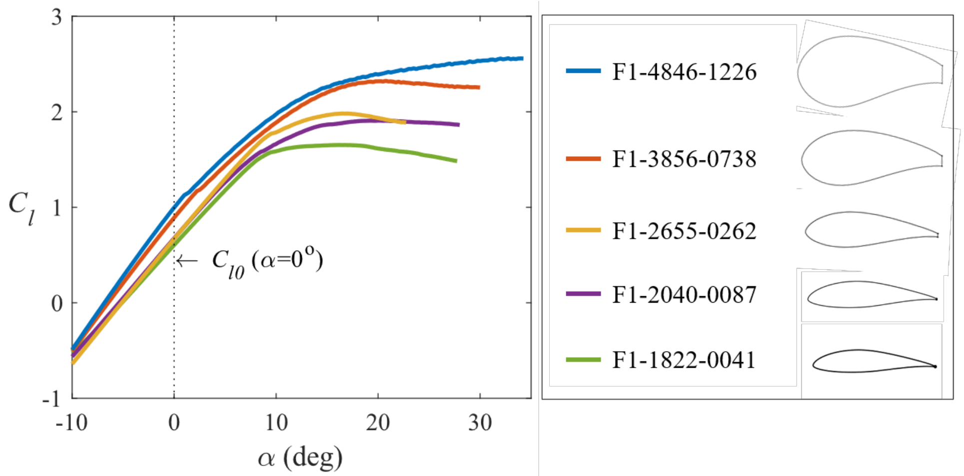

Figure 2-1. XFOIL lift curve predictions for the F1 family of airfoils at Reynolds numbers listed in Table 2-1 at design conditions of the present 25 MW rotor further described in Section 2.2.

Table 2-1. F1 airfoil geometries and XFOIL performance characteristics at design Re for the 25 MW rotor.

Airfoil	r/R	Re	$(L/D)_{max}$	t_{max}/c	t_{TE}/c	t_{TE}/t_{max}	C_{l0}
F1-4846-1226	0.25	11.0×10^6	67.5	48.46%	12.26%	0.253	0.997
F1-3856-0738	0.35	11.8×10^6	91.1	38.56%	7.38%	0.191	0.781
F1-2655-0262	0.55	13.0×10^6	172.3	26.55%	2.62%	0.099	0.673
F1-2040-0087	0.75	14.3×10^6	199.7	20.40%	0.87%	0.044	0.640
F1-1822-0041	0.95	12.3×10^6	198.2	18.22%	0.41%	0.023	0.605

Flatback airfoils have been shown to provide both structural and aerodynamic benefits for larger wind turbine blades near the blade root [40]. The larger cross sections allow for more structural support, and thicker trailing edges reduce premature boundary layer separation, giving flatback airfoils an increased maximum lift coefficient ($C_{l,max}$). For the purpose of designing rotors, the airfoil characteristics of flatback airfoils are used in tools like PROPID in order to achieve the prescribed aerodynamic design parameters like lift coefficient distribution and axial induction factor. These airfoil characteristics can be obtained through numerical tools. The airfoil analysis code XFOIL is used for this purpose in this study [41, 42]. However, numerically derived 2-D airfoil characteristics of flatback airfoils have been shown to be lack accuracy. XFOIL has been found to mispredict lift and drag coefficients, particularly with the flatback airfoils that are used near the blade root [37, 43]. Similarly, 2-D Reynolds-averaged Navier-Stokes (RANS) and unsteady RANS simulations of flatback airfoils have been shown to overpredict maximum lift coefficients and both over- and underpredict drag coefficients which may be attributed to inaccurate modelling of unsteady flow in the wake of the thick trailing edge in 2-D simulations using conventional turbulence models [44–46]. For a robust aerodynamic design, numerically derived airfoil characteristics should be validated using comparable high Reynolds number experimental data to ensure design parameters are realistic. Without such considerations, rotor designs in real operation could lead to shortfalls in performance. Thus, considering adjustments to numerical airfoil characteristic data is important for the aerodynamic design of physically realizable rotors.

This paper discusses the aerodynamic design of a 25 MW offshore downwind wind turbine rotor with 165 m long blades. The objective of maximizing power production was achieved by maximizing swept area and power coefficient (C_P) while providing experimental validation of design choices. This validation was performed by developing a new empirical correlation to correct numerical airfoil data from XFOIL using experimental flatback airfoil data. The corrected XFOIL data was used to create a design space for prescribing realistic lift coefficient distributions for extreme-scale turbines. Three lift coefficient distributions were then chosen and used to design three different rotors using PROPID, each with different resulting chord (c) and twist (θ) distributions. The performance of each rotor was then assessed using OpenFAST [39] and the WISDEM framework [38] to select the best design. Aeroelastic effects on these extreme scale rotors were also explored.

This paper is the first to present a power-maximizing aerodynamic design for a highly flexible 25 MW rotor that uses experimental flatback airfoil characteristics to consider the high Reynolds number effects that have big implications for rotor design at such extreme scales. This study also considers blade flexibility and tip deflections to prescribe rotor pre-cone and shaft tilt angles to further maximize power production, a strategy not considered in most aerodynamic designs. This study is also one of the first to then analyze the resulting rotor designs using high-fidelity simulations and structural optimization tools to provide more useful predictions of rotor performance and cost of rotors that were aerodynamically designed. Such considerations of scale and blade flexibility are not often seen in aerodynamic designs but are critical for extreme-scale turbine operation. The combination of tools and analyses used in this study provides a better understanding of the design parameters and dynamics of extreme-scale wind turbines and a novel framework for designing these turbines that is a crucial step in the development of offshore wind technology. The following sections will discuss the design methods and considerations as well as the designed rotor performance using numerical simulations.

2.2 Design methodology

The blade design process began with determining the main design parameters: rotor size, design λ, axial induction factor, and airfoils. Once the parameters were chosen, PROPID was used to design the rotor geometries. A total of three different blades were designed. These rotor geometries were then analyzed in

OpenFAST to study the predictions under steady wind conditions. In the last step, WISDEM was used to minimize blade mass while meeting critical design load cases for each design. This section will discuss the computational tools and the design parameters selected to design the rotors in this study.

2.2.1 Computational tools

The PROPID program is a tool for designing and analyzing horizontal axis wind turbines (HAWTs) [34–36]. It incorporates a multipoint inverse method that allows the user to specify various desired performance characteristics as input and converge on an outer blade geometry (blade chord length and twist distributions) that achieves the specifications using an iterative solver. Performance characteristics and constraints include peak power, axial induction factor distribution (a), lift coefficient distribution (C_l), and rated wind speed. PROPID uses blade-element momentum theory through implementing a modified version of the PROP blade-element momentum code, PROPSH. This inverse method can allow one to achieve a desired rotor design much more productively than via a direct design approach. Note that PROPID only considers rigid blades and therefore doesn't account for blade deflection in its design and analysis of HAWTs. Thus, additional verification of rotor power generation performance should be performed to consider the time-varying dynamics of wind turbine blades under load (i.e. OpenFAST simulations). The internal structural design of blades (shell thickness, spar cap thickness, etc.) is not performed via PROPID (only the blade geometry is designed with the objective of optimizing rigid blade aerodynamics).

Airfoil characteristics are used as an input in the blade design process within PROPID. Given the airfoils used along the blade span, XFOIL was used to predict 2-D lift and drag coefficients [41, 42]. XFOIL data was subsequently processed through the AirfoilPrep preprocessor to create blends of the F1 airfoils and apply 3-D rotational corrections to XFOIL data for PROPID and OpenFAST. AirfoilPrep uses the Du-Selig method for correcting lift and Egger's method for correcting drag [47].

Rotor performance was simulated following the PROPID design stage using OpenFAST, an open-source wind turbine simulation tool developed by NREL [39]. The OpenFAST framework consists of several computational modules coupled to simulate the aerodynamics, hydrodynamics, structural dynamics and controls systems of turbines. Since OpenFAST can to simulate time-varying effects and various degrees of freedom, it can provide high-fidelity predictions of these turbine dynamics. OpenFAST also can to simulate turbines under unsteady wind conditions, making it useful for simulating design load cases (DLC). However, for the simulations performed in this study, the wind conditions used were steady wind conditions. The aerodynamics module used in OpenFAST was Aerodyn14 which uses blade-element momentum theory (using lookup tables for instantaneous blade element forces) for predicting aerodynamic [48].

WISDEM is an open-source integrated system-level design tool, developed by NREL, capable of designing and assessing individual turbines as well as entire wind farms [38]. WISDEM's aerodynamic module is based on blade-element momentum theory. As steady-state models are used in WISDEM, higher fidelity OpenFAST simulations are required for more accurate, time-varying predictions of turbine dynamics. For this study, after separately designing the blade outer mold line using PROPID, WISDEM was used to design and optimize only the internal structures for a fixed blade outer mold line to minimize rotor mass and thus LCOE to also consider the structural design of wind turbine blades following the aerodynamics focus of the PROPID and OpenFAST design stages.

2.2.2 Main design parameters

The goal of this study was to design a downwind extreme scale wind turbine rotor with a rated power of 25 MW. Design parameters in this study were based partially on the V2e 25 MW turbine described in Escalera Mendoza *et al*. [49]. The V2e design process involved several steps, going through aerodynamics, structures, and controls analyses. The parameters used in this study are listed below in Table 2-2.

Table 2-2. Main design parameters for the 25 MW rotors.

Parameter	Value
Rated power	25 MW
Number of blades	3
Tip-speed ratio	9.25
Target induction factor	1/3
Blade length	165 m
Hub radius	6.75 m
Blade root diameter	6.6 m
Pre-cone angle	6.0°
Shaft tilt	6.0°
Airfoil family	F1

A design tip-speed ratio (λ) of 9.25 was chosen based on tip speed limitations of 120 m/s for offshore turbines. For offshore wind turbines where noise considerations are much less restrictive, an aggressive tip speed limit such as 120 m/s may be appropriate and are already being considered as turbines reach these extreme scales [49, 50]. The design axial induction factor was set at the Betz limit of 1/3 along the entire blade span to maximize aerodynamic performance. Blade length and hub radius were based on the rotor sizes previously used in Escalera Mendoza *et al*. [49]. Blade root thickness was assumed to be 4% of the blade length.

Calculating pre-cone angle and shaft tilt angle required consideration of blade tip deflection limits. Using the V2e turbine, the tip deflection margins toward the tower of a downward pointing blade ($\Psi = 180°$)

under the International Electrotechnical Commission (IEC) 61400-1 standard DLC 1.3 (extreme turbulence model) were considered [51]. The IEC standards define the tip deflection limit toward the tower as 0.7×undeflected tip-to-tower distance away from the tower. Using the V2e deflections and the tip deflection definition, the minimum angle of an undeflected blade at $\Psi = 180°$ could be positioned was determined to be 12° from vertical. This angle corresponds to the sum of the pre-cone and shaft tilt angles. Next, to determine the individual pre-cone angle and shaft tilt angles, a swept area maximizing approach was used. The approach was to align an upward-pointing blade ($\Psi = 0°$) vertically during operation. Thus, to achieve an upward vertical blade orientation, a pre-cone angle and shaft tilt angle were each set to 6°. Note these were the pre-cone and shaft tilt angles used in PROPID, which does not consider blade deflections that would deform the blades downwind and decrease swept area during actual operation. A visualization of the rotor geometry can be seen below in Figure 2-2. Adjustments to this are described below in the discussion of OpenFAST simulations where these aeroelastic deflections are modeled. It should be noted that this same optimization of tilt and coning angle based on aeroelastic deflections can also be applied to upwind extreme-scale rotors (which are expected to be similarly flexible).

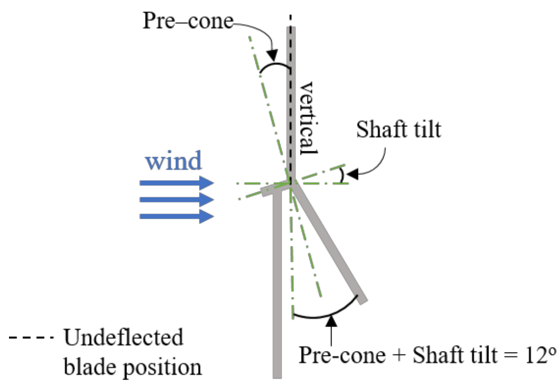

Figure 2-2. Pre-cone angle + shaft tilt configurations for PROPID design assuming rigid blades.

2.2.3 Flatback airfoil aerodynamic coefficient models

PROPID was used to prescribe not only the axial induction factor distribution but also the blade C_l distribution along the span. The prescribed C_l distributions are based on the F1 family of airfoils and the Reynolds numbers at which they are operating for the final blade design. Although experimental data for airfoil characteristics would be useful, obtaining such data at the operational Reynolds numbers for extremely large-scale wind turbines would be difficult. Thus, XFOIL was used to predict F1 airfoil performance at Reynolds numbers shown above in Table 2-1. Interpolated aerodynamic coefficients were also obtained from the XFOIL data with AirfoilPrep to be used along the blade span in between the *r/R* locations of the F1 airfoils [47]. The Reynolds numbers used were based on the rated operating conditions of the V2e blade [49].

However, XFOIL has been shown to underpredict C_d for flatback airfoils and overpredict $C_{l,max}$ [37, 43]. Due to these discrepancies, XFOIL data is not accurate enough to find the stall point for predicting $C_{l,max}$ and C_d characteristics for flatback airfoils used near the blade root. In order to verify the discrepancies found in previous literature, experimental wind tunnel C_d and C_l data were compared to XFOIL data for the DU-97-W-300 airfoil [52–54].

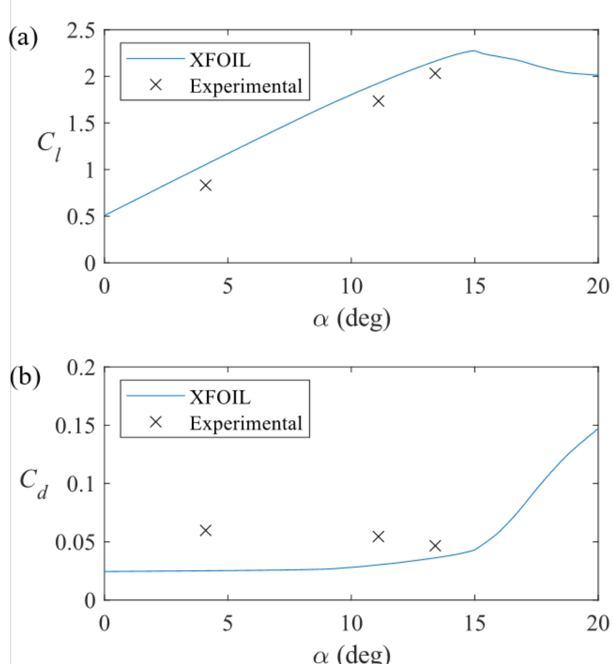

Figure 2-3. Comparison of aerodynamic coefficients between XFOIL and experimental data for the DU97-W-300 airfoil at Re = 3×106 [54] for clean conditions: a) lift; b) drag.

From Figure 2-3, it was observed that XFOIL significantly underestimated C_d by ~60% at low angles of attack. Therefore, experimental wind tunnel data was used to empirically adjust XFOIL data to ascertain more accurate C_l and C_d characteristics. The experimental wind tunnel data for various flatback airfoils are shown in Table 2-3 below [53–57]. These data were taken over various Reynolds numbers ranging from 0.76×10^6 to 4×10^6 and had varying trailing edge thicknesses (t_{TE}/c) ranging from 4.2% to 17.5%. These data can be used in conjunction with XFOIL to account for these over/underpredictions.

Table 2-3. Characteristics of experimental flatback airfoil

Airfoil	t_{max}/c	t_{TE}/c	t_{TE}/t_{max}	Re ($\times10^6$)	C_{l0}	Data reference
DU97-W-300	30%	10%	0.333	3	-	Barone, M., Berg, D. [53, 54]
LI30-FB10	30%	10.6%	0.353	1.5	0.16	Manolesos, M., Voutsinas, S. [55]
FB3500-0050	35%	0.5%	0.014	0.67	0.29	Baker, J., Mayda, E. A., et al. [46]
FB3500-0875	35%	8.75%	0.25	0.67	0.34	Baker, J., Mayda, E. A., et al. [46]
FB3500-1750	35%	17.5%	0.5	0.67	0.51	Baker, J., Mayda, E. A., et al. [46]
DU97-W-300 mod.	27%	10%	0.37	1	0.96	Yilmaz, O., Timmer, W. [56]
FB3500-1750	35%	17.5%	0.5	0.67	0.36	Metzinger, C., Baker, J., et al. [45]
PGW6	27%	4.2%	0.155	3	0.46	Althaus, D. [57]
PGW7	34%	4.2%	0.123	3	0.48	Althaus, D. [57]
PGW6	27%	4.2%	0.155	4	0.48	Althaus, D. [57]
PGW7	34%	4.2%	0.123	4	0.47	Althaus, D. [57]

Experimental flatback airfoil data listed in Table 2-3 was used to see if any correlation could be found to estimate flatback airfoil C_d before stall. The experimental data showed nearly constant C_d for flatback airfoils in this region. Using this assumption, C_d was found to correlate with the trailing edge ratio (t_{TE}/t_{max}), defined as the ratio of airfoil trailing edge thickness (t_{TE}/t_c) to airfoil maximum thickness (t_{max}/t_c), and can be approximately modeled as

$$C_d = 0.227\frac{t_{TE}}{t_{max}} - 0.165 \qquad \text{Eq. 2.1}$$

This correlation is presented in Figure 2-4a. XFOIL data for the F1 family of airfoils is also included in Figure 2-4a showing underprediction of C_d compared to the empirical fit. The F1 airfoils with thinner trailing edges did not seem to show as much C_d underprediction and thus XFOIL C_d adjustments were only added to airfoils with $t_{TE}/t_{max} > 0.11$.

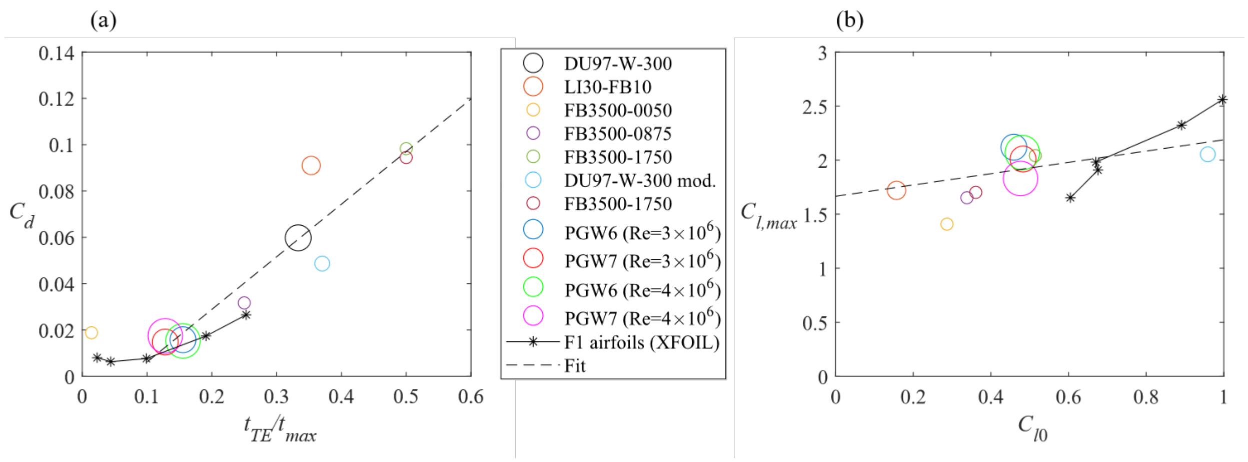

Figure 2-4. Flatback (a) drag and (b) maximum lift coefficient correlations. Larger marker size corresponds to larger Reynolds number. Order of listed airfoils is the same as in Table 2-3.

The experimental data in Table 2-3 was also used to determine an adjustment for overpredicted XFOIL $C_{l,max}$ data. Since $C_{l,max}$ and C_l at zero angle of attack (C_{l0}) depends on airfoil camber, the C_{l0} of the experimental airfoils was used to determine a correlation for $C_{l,max}$ that can be described as:

$$C_{l,max} = 1.67C_{l0} + 0.52 \qquad \text{Eq. 2.2}$$

Again, it was determined for the F1 family of airfoils that the thicker flatback airfoils required adjustment for overpredicted $C_{l,max}$ values, and thus only airfoils with $t_{max}/c > 26.55\%$ (corresponding to the F1-2655-0262 airfoil) were modified.

2.2.4 Lift coefficient design space and distributions

To set the design C_l distribution to use in the rotor design, physically realizable values of C_l along the blade span must be determined for the airfoils. This C_l distribution is limited by a margin below the $C_{l,max}$ of the airfoils to consider deviations in angle of attack due to turbulence. To optimize for aerodynamic performance, the C_l distribution should be as close as possible to $(L/D)_{max}$ curve along the blade span. For the F1 family of airfoils, the $C_{l,max}$ and $(L/D)_{max}$ characteristics were calculated using XFOIL data modified by the high Reynolds number $C_{l,max}$ and C_d adjustments described above. These values were then shifted to create the final design space (shown in green in Figure 2-5b).

The upper limit of the design space is based on $C_{l,max}$ values and the lower limit is based on C_l values at the $(L/D)_{max}$. These values from XFOIL, without any adjustments, can be seen in Figure 2-5a. It can be observed that the flatback airfoils within the inboard 50% of the blade show very high $C_{l,max}$ values as well as low $(L/D)_{max}$ values due to underpredicted C_d before stall. Accounting for C_d and $C_{l,max}$ adjustments, the $C_{l,max}$ vs. $(L/D)_{max}$ curves can be seen in Figure 2-5b, showing decreased $C_{l,max}$ values and increased $(L/D)_{max}$ values for the inboard flatback airfoils.

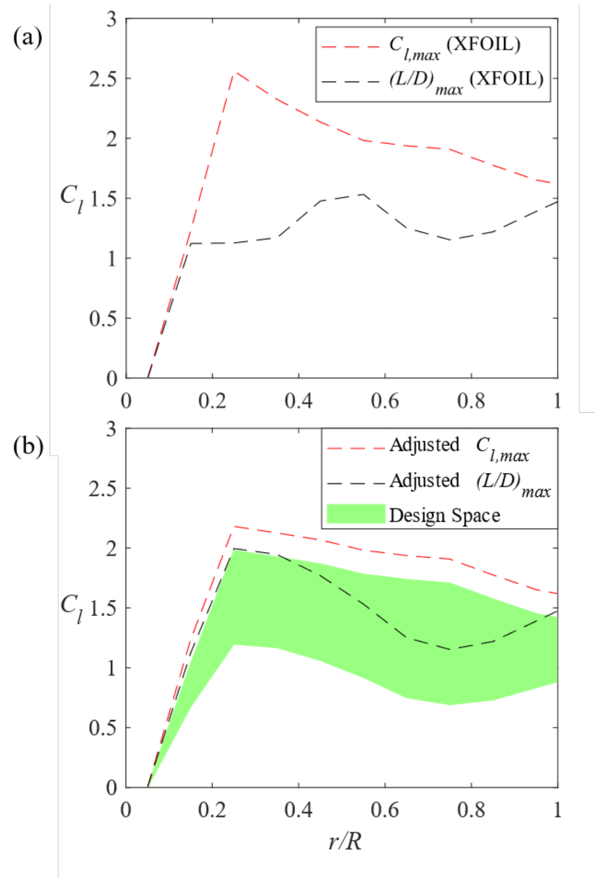

Figure 2-5. a) XFOIL maximum lift coefficient and lift-to-drag ratio curves of F1 airfoils for clean conditions; b) final design space and empirical lift coefficient limits with adjustments.

From the $C_{l,max}$ and $(L/D)_{max}$ curves, adjustments could then be made to create the final design space. The upper limit of the design space was created by uniformly decreasing the $C_{l,max}$ curve by 0.2 as shown in Eq. 2.3 to create a margin for excursions in angle of attack due to turbulence. The lower limit was created by adjusting the $(L/D)_{max}$ curve by a factor of 0.6 as shown in Eq. 2.4 , low enough to encompass the lift-to-drag (L/D) curve, thus creating a reasonable bracket for C_l distributions. The upper and lower C_l limits of the final design space can then be described as:

$$C_{l,upper} = C_{l,max} - 0.2 \qquad \text{Eq. 2.3}$$

$$C_{l,lower} = 0.6(L/D)_{max} \qquad \text{Eq. 2.4}$$

From this design space, three C_l distributions were determined for three different rotor designs presented in Figure 2-6. The three distributions were placed at the upper, middle, and lower parts within the design space. The Design 3 distribution is the same distribution used in the V2e rotor design and was kept the same as a method of comparison to the two other cases [49]. All the distributions decrease linearly from r/R = 0.25 to the blade tip. While the ideal aerodynamic performance would be achieved on the $(L/D)_{max}$ curve, the linear C_l distributions chosen allow for smoother chord distributions, and in case of Designs 1 and 2, the C_l distributions contain sections that overlap the $(L/D)_{max}$ curve. A similar strategy was used in the design of a 15 MW rotor with a similar rotor diameter that also achieved a chord distribution very close to optimum L/D [58]. These differences between the C_l distributions of Designs 1–3 lead directly to differences in blade chord and twist that could then be run in simulations to compare performance.

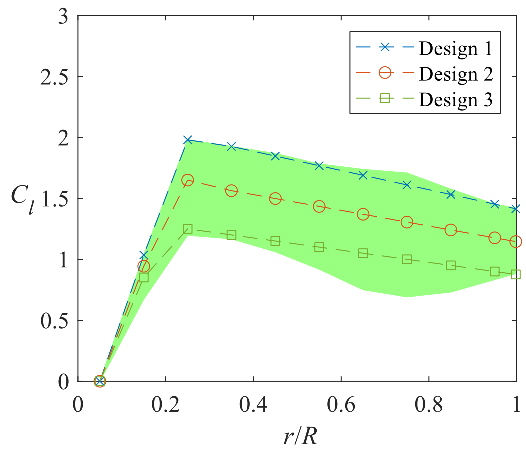

Figure 2-6. Lift coefficient distributions of Designs 1–3 within the final design space for clean conditions (free transition).

It should be noted that this design space has been created assuming clean blade surface conditions. This was done by using the e^N transition method with N = 9 in XFOIL when producing the F1 airfoil data [41]. However, turbine blades in actual operation will experience surface degradation overtime that can significantly increase roughness and cause premature boundary layer transition which is a cause for concern for aerodynamic performance. To maintain the usefulness of the design space shown in Figure 2-5b, XFOIL data was also obtained for an early transition case (N=0.3) and a fully turbulent case (forced transition at the leading edge) and then used to create two more design spaces using the same methodology and empirical adjustments described above. Polars of the F1 airfoil characteristics and transition location of three sets of XFOIL data are shown in Figure 2-7 and Figure 2-8 respectively.

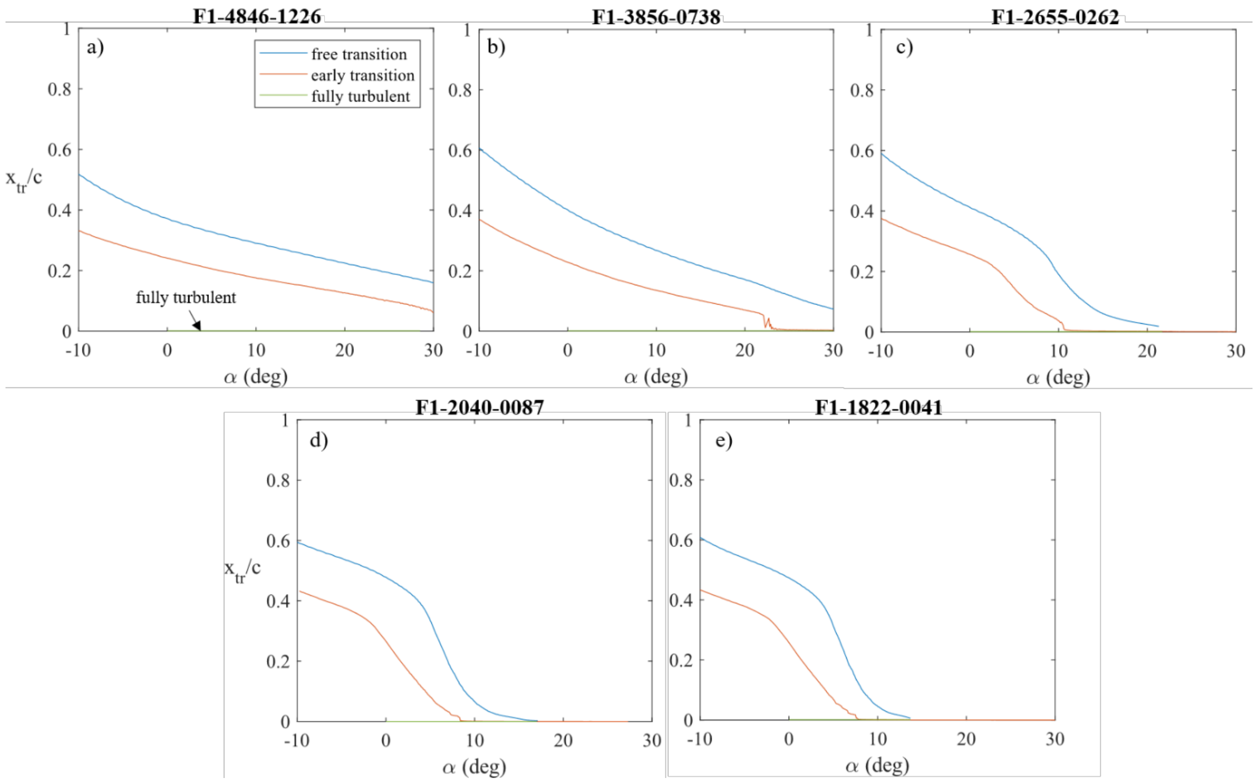

Figure 2-7. Airfoil transition location normalized by chord for F1 airfoils for varying angles of attack and three transition criteria. Note that x_{tr}/c = 0 for fully turbulent conditions on each airfoil.

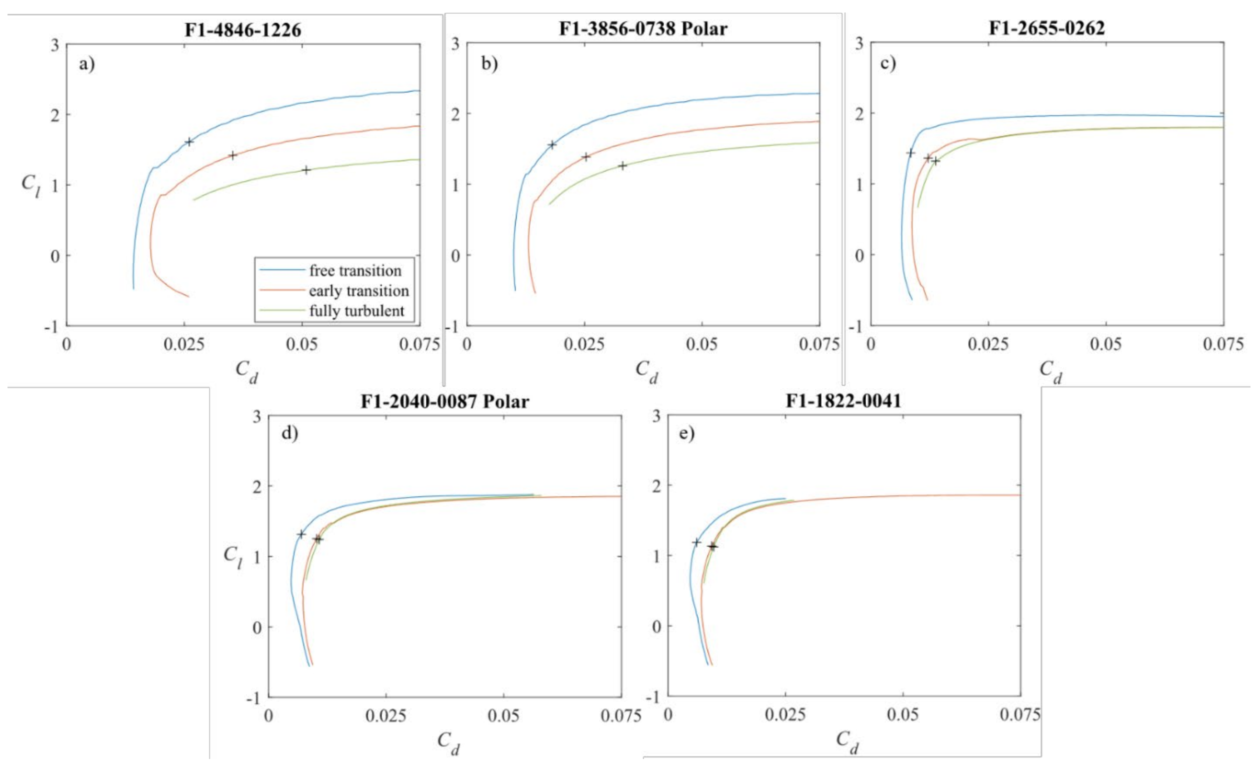

Figure 2-8. Polars of the F1 family airfoils for three different transition criteria produced using XFOIL, where '+' marks operating points at rated conditions of Design 2 for each transition criteria.

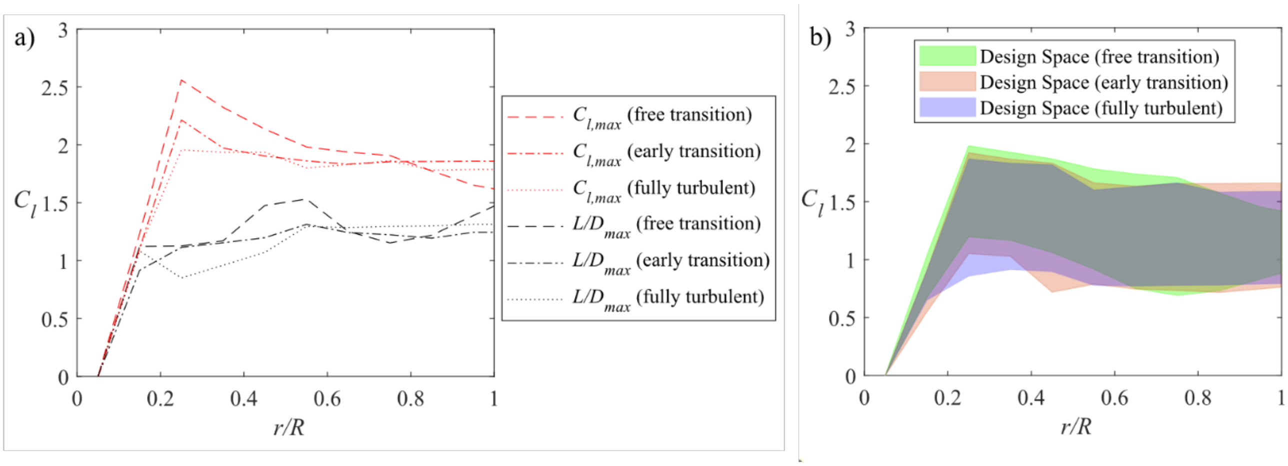

Figure 2-9. a) XFOIL maximum lift coefficient and lift-to-drag ratio curves of F1 airfoils for three different transition criteria; b) Empirical lift coefficient limits with adjustments and resulting design spaces for the three different transition criteria.

The two premature transition cases showed decreased C_l and increased C_d as expected with the thicker flatback airfoils showing the most loss in aerodynamic performance. The $C_{l,max}$ and $(L/D)_{max}$ curves using just the XFOIL data are shown in Figure 2-9a for all three transition cases. However, using the adjustments in Eq. 2.1 – Eq. 2.4 to create a C_l design space adjusts the thicker flatback airfoil characteristics where the most aerodynamic performance loss occurs. The resulting 3 design spaces shown in Figure 2-9b span similar ranges of C_l that do not differ as significantly as the $C_{l,max}$ and $(L/D)_{max}$ curves shown in Figure 2-9a, although the design spaces of the early transition and fully turbulent cases appear to be shifted slightly toward lower C_l values compared to that of the free transition case used in this study. Future designs may further consider these surface degradation effects in prescribing C_l distributions.

2.3 Results and Discussion

2.3.1 PROPID results

The parameters listed in Table 2-2 were inputs in PROPID for three separate cases, each with one of the three C_l distributions shown in Figure 2-6. The PROPID results are shown in Figure 2-10. The axial induction factor of 1/3 across the blade span in Figure 2-10a indicates that the prescribed axial induction factor was successfully converged upon in each of the three designs.

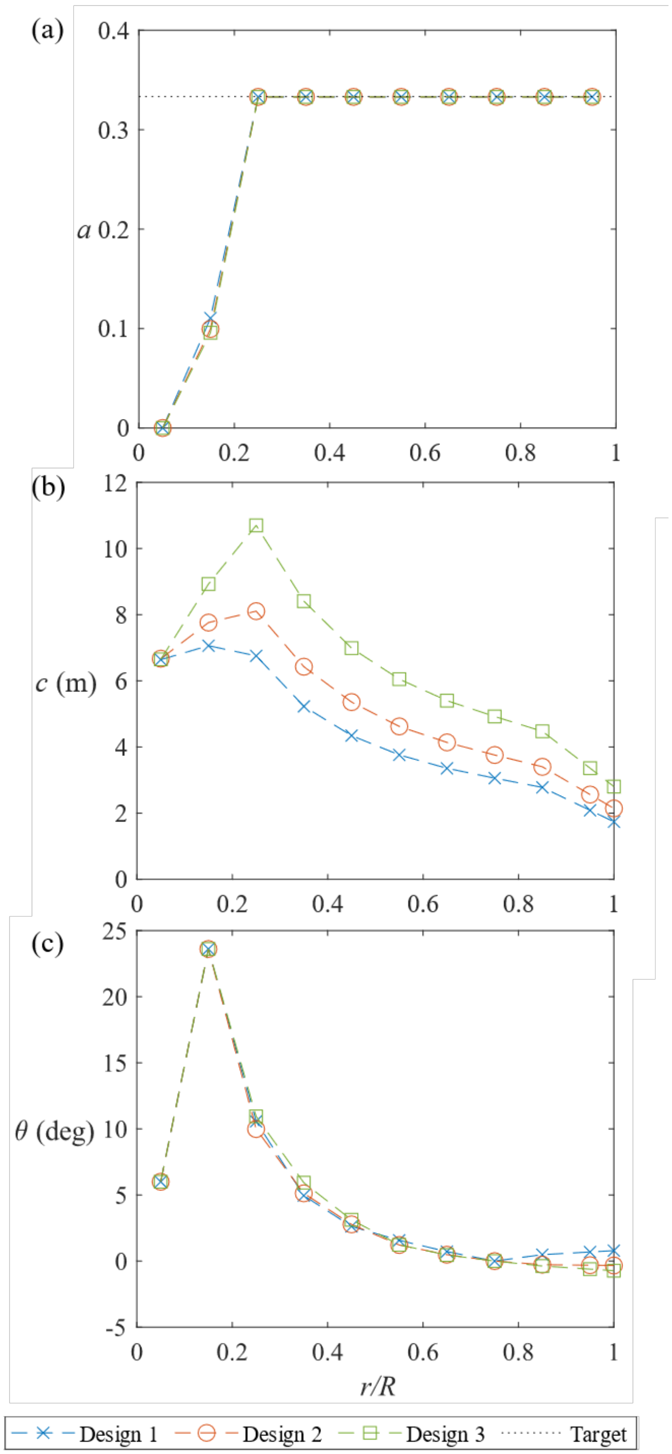

Figure 2-10. PROPID results for Designs 1–3 along nondimensional blade span: a) axial induction factor; b) chord; c) twist.

The chord distributions for Designs 1–3 in Figure 2-10b show Design 1 with the smallest chord distribution and Design 3 with the highest chord distribution, as expected given chord is inversely related to C_l. All three designs show maximum chord values between r/R = 0.15–0.25 with Design 3 having a maximum chord approximately 60% larger than that of Design 1.

The twist distributions shown in Figure 2-10c are similar between Designs 1–3 (note that greater positive twist angle twists the blade into feather). Between r/R = 0.15–1.0, Designs 2 and 3 smoothly decrease from ~24° to slightly negative angles past r/R = 0.75. However, in Design 1, twist starts to increase past r/R = 0.75. This twist increase occurs because the prescribed C_l values at those locations required less angle of attack than would occur if the twist distribution were to continue decreasing smoothly as is the case in Designs 2 and 3. Because the trends in twist at the blade tip appear in order from Design 1 to Design 3, and since the Design 1 C_l distribution is already at the upper limit of the design space, Design 1 was left unchanged. A 1:1 scale rendering of the three designs is shown in Figure 2-11 below as a more realistic view of the blade geometries.

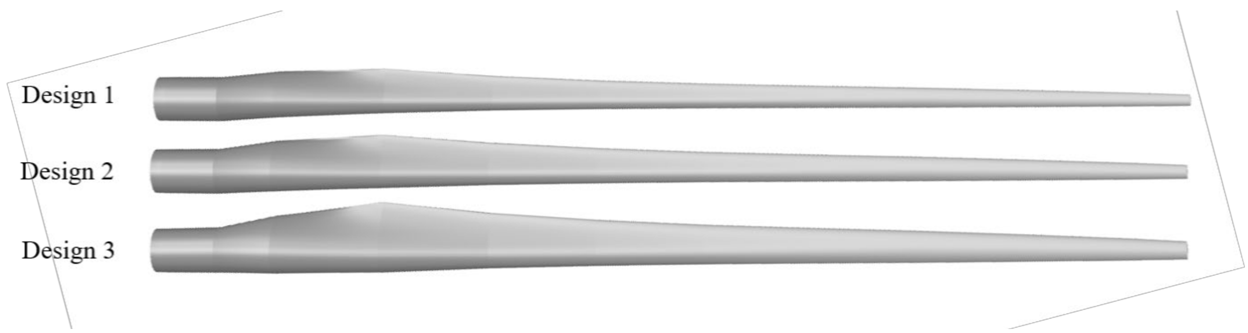

Figure 2-11. 3-D rendered blades for Designs 1–3.

Table 2-4. Blade pitch angle and rotor performance (PROPID).

	Pitch angle (β)	$C_{P,max}$ (PROPID)	C_T @ $C_{P,max}$ (PROPID)
Design 1	−3.91°	0.505	0.825
Design 2	−0.02°	0.511	0.823
Design 3	2.79°	0.510	0.823

The PROPID results for blade pitch angle (β), maximum $C_{P,max}$, and C_T are shown in Table 2-4. The blade pitch angle refers to the pitch in angle in Region 2 of the power curve to get the desired aerodynamic performance and is in reference to r/R = 0.75 where blade twist is zero. The $C_{P,max}$ and C_T values are calculated at the design λ of 9.25. These results indicate that Design 2 is predicted to have slightly better performances than Designs 1 and 3. However, the lack of blade flexibility in models used within the PROPID code should be considered in interpreting PROPID predicted $C_{P,max}$ values and warrants further rotor performance verification through the subsequent OpenFAST simulations.

2.3.2 OpenFAST simulations

The three designs were subsequently analyzed in OpenFAST to compare performance predictions and observe aeroelastic effects on power and thrust. The process of running OpenFAST, and its results will be discussed in the following subsections.

OpenFAST parameters

All simulations were performed using steady wind speeds in Region 2 (5 m/s to U_{rated}) neglecting shear and without a controller. Simulations were performed at each wind speed for a sufficiently long time in order to ignore initial transient effects in OpenFAST. Rotor speed was held constant at each wind speed such that the design λ of 9.25 was maintained, and β values from PROPID (shown in Table 2-4) were used. For aerodynamic loads, the Aerodyn 14 module was used [48]. The V2e tower design and blade structural properties from Escalera Mendoza *et al*. [49] were used for all three rotors. These blade structural properties include stiffness values along the blade span in the flapwise and edgewise directions that characterize the blade flexibility. Finally, both rigid and flexible blade cases were considered.

Flexible blade adjustment

As described previously, a design strategy was to maximize swept area by minimizing pre-cone and tilt angle while maintaining IEC 61400-1 standard set margins for tip-deflection as well as aligning the blades at $\Psi = 0°$ to be vertical. To achieve this in operation, blade deflections must be considered as they will change the blade alignment and thus swept area. Therefore, for OpenFAST simulations with flexible blades, the pre-cone and shaft tilt angles were changed to allow aeroelastic orientation of the blade at $\Psi = 0°$ to be nearly vertical when deflected downwind resulting in a blade pointing slightly upwind at $\Psi = 0°$ when rigid as can be seen in Figure 2-12. This adjustment was based on the average blade deflections observed in flexible blade simulations at $\Psi = 0°$ and at a high Region 2 wind speed (U = 8 m/s) with the V2e turbine. The rigid blade configuration is the same one shown above in Figure 2-2 above. The 8 m/s velocity was used based on the assumption that the turbine will be operating in this upper range of Region II for a majority of its time. Thus, adjusting for the deflections at 8 m/s would allow for the swept area to be near maximum as much as possible. However, the combination of pre-cone angle and shaft tilt angle was kept at 12° to prevent tower strike.

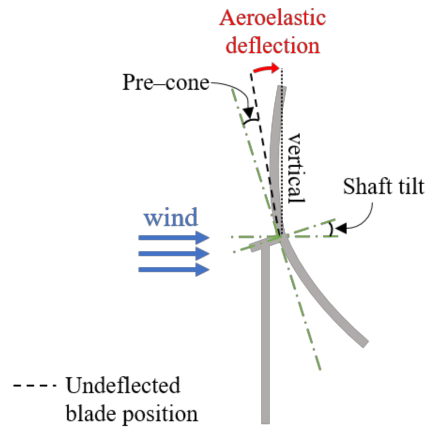

Figure 2-12. Pre-cone angle + shaft tilt configurations for flexible blade OpenFAST simulations.

Including tip deflections, when the performance of the flexible blade configuration is compared to that of the rigid blade configuration, initially less power will be produced at lower Region 2 wind speed as the rotor swept area will be smaller due to the upward pointing blade still being slightly upwind. But at higher Region 2 wind speeds, the flexible blade configuration will be able to produce more power as the near vertical blade will create a larger swept area than the rigid blade configuration that has a deflected upward pointing blade pointing downwind.

Table 5 shows these adjusted pre-cone and shaft tilt angles for the aeroelastic designs. There is only a 0.2% decrease in C_P and a 2.5% decrease in C_T due to aeroelastic deflections at a steady, no-shear 8 m/s wind. However, these differences may differ with turbulence and shear included.

Table 5. Rigid and flexible blade configurations.

	Rigid design	Aeroelastic design
Pre-cone angle	6°	3.6°
Operation cone angle	6°	7.8°
Shaft tilt angle	6°	8.4°
Pre-cone swept area [m^3]	91.81×10^3	91.33×10^3
Operation swept area [m^3]	91.81×10^3	89.80×10^3
C_P	0.498	0.496
C_T	0.836	0.815

OpenFAST results

For rigid blade simulations, the OpenFAST results for the induction factor and lift coefficient (prescribed parameters in PROPID) were verified to match the desired targets within 1%. All three designs produced similar power, but Design 2 provided the most power, producing 0.9% more than Design 1 and 0.7% more than Design 3 on average over the simulated wind speeds. Design 1 shows the highest rated thrust (T_{rated}) at 4.26 MN: 0.2% more than Design 3 and 0.7% more than Design 2. These results of aerodynamic power and thrust are consistent with the PROPID results which showed Design 2 with the highest $C_{P,max}$ of 0.511 and Design 1 with the highest C_T @ $C_{P,max}$ of 0.825. Average thrust across wind speeds decreased in the order of decreasing C_l distribution (i.e., Design 1 had the highest average thrust and Design 3 the lowest).

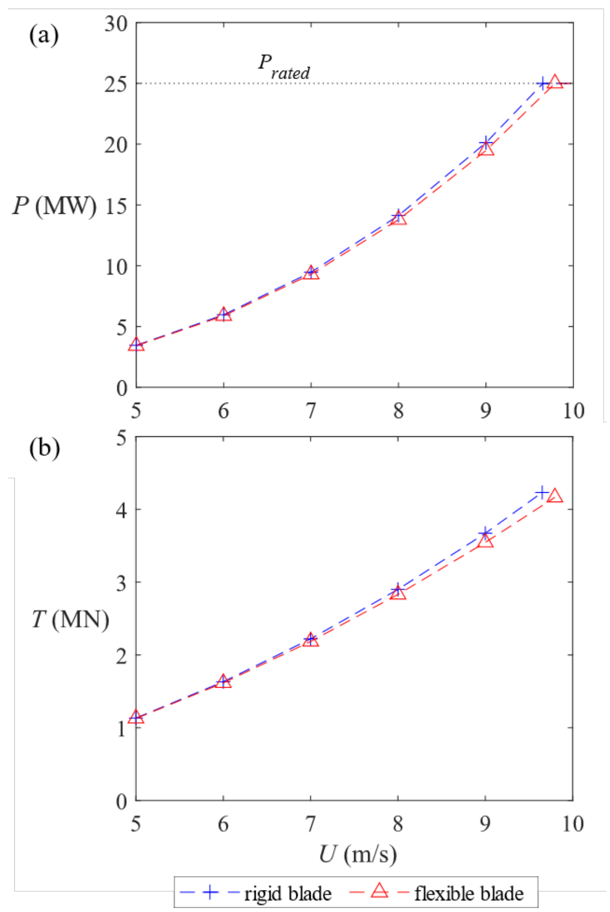

Figure 2-13. Aeroelastic effects on Design 2 with steady wind (OpenFAST): a) aerodynamic power; b) aerodynamic thrust.

The aeroelastic effects on power and thrust are shown in Figure 2-13. As the blades deflect downwind, the rotor swept area decreases, effectively reducing the power production and also thrust forces on the rotor. The results for Design 2 show a power loss between 1.4%–4.7% across wind speeds with the greatest loss at U_{rated} when compared to the rigid rotor. Likewise, T_{rated} decreases by 1.4% from 4.23 MN to 4.17 MN, but the reduction in thrust ranged from 0.4%–1.4% across wind speeds. Designs 1 and 3 also showed similar power and thrust performance.

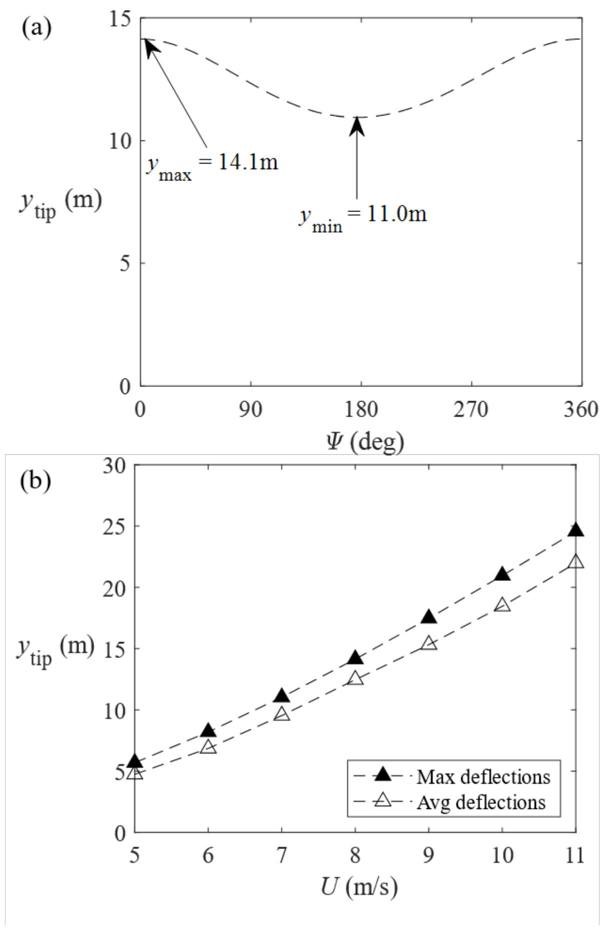

Figure 2-14. Downwind tip deflections on Design 2 blade (OpenFAST): a) at 8 m/s steady wind (vertical blade at Ψ=0º); b) 5 – 11 m/s steady winds.

Tip deflections for Design 2 in the flexible blade configuration are shown above in Figure 2-14. Figure 2-12a shows tip deflections at U = 8 m/s varying from 11–14.1 m downwind with maximum deflections occurring when the blade is at $\Psi = 0°$. As mentioned before, adjustments for pre-cone and shaft tilt angles for blade flexibility were based on average tip deflections observed at U = 8 m/s in the V2e turbine. However, the deflection observed in V2e was ~2 m larger than that observed in Designs 1–3. This meant that at U = 8 m/s the upward pointing blade for Designs 1–3 was slightly less vertical than desired and rather reached a more vertical position closer to U = 9 m/s. This difference may be corrected in a future iteration to further improve performance. Solely considering steady Region 2 wind, tip deflection limits specified by IEC standards were not violated, although more considerable deflections that would push these limits are often seen with extreme gust conditions such as DLC 1.4.

2.3.3 WISDEM results

In the final part of this study, the three rotor designs were evaluated using WISDEM (study carried out at NREL) to optimize for minimal rotor mass and LCOE. Since the WISDEM optimization was performed after the OpenFAST simulations, the resulting WISDEM structural properties are different from the more detailed V2e blade structural design by Escalera Mendoza *et al.* used in the OpenFAST simulations [49]. While creating higher fidelity structural designs for all three rotors would be ideal to use in the OpenFAST simulations, for purposes of this study, such structural designs were not performed due to time and resource constraints. However, the use of WISDEM allowed for more rapid estimates of structural design. By constraining the blade geometry, the WISDEM optimization can still provide a useful approximation of blade structural design to compare the effects of varying chord and twist distributions on blade mass and LCOE. Results can be seen below in Table 2-5. WISDEM was first run using a strain constraining approach, optimizing blade structures to a typical limit of 4,000 micro-strain due to flapwise and edgewise blade loads under extreme wind conditions [50, 59]. Spar cap thickness as well as the leading-edge and trailing-edge thicknesses were the drivers of the structural design. The structural optimization is performed using a 1-D model based on blade root bending moments using Glass Fiber Reinforced Materials. This approach was used for the blade structural design in Escalera Mendoza *et al.* [49]. The strain constrained approach resulted in Design 1 exhibiting the lightest blade mass and lowest LCOE most likely due to the smallest chord in Design 1. However, this approach also resulted in downwind tip deflections greater than 50 m for Designs 1 and 2 that surpassed downwind tip-deflection limits. Thus, the WISDEM approach was updated to constrain deflections in addition to strain. This deflection limit was based on the downwind deflection limits from the IEC standards for an upwind version of the V2e rotor [49, 51].

Table 2-5. WISDEM blade mass optimization results.

	Design	AEP (GWh/yr)	LCOE ($/MWh)	m_{blade} (kg)	y_{tip} (m)
Strain Constrained	1	135.2	71.88	1.281×10^5	59.95
	2	135.8	72.36	1.380×10^5	50.16
	3	135.5	73.53	1.586×10^5	40.18
Deflection Constrained	1	135.2	73.89	1.598×10^5	41.74
	2	135.8	72.72	1.450×10^5	41.63
	3	135.5	73.25	1.532×10^5	41.75

These results showed increased mass for Designs 1 and 2 but much more reasonable tip deflections. LCOE for the deflection constrained rotors also increased for Designs 1 and 2 as stiffer and heavier blades require more material. However, blade mass and LCOE for Design 3 decreased between the strain constrained rotor and the deflection constrained rotor, also resulting in higher tip deflections.

The tip-deflection constrained WISDEM results indicate Design 2 as the lightest and least expensive rotor. This rotor is the same design that showed the highest aerodynamic power in the OpenFAST simulations and the highest $C_{p,max}$ from PROPID. The results in AEP and mass (hence LCOE) indicate Design 2 as being the best of the three rotors. The high $C_{p,max}$ and moderate chord of Design 2 likely benefited the resulting LCOE by increasing AEP and limiting blade mass and thus costs to a moderate degree. Based on these results, of the three rotors designed in this study, Design 2 can be recommended for use in further studies of 25 MW offshore turbines including further structures analyses and controls design.

2.4 Conclusions

The benefits of continuously increasing offshore wind turbine scales call for extreme scale rotor designs that can maximally produce power. In this study, the aerodynamics of three different blade geometries were strategically designed using PROPID and compared through numerical simulations in OpenFAST and WISDEM for a 25 MW downwind rotor. This included a new optimization approach for the flexible blade configuration to consider optimum rotor tilt and coning based on aeroelastic deflections at sub-rated conditions as well as a rotor aerodynamic geometry that employs a design space based on a combination of maximum lift and maximum lift to drag ratio with the design objective to both maximize power production and minimizing rotor mass, so as to minimize the LCOE. Creating this design space required determining new empirical correlations based on experimental wind tunnel data to adjust inaccurate 2-D XFOIL data of the flatback airfoils used near the blade root. Three different rotor designs, each with different C_l distributions, were evaluated, first adjusting the designs to maximize swept area without violating tip-deflection constraints and thus maximizing power. OpenFAST was then used to predict desired performance and compare Designs 1–3. Finally, WISDEM was used to optimize for minimal rotor mass, and hence LCOE, while maintaining constraints on maximum tip-deflection and blade strain. The blade strain constrained cases and the maximum tip-deflection constrained cases showed different results in blade mass, a finding that could be important to consider in future studies. The three different design stages (PROPID, OpenFAST, WISDEM) performed in sequence provided a strategy for determining the best performing design, and all indicated that Design 2 was the preferred rotor due to the following results: highest $C_{p,max}$ from PROPID, highest power production in OpenFAST, lightest blade and lowest LCOE from WISDEM. Thus, the final 25 MW design was completed.

This study represents the first step in the aerodynamic design of highly flexible, downwind, extreme-scale 25 MW rotors, but can be applied to upwind extreme-scale rotors as well. As the focus of this study was on rotor aerodynamics, more work needs to be done on the structural and controls system aspects of these rotor designs. While this design process relied on predicting steady inflow wind performance, the careful consideration of design parameters in this study leads to the expectation that these rotors will still perform well under more realistic and extreme wind conditions. However, further simulations are recommended to assess this. A control system design study will be performed on the final rotor design developed in this paper which considers DLCs and incorporates an active IPC control system to better evaluate the performance of this rotor under more realistic wind conditions. Future studies on a more detailed structural design for this 3-bladed 25 MW rotor are also recommended. Future work may also focus on trade studies of pre-cone and shaft tilt angles to provide more benefit in power.

Chapter 3

Operational Pitch Actuation Dynamics for Offshore Wind Turbines ranging from 5 MW to 50 MW

Abstract

Modern wind turbines have been continuously growing in size due to the increased power generation and reduced costs associated with larger rotors and more abundant wind resources offshore. In order to effectively implement pitch control on blades that are longer, more flexible, and heavier than ever before, modern electric pitch systems must provide enough torque to overcome blade pitch inertia and loads while providing suitable control response frequencies. Despite this need, there is limited published research on the sizing of such pitch systems at extreme scales. This study models peak pitching power and pitch actuator torque requirements in Region 2 and Region 3 turbulent wind conditions. The developed model considers blade pitch response, pitching moments, pitch system dynamics, and blade aeroelasticity. The model is applied using an integrated wind turbine code used to simulate turbine response of a 25 MW offshore reference turbine with advanced pitch control under standardized turbulent wind conditions and shows that the fastest pitch response requirements occur in Region 3 wind speeds just above the rated wind speed and that the peak pitch actuator torque requirements are correlated with maximum pitching moments. The model is extended to turbines ranging from $5 - 50$ MW to develop a simplified scaling power law based on only the product of blade mass and mean chord length. This scaling law predicts maximum pitch actuator torque and maximum power consumed from pitch actuation based on results from computational simulations of multiple extreme- scale reference turbines. This study provides useful insights for the design and sizing of pitch systems in large-scale wind turbines.

3.1 Introduction

Wind energy has emerged as a leading form of renewable energy to keep pace with increasing demands for electricity and efforts to reduce fossil fuel consumption. Wind turbine technology has continuously been trending toward larger scales and offshore locations that allow for a reduced Levelized Cost of Energy (LCOE) due to larger rotor swept areas, faster wind speeds at higher hub heights, and more abundant wind resources offshore [5]. Currently, the largest commercially available platforms are around 15 MW for offshore sites but commercial plans up to 22 MW have already been revealed [60,61]. In the concept space, turbine designs with rated power as large as 25 MW and 50 MW have also been proposed [32, 37, 62–64].

Developing turbines at these extreme scales presents significant challenges. While increasing turbine size promises increased power production and decreased costs, it also produces structural challenges for blades that easily surpass 100 m in length and weigh tens of metric tonnes [33, 37]. Employing a downwind-facing rotor mitigates some of the challenges of extremely large blades by reducing blade mass and risk of tower strike, allowing for lighter, more flexible, and ultimately lower-cost blades as they are more likely to bend away from the tower under loads. However, downwind turbines face potential reductions in swept area due to blade deflections, which cause reductions in annual energy production. This issue can be addressed by optimizing rotor geometry to account for blade aeroelastic response [62]. Beyond the logistics of manufacturing and installation, once in operation, these blades will experience high structural loads and deflections that impact the turbine's efficiency and longevity due to scale and regardless of rotor orientation, especially in highly turbulent offshore wind conditions. Active pitch control alleviates these operational challenges, but requires advanced control algorithms and sufficient power to accurately and quickly pitch the blades. Therefore, both downwind and upwind variants face challenges with pitch control at extreme scales, e.g., at rated powers above 20 MW.

In order to optimally operate within offshore sites, wind turbines need sophisticated controllers to maximize power production in below-rated wind conditions, and limit loads and power production in above-rated wind conditions. Modern turbines use variable speed and variable pitch to accurately control power and torque generation [8]. Specifically, blade pitch can be varied based on parameters including the incoming wind speed and rotor speed in order to control blade angle of attack. Collective Pitch Control (CPC), which adjusts the pitch of all blades together is an effective strategy for smaller turbines, but variations in wind speed across the rotor disk increase and can lead to significant asymmetric loading on blades that are more pronounced at extreme scales [8, 66, 67]. In addition, blade tip deflections in extreme-scale downwind rotors are predicted to reach in excess of 20 m away from the tower, introducing further challenges in control as the blades experience these deflections out of phase from one another [32]. Therefore, modern offshore wind turbines implement Individual Pitch Control (IPC) where each blade receives additional cyclic pitch commands superposed over collective pitch commands to mitigate some of these undesirable effects [67]. Particularly for downwind rotors, IPC can also address the additional fatigue loading on the blades due to tower shadow effects [6, 68].

Collective pitch control commonly uses Proportional-Integral (PI) based or Proportional-Integral-Derivative (PID) based control to induce blade pitch motions to limit power and loads above rated conditions as documented in the literature [8, 67, 68]. Only a few experimental studies have reported physical pitch controllers on physical pitch systems where controller performance can be observed in conjunction with the pitch actuation system dynamics [69–71]. These experimental studies are focused on smaller turbines, i.e. only range up to the 2 MW scale since it becomes difficult to build a larger pitch system for lab testing purposes. With the scale of commercial turbines continuously growing, pitch systems larger than those at the 2 MW scale need to be designed. As such, much of the published work for large-scale wind turbines is simulation- based, e.g. coupled simulation codes like the OpenFAST code developed at the National Renewable Energy Laboratory (NREL) are often used to predict turbine pitch response dynamics for various control schemes [39]. However, these simulations generally do not investigate the physical peak power requirements of the mechanical pitch actuation system. The power requirements grow as the blades get larger, since the pitch system needs to overcome the pitch inertia of the blade to provide an angular acceleration, along with the aerodynamic forces and rotor inertial forces on the blades in operation.

Pitch actuation systems can be either hydraulic or electric [70]. Either type of pitch system may be installed in the next generation of offshore wind turbines, however, the advantages and disadvantages of each type must be considered to ensure the maximum performance and longevity of turbines. This is particularly important as turbines grow larger and are used in offshore sites that increase turbine maintenance complexity and cost. Multiple studies on wind turbine fault rates have found that pitch systems are associated with the highest rate of failure compared to all other wind turbine components [72, 73]. The differences in mechanical components between the two types of pitch systems (hydraulic and electric) lead to differences in the types of failures that each will experience. Typical hydraulic pitch systems use a pump and servo valve to operate a hydraulic cylinder attached to a slider crank mechanism at the blade root to rotate a blade about its pitch axis [74]. Because hydraulic pitch systems don't rely on geared components, they are relatively robust mechanically. However, they can have relatively slower response times, and lower energy efficiency [70, 75]. In terms of faults, failures in hydraulic pitch systems most frequently occur in the hydraulic components (hydraulic cylinder, valves, and accumulator unit) that may cause leakage of the hydraulic fluid and present risks to the environment [72].

While the robustness of hydraulic systems makes it difficult to assert that electric pitch systems are the future, electric systems have particular advantages to hydraulic systems that are valuable considerations for modern offshore wind turbines. Electric pitch systems actuate pitch through an electric pitch motor and gearbox system [76]. The torque from the pitch motor is amplified through the gearbox system which then connects to a geared pitch bearing to drive blade rotation. A simplified illustration of this is shown in Figure 3-1. These systems are compact and offer better accuracy and response time but can have mechanical robustness issues due to gear components eroding as well as other motor and drive-train related faults [70,77]. Common failure components of electrical pitch systems include motor relays, electrical current control components, and the battery pack [72]. In addition, electrical pitch systems are subject to seasonal faults where components like the batter pack appear to fail more in colder months [72].

Yet, when comparing failure rates of hydraulic and electric pitch systems per year, there is little difference. Hydraulic pitch systems perform marginally better than electric pitch systems at 0.54 failures per turbine per year as opposed to 0.56 [72]. There is also variation in failure rates between pitch systems from different manufacturers [72, 73]. Both indicate that the reliability of either type of system is currently similar. Lastly, pitch system faults appear to increase with turbine scale [72]. The growing scales of offshore wind turbines will need to be accompanied by more reliable pitch system designs to prevent losses in power generation and increases in costs and downtime.

Much of the published work on wind turbine pitch systems focuses on the modelling and faults of hydraulic pitch systems. Hydraulic pitch system models are included in PID-based controllers to tune performance when considering the dynamics and response time of the pitch system [71, 75, 78, 80]. A model for electric pitch actuation system dynamics that includes elastic deformation of the drive shaft and gear backlash is published [75]. An example of an electric pitch system used for field testing is found in the Controls Advanced Research Turbine (CART-2) at NREL and has been tested with PI-based IPC [69, 80–82]. It is important to consider the dynamics of pitch actuation system components in the context of physical pitching power requirements to predict real-world operation of extreme-scale turbines. However, there is a notable scarcity of studies that have made this connection, with published research primarily centered on smaller turbines (2 MW or less) equipped with hydraulic-drive pitch systems.

Few studies have considered the comprehensive sources of pitch loads on blades. For example, equations for calculating gravitational, aerodynamic, and centrifugal pitch loads have been published by Dai et al. [83]. These equations were then applied to a 1.2 MW turbine with an electric pitch system to quantify each component of pitch loads with azimuthal angle, pitch angle, and blade span. A similar approach has been used to design a controller for a rotary hydraulic pitch system which was found to improve pitch reference tracking and power output smoothness using experiments and simulations [71]. Analysis of pitch loads using SCADA data of a 2 MW turbine reveal a linear relationship between rotor speed and pitch load below-rated wind speeds and a sinusoidal relationship between pitch loads and azimuthal angle [84]. No published research has translated pitch loads into useful results on pitch system sizing requirements for turbines even at these smaller scales, let alone for large offshore turbines that are more than 10 MW in size for which electric-drive pitch systems are more prevalent. For such turbines, the pitch system and hub can represent about $7-8\%$ of the capital expenditures of the turbine [38]. Friction from the pitch bearing also creates significant resistance to pitch actuation [85]. For extreme-scale turbines, pitch bearing friction may contribute the largest percentage of the total moment the pitch motor must overcome with conservative estimates reaching up to 80% [85]. However, estimation of the pitch bearing moment is complex, depending on many parameters related to the mechanical components of the bearing, and there is much uncertainty in predictions. Analysis of various pitch bearing models has not shown consistently accurate estimations when compared to experimental data [86]. Methods of pitching moment estimations due to aerodynamic, gravitational, and inertial effects on blades are currently more reliable, but in considering the total pitching moment on blades, pitch bearing friction cannot be overlooked.

Understanding pitch system requirements for extreme-scale turbines improves optimization of aerodynamic and structural rotor design, predictions of realistic performance for improved controller design, and fidelity of LCOE estimations. To the authors' knowledge, this paper is the first to present a method of estimating peak blade pitching power and pitch actuator torque requirements for extreme-scale turbines due to aero-inertial effects based on results from coupled simulations using advanced blade pitch control. Blade root pitching load estimates are obtained using the OpenFAST code where the ElastoDyn module calculates these loads as a combination of aerodynamic, gravity, and mass/inertia loads under various wind conditions [39]. Standardized Region 2 and Region 3 wind conditions are considered based on conditions specified by the International Electrotechnical Commission (IEC) 61400-1 standards for wind turbine design [51]. A method for estimating blade pitching inertia is developed that includes structural deflection and pitch drive inertial effects. This study is also the first to consider the peak pitching power requirements based on electric-drive pitch systems at these scales. The novel pitch drive inertia model uses field-tested pitch actuator data obtained from the electric pitch system of the CART-2 turbine in order to account for the pitch system dynamics [80]. This methodology was applied as an exploration of peak pitch response and moments of academic reference turbines and their implications on power consumption requirements for extreme-scaling turbines operating in turbulent offshore wind conditions. A case study of an offshore downwind turbine with a high-fidelity IPC controller is presented for evaluating peak pitch requirements at the 25 MW scale. Results from additional reference turbines ranging from 5 MW to 50 MW in rated power are used to develop a novel scaling law for estimating maximum pitching moment, actuator torque, and pitching power as a function of blade chord length and mass. The results provide valuable insights into design driving wind conditions and pitch system sizing required for extreme-scale wind turbines.

3.2 Methodology

3.2.1 Pitching Power and Pitch Actuator Torque Calculation

In this study, a model for blade pitch is employed to estimate pitching requirements for extreme-scale turbines with electric-drive geared pitch systems. The model considers the pitch system, shown in Figure 3-1, in the context of an individual blade, where an electric pitch motor and gearbox assembly drive blade pitching at the root. The pitch motor and gearbox assembly transmit torque to the blade through toothed contact with a geared pitch bearing. The pitch motors are located within the turbine's hub and receive commands from the controller (not shown in Figure 3-1). All pitch-related variables act about the pitch axis

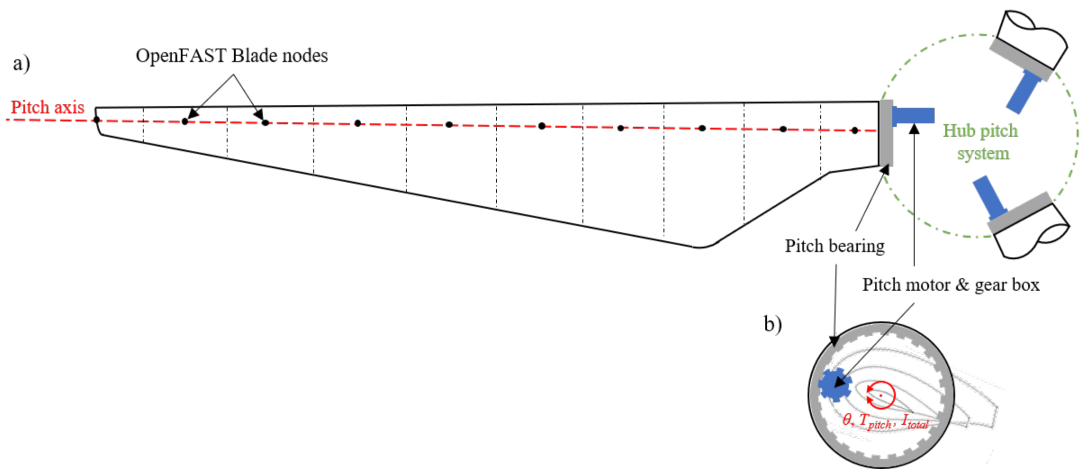

Figure 3-1. Blade and hub components considered for the pitch model.

The steady-state power required for pitching a blade (P_{pitch}) depends on pitch rate ($\dot{\theta}$) and the blade root moment about the pitch axis (T_{pitch}) as shown in Eq. 3.1 where the individual blade moment arises due to gravitational, inertial, aerodynamic, and frictional loads on the blade [83, 85]. Pitch bearing friction is not explicitly included in the application of this model within this study due to uncertainty in predictions but should be considered when interpreting the results.

$$P_{\text{pitch}} = T_{\text{pitch}}\dot{\theta} \qquad \text{Eq. 3.1}$$

While Eq. 3.1 estimates the amount of power for constant $\dot{\theta}$, blades often need to accelerate to achieve pitch control. In this case, the pitch actuator torque applied by the pitch motor and gearbox (T_{act}) must be greater than the pitching moment on the blade (T_{pitch}). The difference between these moments is the product of the total pitch inertia (I_{total}) and the pitch acceleration ($\ddot{\theta}$) as described by Eq. 3.2, which is reorganized in Eq. 3.3 to express the peak pitch actuator torque ($T_{act,max}$) based on the maximum blade pitching moment requirement $T_{pitch,max}$.

$$T_{\text{net}} = T_{\text{act}} - T_{\text{pitch}} = I_{\text{total}}\ddot{\theta} \quad \text{Eq. 3.2}$$

$$T_{\text{act,max}} = I_{\text{total}}\ddot{\theta} + T_{\text{pitch,max}} \quad \text{Eq. 3.3}$$

The total pitch inertia is comprised of three components as shown in Eq. 3.4: the rigid blade mass moment of inertia (I_{pitch}), the added blade mass moment of inertia due to blade deflections (I_{defl}), and the actuator drive inertia reflected from the blade and gearbox assembly (I_{drive}).

$$I_{\text{total}} = I_{\text{pitch}} + I_{\text{defl}} + I_{\text{drive}} \quad \text{Eq. 3.4}$$

Estimation of I_{total} components at extreme-scales requires simulation results. The blade mass moment of inertia (I_{pitch}) is derived from the blade's structural design. Blade deflection data from simulations provides estimates for I_{defl}, calculated using the parallel axis theorem. Actuator drive inertia (I_{drive}) is scaled using data from the electric pitch-system on the CART-2 demonstrator turbine. Because I_{drive} represents the inertia perceived at the pitch motor shaft, the results of this study are estimations for electric pitch systems as typical hydraulic systems do not have the gearbox used to amplify pitch motor torque. Considering the differences in mechanical components between hydraulic and electric pitch systems may vary, I_{drive} values and thus estimates of required pitch actuator torque may differ and should be considered when interpreting the results of this study.

This model allows for precise calculation of the power and torque required to control the pitch of large wind turbine blades under turbulent operational wind conditions. By integrating structural and dynamic considerations, it can estimate realistic pitch control requirements for the simulated turbine.

3.2.2 Computational Tools

The OpenFAST framework [39], created by NREL, is used to run the present simulations of the 25 MW turbine based on a detailed rotor design [62] and a detailed tower and monopile design [49, 87]. OpenFAST is a coupled aero-servo-elastic simulation tool which has been extensively employed and validated for the dynamics of wind turbine systems [88]. OpenFAST integrates multiple coupled computational modules to simulate aerodynamics, hydrodynamics, structural dynamics and controls systems for both onshore and offshore turbines and is used to predict turbine dynamics, allowing for simulation of time-varying effects and various degrees of freedom including blade pitch angle and pitching moments. The aerodynamics module used in OpenFAST for the present simulations is Aerodyn15 which uses blade-element momentum theory for predicting aerodynamics [89]. Note that the blade torsional degree of freedom is not considered for this study since the ElastoDyn module was used for structural dynamics within OpenFAST. OpenFAST can also simulate turbines under unsteady wind conditions, making it useful for simulating Design Load Cases (DLCs) as defined by the International Electrotechnical Commission (IEC) 61400-1 standards for wind turbine design [51]. In particular, the TurbSim tool, also developed by NREL, is used herein to generate time-series inflow wind files for DLC 1.2 and DLC 1.3 needed for OpenFAST simulations [90]. TurbSim stochastically generates 2-D stationary turbulent wind field data in three directions within a specified rectangular gridded domain that fully encapsulates the rotor swept area. The IEC Kaimal turbulence spectra model is used to generate all DLC 1.2 and DLC 1.3 data for this study [51].

The coupling of structural and aerodynamic analyses within OpenFAST ensures accurate time-varying predictions of wind turbine dynamics. This makes the OpenFAST tool well-suited to estimate the quantities described in the equations shown in Section 3.2.1. OpenFAST can provide time-varying predictions for the pitching moment at the blade root (T_{pitch}) and pitch angle (θ) response under specified wind conditions. Finite differencing is then used on the pitch angle signal from OpenFAST to estimate pitch rate and acceleration. Thus, pitching power can be estimated based on Eq. 3.1. One may consider approaching the problem in reverse, where pitch motor rated torque is an input in calculating pitch rate limits and power consumption rather than an output from OpenFAST simulations. Such an approach would efficiently provide pitch system power consumption based on commercial pitch system requirements. However, information on OEM pitch motor specifications at these scales was not readily available. Thus, this method of estimating pitching power and actuator torque was developed to use predictions of pitch rate and pitching moments from the OpenFAST simulations of reference turbines in wind conditions where high pitch activity is expected. OpenFAST results are also needed in estimating the blade flexibility components of pitch inertia (I_{defl}) by taking time-averaged maximum blade deflections predicted by OpenFAST. Further discussion of estimating the total pitch inertia is presented in Section 3.2.6.

3.2.3 Simulated Wind Turbine Model

The wind turbine model used in the OpenFAST simulations is a 25 MW three-bladed downwind offshore turbine with 165 m long blades labeled 25-DW2 and is the same model used in Phadnis et al. and Pusch et al. [49, 91, 92]. The blade chord and twist distributions for the 25-DW2 blades are the same as those for the design labeled V2e in Escalera et al. but using the pre-cone and shaft tilt angles shown in Table 3-1 [49]. This turbine features a fixed monopile and is designed for IEC standard class I-B wind speeds [51]. Key design parameters are summarized in Table 3-1. The rotor is aeroelastically designed for maximum power production by inversely designing the blades to meet desired aerodynamic parameters as well as optimizing for maximum swept area in operation within Region 2. Structural design of the blades, tower, and monopile was completed using an aero-structural rapid screening (ASRS) method published by Escalera-Mendoza et al. [87]. The ASRS approach optimizes structural properties by emulating controller performance and evaluating rotor aerodynamics and structural loads.

Table 3-1. Turbine Model Parameters.

Parameter	Value
Rated power	25 MW
Number of blades	3
Optimum tip-speed ratio	9.25
Rated wind speed	10 m/s
Blade length	165 m
Pre-cone angle	3.6°
Shaft tilt angle	8.4°
Hub radius	6.75 m
Hub height	199.8 m
Tower length	178.3 m
Monopile length	90 m
Water depth	30 m
Tower material	Steel
Monopile material	Steel
Blade material	Tri-axial fiberglass (root)
	Uni-axial carbon fiber pre-preg (spar cap)

Within OpenFAST, blade flexibility degrees of freedom are considered and the initial pitch angle is set to the design pitch angle for Region 2 wind speeds. The yaw degree of freedom is not considered so as to focus on the pitch angle (θ) response and since there is no yaw error given the inflow wind conditions selected. Since the rotor faces downwind, tower shadow effects are included. CPC and IPC are implemented via Simulink and is further described in Section 3.2.5. The resulting θ response, T_{pitch}, and blade deflections are analyzed to estimate P_{pitch} and T_{act}. Finite differencing on the θ response is used to calculate the $\dot{\theta}_{\max}$ and $\ddot{\theta}_{\max}$ values needed for $P_{\mathrm{pitch,max}}$ and $T_{\mathrm{act,max}}$ estimations.

3.2.4 Design Load Cases

Pitch actuation systems need to have sufficient power to handle high shear and large fluctuations in inflow speed that extreme-scale offshore wind turbines will experience. Although shut-down wind conditions may induce extreme pitch responses, this study focuses on wind conditions in which the turbine is able to generate power (Region 2 and 3). Wind conditions chosen are in attempt to generate peak pitch responses needed to calculate pitching power consumed and pitch actuator torque as shown in Eq. 3.1 and Eq. 3.3 respectively. Design Load Cases 1.2 and 1.3 are used as the inflow wind fields in OpenFAST simulations [51]. These are used to model normal turbulence (DLC 1.2) and extreme turbulence (DLC 1.3) wind conditions that wind turbines likely experience over the course of their normal lifetimes. This is crucial for extreme-scale offshore turbines as longer blades and taller hub heights result in operating conditions consisting of higher wind speeds and turbulence in offshore sites. Inflow wind files are generated using TurbSim for a 21 × 21 grid with a shear exponent of 0.2 across the rotor disk and surface roughness length of 0.03. Mean wind speeds at the hub height ($\overline{U}_{\text{hub}}$) chosen for OpenFAST simulations are limited to Region 2 and Region 3 and range from 4 – 24 m/s in increments of 2 m/s for a given DLC. Data from six random seeds are generated at each mean wind speed, resulting in a total of 66 cases for each DLC to provide unsteady velocity in all three directions where the *x* direction is downstream normal to the rotor plane, the *y* direction is horizontal parallel to the rotor plane, and the *z* direction is vertical. Within OpenFAST, each DLC case is run for a total of 400 s per simulation with a time step of 0.0125 s. An example of the generated TurbSim data is shown in Figure 3-2. As shown, the DLC 1.3 data indicates increased velocity fluctuations in all 3 directions compared to that of DLC 1.2 due to the higher turbulence standard deviation value [51].

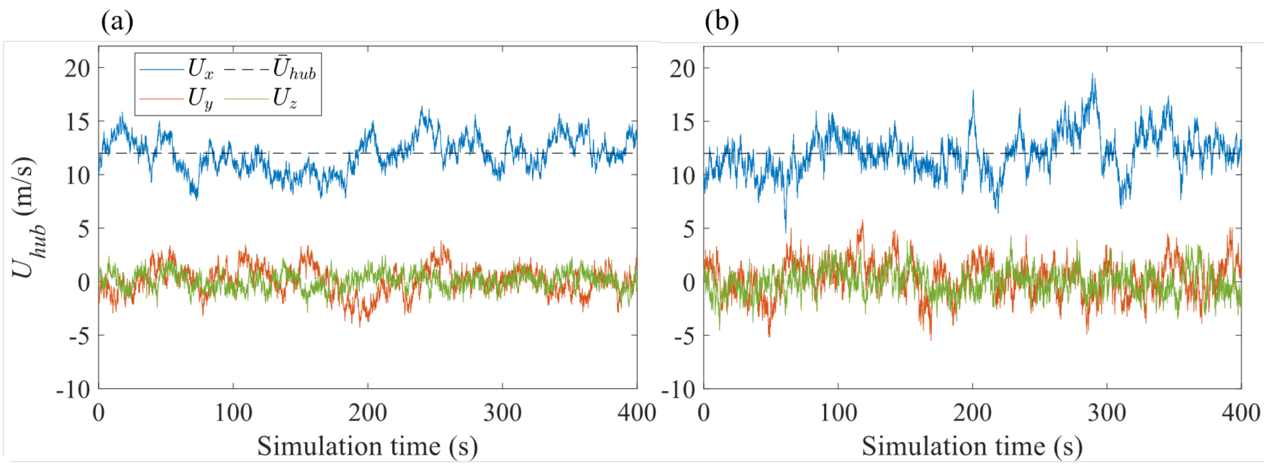

Figure 3-2. Example TurbSim wind data at hub height for a) DLC 1.2; b) DLC 1.3. Both data are generated at a mean wind speed of 12 m/s. Wind directions are in the inertial coordinate system used in OpenFAST (i.e. U_x is in the nominal downwind direction).

3.2.5 Control System

The controller design was carried out by collaborators at the University of Colorado Boulder [91, 94]. The baseline controller for the 25-DW2 turbine in above-rated operation is implemented as a gain-scheduled proportional-integral (PI) collective pitch control (CPC) [93]. The PI gains are auto-tuned using a zeroth- order optimization framework and are scheduled using the turbine's power-to-pitch sensitivity as a function of the collective pitch angles as shown in Figure 3-3 [93, 94]. For below-rated operation, a $K\omega^2$ control law is implemented to maximize power capture [95].

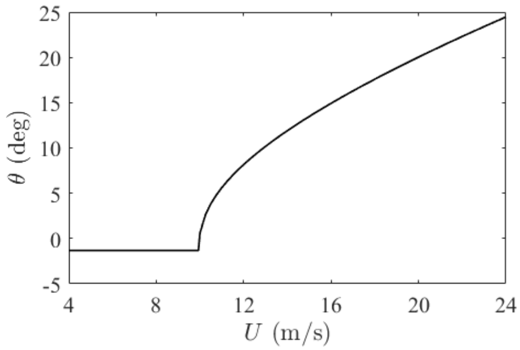

Figure 3-3. Pitch schedule used in the baseline collective pitch controller.

Augmenting the baseline controller with IPC is commonly done to reduce fatigue damage on the turbine components [67]. In this research, IPC is used to mitigate blade fatigue caused by periodic and asymmetric loading across the rotor plane due to wind shear. As shown in Figure 3-4, this is achieved by reducing the once-per-revolution (1P) blade loads using a multi-blade coordinate (MBC) transform on blade root bending moments ($M_{y\{1,2,3\}}$) as described in Eq. 3.5 [67, 96].

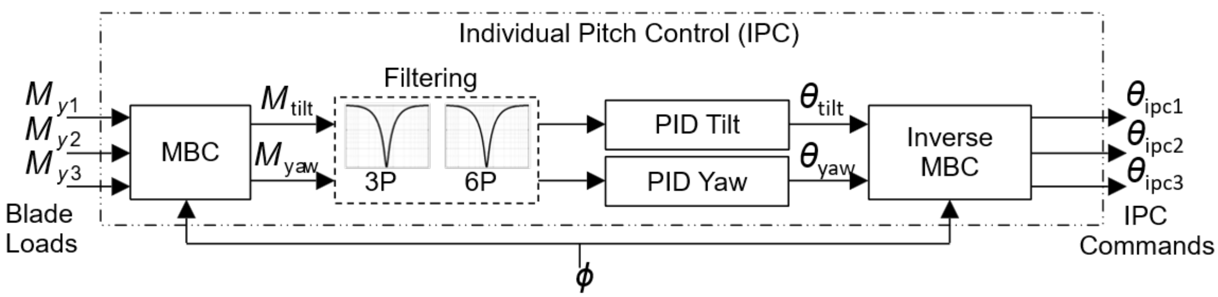

Figure 3-4. Individual pitch control block diagram.

$$\begin{bmatrix} M_{\text{tilt}} \\ M_{\text{yaw}} \end{bmatrix} = \begin{bmatrix} \cos(\phi) & \cos\left(\phi + \dfrac{2\pi}{3}\right) & \cos\left(\phi + \dfrac{4\pi}{3}\right) \\ \sin(\phi) & \sin\left(\phi + \dfrac{2\pi}{3}\right) & \sin\left(\phi + \dfrac{4\pi}{3}\right) \end{bmatrix} [M_{y1} \quad M_{y2} \quad M_{y3}]^T \qquad \text{Eq. 3.5}$$

In Eq. 3.5, ϕ is the azimuth angle of the first blade. The MBC transform converts the rotating 1P loads to constant loads along the vertical (yaw) and horizontal (tilt) directions in the rotor plane. After filtering out higher frequency harmonics of the 1P frequency, two single-input, single-output (SISO) proportional-integral-derivative (PID) controllers are used to generate the pitch commands in the yaw (θ_{yaw}) and tilt (θ_{tilt})

directions. The inverse MBC transform is then used to convert the pitch commands into the rotating frame to give the individual pitch commands ($\theta_{\text{ipc}\{1,2,3\}}$) per blade as shown in Eq. 3.6.

$$\begin{bmatrix} \theta_{\text{ipc1}} \\ \theta_{\text{ipc2}} \\ \theta_{\text{ipc3}} \end{bmatrix} = \begin{bmatrix} \cos(\phi) & \sin(\phi) \\ \cos\left(\phi + \frac{2\pi}{3}\right) & \sin\left(\phi + \frac{2\pi}{3}\right) \\ \cos\left(\phi + \frac{4\pi}{3}\right) & \sin\left(\phi + \frac{4\pi}{3}\right) \end{bmatrix} \begin{bmatrix} \theta_{\text{tilt}} \\ \theta_{\text{yaw}} \end{bmatrix} \qquad \text{Eq. 3.6}$$

The individual pitch commands are superimposed upon the collective pitch commands and applied to each blade pitch actuator as shown in Eq. 3.7.

$$\theta_{\{1,2,3\}} = \theta_{\text{cpc}} + \theta_{\text{ipc}\{1,2,3\}} \qquad \text{Eq. 3.7}$$

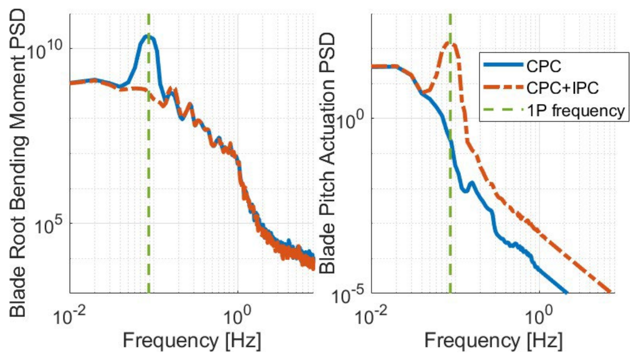

Figure 3-5. Power spectral density (PSD) for blade root bending moment and blade pitch actuation for turbulent wind simulation at 16 m/s for the 25-DW2 turbine.

Figure 3-5 shows the power spectral density of the blade root bending moment and blade pitch actuation signal for the first blade. For the baseline controller (blue curves), a peak in load is observed at the 1P frequency (green dashed line). This peak in blade load at the 1P frequency is eliminated using IPC (red curves). The cost of IPC is the increased pitch actuation at the 1P frequency, which can result in faster wear of the pitch drive motors due to the higher pitch travel. Since one of the objectives of this study is to analyze the pitch actuator requirements at a 25MW scale such that reliable performance is achieved, no maximum pitch rate constraint was set in the controller. The simulations were then used to analyze and determine requirements for the pitch actuator.

Controller tuning was finalized prior to running the OpenFAST simulations used in this study. The results from this study may be used to further tune the controllers of the simulated turbines, but are not explicitly done so for this study as the focus is not controller design.

3.2.6 *Estimating Blade Pitch Inertia*

To estimate pitch actuator torque (T_{act}), the total blade inertia about its pitching axis (I_{total}) must be calculated for the 25-DW2 blades. This is accomplished by decomposing I_{total} into three components as shown in Eq. 3.4: a rigid blade component (I_{pitch}), an added blade flexibility component (I_{defl}), and a pitch actuator drive inertia component (I_{drive}). Two of these components, I_{drive} and I_{defl}, are estimated using OpenFAST while I_{drive} is scaled using data from the CART-2 demonstrator [80].

The blade mass moment of inertia (I_{pitch}) is derived from the blade structural design of the 25-DW2 turbine. This includes flapwise and edgewise blade inertia per unit length at specified blade segments along the blade span. Therefore, I_{pitch} is simply the sum of the total flapwise ($I_{\text{flp,pitch}}$) and edgewise inertias ($I_{\text{edg,pitch}}$) about the pitch axis as shown in Eq. 3.8. However, the flapwise and edgewise pitch inertias are defined per unit length, and thus are calculated per span-wise blade segment *n* as specified within the OpenFAST model using the length of each blade segment (l_{spn}). Example blade segment locations are shown in Figure 3-1 where the blade structural properties (per unit length) are defined at the blade nodes located at the center of each blade segment. The per unit length inertias are also given with respect to the blade segment center of gravity and are adjusted to consider its value about the pitch axis. The offset between the blade segment center of gravity and pitch axis in the edgewise ($l_{\text{edg offset}}$) and flapwise ($l_{\text{flp offset}}$) directions is used to adjust the center of gravity based inertias ($I_{\text{flp cg}}$ and $I_{\text{edg cg}}$) using the parallel axis theorem to get $I_{\text{flp,pitch}}$ and $I_{\text{edg,pitch}}$ as shown in Eq. 3.9 and Eq. 3.10.

$$I_{\text{pitch}} = I_{\text{flp,pitch}} + I_{\text{edg,pitch}} \qquad \text{Eq. 3.8}$$

$$I_{\text{flp,pitch}} = \sum_{k=1}^{n} (I_{\text{flp cg},k} l_{\text{spn},k} + m_{\text{bld},k} l^2_{\text{flp offset},k} \qquad \text{Eq. 3.9}$$

$$I_{\text{edg,pitch}} = \sum_{k=1}^{n} (I_{\text{edg cg},k} l_{\text{spn},k} + m_{\text{bld},k} l^2_{\text{edg offset},k} \qquad \text{Eq. 3.10}$$

Blade deflection data (y) from OpenFAST simulations estimate I_{defl} using the parallel axis theorem as shown in Eq. 3.11. Maximum deflections at each blade node are calculated as the combination of flapwise and edgewise deflections. Ten blade nodes are used along the blade span from root to tip and are defined as depicted in Figure 3-1.

$$I_{\text{defl}} = \sum_{k=1}^{n} m_{\text{bld},k} y_k^2 \qquad \text{Eq. 3.11}$$

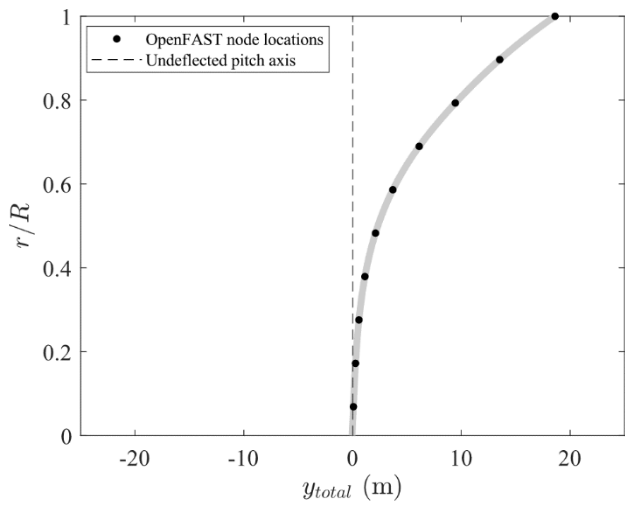

Figure 3-6. Example of maximum blade deflections across blade span in reference to rigid blade pitch axis. Case presented shows data from OpenFAST simulation with highest pitch rate ($\overline{U}_{hub}$ = 14 m/s, DLC 1.3)

The reflected pitch motor inertia from blade and gearbox, denoted as I_{drive}, is estimated using pitch actuator data from the 0.6 MW CART-2 demonstrator upscaled to 25 MW [80]. This scaling depends on four assumptions: 1) drive inertia scales with mass and the square of a length scale; 2) the length scale used is proportional to the blade root diameter; 3) actuator mass scales with rated power; 4) gearbox ratio is fixed as turbine scale increases. Using these assumptions, I_{drive} is estimated as shown in Eq. 3.12.

$$I_{\text{drive}} = \frac{P_{\text{rated}}}{P_{\text{rated,CART2}}} \left(\frac{d_{\text{root}}}{d_{\text{root,CART2}}} \right)^2 I_{\text{drive,CART2}} \qquad \text{Eq. 3.12}$$

The OpenFAST simulations provide the necessary data to calculate these inertia components under various wind conditions. By accurately estimating I_{total}, it can determine the maximum pitch actuator torque ($T_{\text{act,max}}$) required for effective pitch control in a 25 MW turbine. This method ensures that all relevant factors are considered, providing a comprehensive understanding of the pitch inertia and torque requirements. Consideration of all of these parameters is essential for designing robust and efficient pitch control systems for extreme-scale wind turbines.

3.3 OpenFAST Simulation Results

3.3.1 OpenFAST results

The OpenFAST simulations for DLC 1.2 and DLC 1.3 wind conditions are analyzed to provide estimates for pitching power (P_{pitch}) and pitch actuator torque (T_{act}) due to aero-inertial effects. An example of blade root pitching moment (T_{pitch}) and pitch angle (θ) along with pitch rate ($\dot{\theta}$) and pitch acceleration ($\ddot{\theta}$) are shown in Figure 3-7 and Figure 3-8, respectively. Negative values of T_{pitch} indicate pitching moments pushing the blade towards feather. Note that T_{pitch} does not include pitch bearing friction. Only a portion of the full 400 s simulation time is shown to illustrate the θ response when pitch control becomes active.

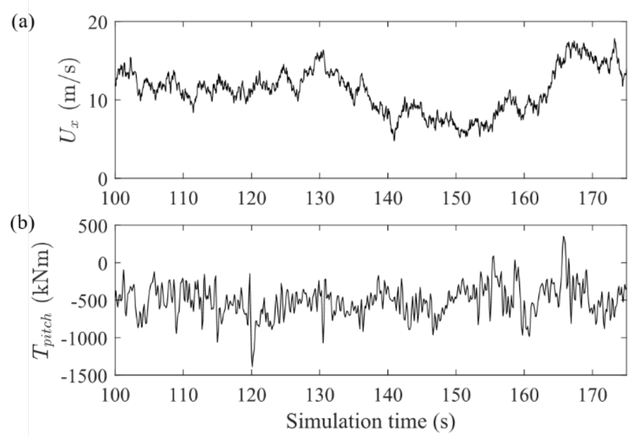

Figure 3-7. Example OpenFAST results for blade root pitching moment at a mean hub height wind speed of 14 m/s under DLC 1.3 wind conditions: a) wind speed in nominal downwind direction and b) blade root pitching moment.

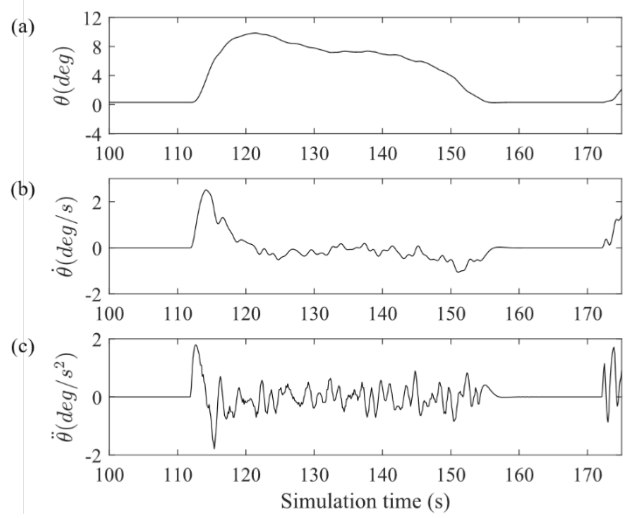

Figure 3-8. OpenFAST results for blade pitch from the same case as Figure 3-7 showing: a) blade pitch response directly from OpenFAST, b) pitch rate, and c) pitch acceleration.

At each DLC and mean wind speed at the hub height ($\overline{U}_{\text{hub}}$), the data is investigated to obtain peak values for each seed, and the overall peak value for all seeds. The range and average peak values of $\dot{\theta}$ and $\ddot{\theta}$ for each mean wind speed are shown in Figure 3-9. Although higher average pitch angles were observed at high Region 3 wind speeds, these wind speeds do not correlate with higher $\dot{\theta}$ or $\ddot{\theta}$ as expected based on the collective pitch schedule shown in Figure 3-3. The highest maximum pitch rate ($\dot{\theta}_{\max}$) and maximum pitch acceleration ($\dot{\theta}_{\max}$) are observed at low Region 3 wind speeds for both DLCs where the collective pitch schedule shown in Figure 3-3 is the steepest. In comparing the two DLCs, the higher turbulence in DLC 1.3 resulted in larger pitch motions and thus higher $\dot{\theta}_{\max}$ and $\ddot{\theta}_{\max}$ values across all above-rated mean wind speeds compared to that under DLC 1.2. Within the DLC 1.3 cases, $\dot{\theta}_{\max}$ and $\ddot{\theta}_{\max}$ values at $\overline{U}_{\text{hub}}$ = 12 m/s and $\overline{U}_{\text{hub}}$ = 14 m/s are over 100% greater than that at any other mean wind speed, indicating that highly turbulent low Region 3 wind conditions should be the drivers of determining peak pitch response requirements. The differences between DLC 1.3 and DLC 1.2 are the most pronounced at these mean wind speeds. Note that at $\overline{U}_{\text{hub}}$ = 10 m/s, only one seed for DLC 1.3 showed any pitch actuation while the other five seeds did not trigger pitch control over the full 400 s simulations. Between $\overline{U}_{\text{hub}}$ = 4 m/s – 8 m/s for DLC 1.3, no pitch actuation is observed. No DLC 1.2 seeds for $\overline{U}_{\text{hub}} \leq 10$ m/s resulted in any pitch actuation.

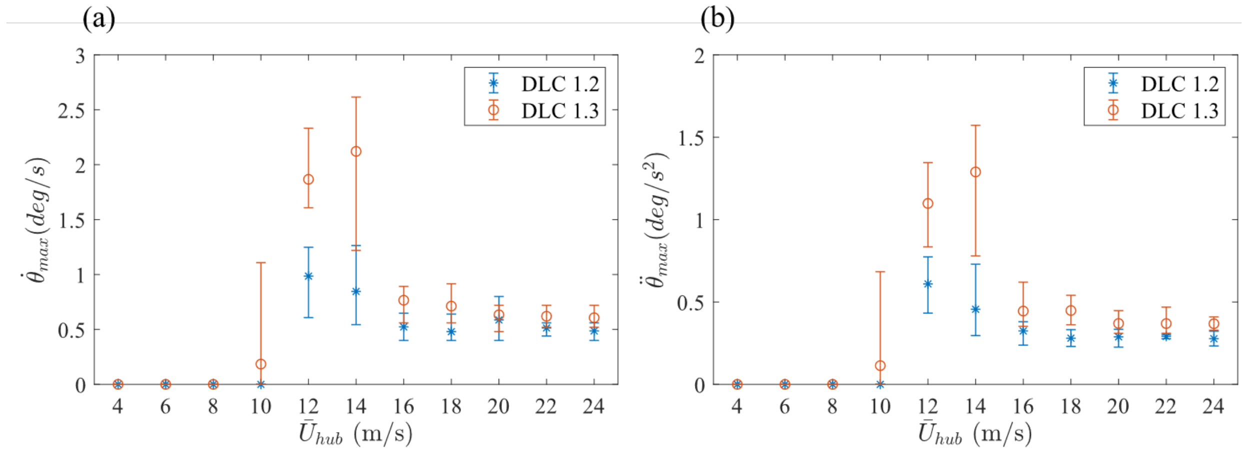

Figure 3-9. mean values (∗ and ◦) of maximum pitch rates and accelerations based on OpenFAST simulations for all DLC 1.2 and 1.3 cases. The mean values are averaged across all six seeds and the bars indicate the range of maximum pitch rates and accelerations from the six seeds at a given mean wind speed. a) Maximum pitch rate; b) maximum pitch acceleration.

Figure 3-10 shows the maximum pitching moment averaged across the six seeds ($\bar{T}_{\text{pitch,max}}$) at each mean wind speed. For mean wind speeds in below-rated conditions, there is larger variation in maximum pitching moment ($T_{\text{pitch,max}}$), but since no pitch motions were observed at these wind speeds, these results are omitted from Figure 3-10. However, turbines in real-world operation will undergo blade torsional deflections, especially at larger turbine scales. Although usually small compared to flap-wise and edge-wise deflections [97], torsional deflections can result in pitch actuation in Region 2 wind speeds in order to maintain optimal angle of attack along the blade. Simulating the blade torsional degree of freedom in future studies may be a useful consideration to better quantify pitch motions in Region 2 wind speeds and improve overall accuracy of pitch system requirements. Variation in $T_{\text{pitch,max}}$ is relatively small for a given above-rated wind speed as IPC reduces blade loads. For all Region 3 mean wind speeds, DLC 1.3 wind conditions resulted in higher $\bar{T}_{\text{pitch,max}}$ than DLC 1.2, about 21% on average across all $\bar{U}_{\text{hub}} > U_{\text{rated}}$. However, no clear trend in $\bar{T}_{\text{pitch,max}}$ with increasing mean wind speed ($\bar{U}_{\text{hub}}$) is observed.

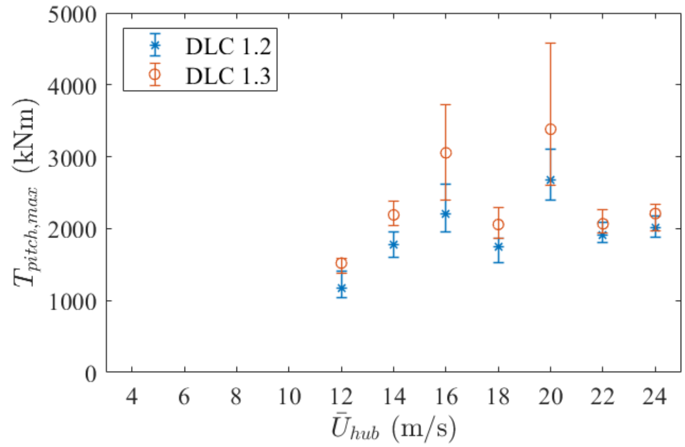

Figure 3-10. Maximum pitching moment magnitudes averaged across six seeds at each mean hub height wind speed from OpenFAST simulations for all DLC 1.2 and 1.3 cases.

3.3.2 Pitching power

The peak power consumed by the pitch actuator is then estimated using Eq. 3.1 based on the maximum pitch rate and blade pitching moment values computed for each seed at each mean wind speed under both DLCs. Peak pitch rates were estimated from the OpenFAST pitch response with central finite differencing. The maximum pitching power ($P_{\mathrm{pitch,max}}$) results are shown in Figure 3-11. Because $P_{\mathrm{pitch,max}}$ is proportional to peak pitch rate, the trends between the two parameters are similar. The highest $P_{\mathrm{pitch,max}}$ values are observed under DLC 1.3 at a mean wind speed of 14 m/s and correspond to a maximum of about 0.2% of the turbine's rated power, per blade, suggesting that the energy loss due to pitch control is relatively small. However, recall that pitch bearing friction is a significant component of blade pitch moment despite inaccurate models to predict its contribution [85]. Conservative estimates of pitch bearing friction increase the single blade pitching power percentage to around 1% of the turbine's rated power, still a relatively small energy loss due to pitch actuation.

While further detailed studies on the impact of pitch actuation on LCOE is necessary, the estimated cost of the pitch system relative to the total wind turbine costs can be made as a comparison. From Qin [98], the pitching system cost estimated from WISDEM for the NREL 5 MW reference turbine [93] and the IEA 15 MW reference turbine [99] predict pitch system Capital Expenditures (CAPEX) as 5.9% and 6.7% respectively. Thus, as a very rough estimate, if the pitch system is estimated to be around 6% to 7% of CAPEX, and CAPEX is estimated to be approximately 29% of the total turbine costs [100], the resulting pitch system capital costs are approximately 1.7% to 2% of total turbine costs. However, considering Operational Expenditures (OPEX), this value will be higher. Note that turbines that can significantly reduce costs (e.g. reducing mass by using a downwind rotor such as on the 25-DW2 turbine) may see the percentage of CAPEX from the pitch system increase to 10% to 15% [98]. Based on these estimates, the peak pitching power results suggest that the primary impact of pitch control on LCOE is the mechanical system cost.

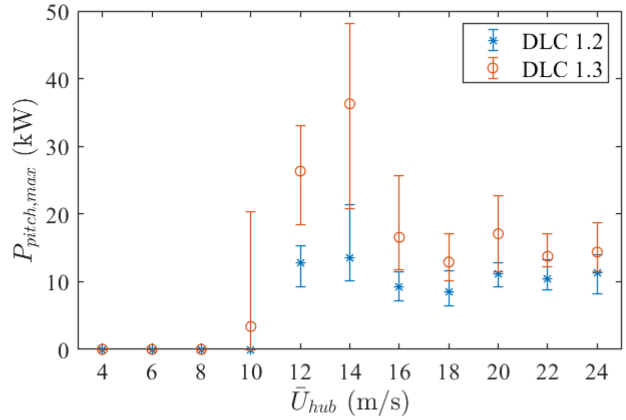

Figure 3-11. Maximum pitching power estimated using OpenFAST data for all DLC 1.2 and 1.3 cases.

3.3.3 Pitch Actuator torque

The total pitch inertia (I_{total}) is estimated using blade structural properties, OpenFAST results, and the CART-2 drive inertia scaling model described in Section 3.2.6. For the pitching inertia due to blade deflection (I_{defl}), although blade deflection varied with mean wind speed, the rigid blade pitch inertia (I_{pitch}) and pitch system drive inertia (I_{drive}) made up a significantly larger portion of I_{total}, ranging from 93% − 96% of I_{total} combined. This indicates that total pitch inertia can be estimated with just the I_{pitch} and I_{drive} components and additional contributions from I_{defl} are small. Although blade deflections in OpenFAST results do not significantly contribute to I_{total}, the simulations are still necessary in estimating peak pitching power and pitch actuator torque. The resulting I_{total} values remained similar across the simulated wind speeds with a mean value of 4.03 × 106 kg-m^2.

However, I_{drive} may be an overestimate at these extreme scales as reducing blade mass becomes much more critical for the design of extreme-scale turbines. While using the CART-2 pitch system ensures a conservative estimate, obtaining drive inertia data from larger turbines for Eq. 3.12 may result in more accurate I_{drive} estimates. With such data, pitch inertia due to blade deflections estimated by OpenFAST may be expected to contribute more to I_{total}. The lack of drive inertia data from larger turbines is a limitation of this study. While this data may come from existing turbines, detailed mechanical design of extreme-scale pitch systems can also provide estimates. However, such work is currently lacking in the literature beyond 2 MW and is recommended as future work [70].

Using Eq. **3.3**, the required maximum pitch actuator torque ($T_{act,max}$) is estimated and is shown in Figure 3-12. Although maximum pitching moment values are significant for mean wind speeds below-rated conditions, pitch actuator torque requirements are only investigated for above-rated wind conditions since blade pitch is held constant for below-rated wind speeds. In order to achieve the maximum pitch accelerations shown in Figure 3-9b, the required $T_{act,max}$ at each mean wind speed is greater than the blade pitching moment. At low Region 3 mean wind speeds, where the highest pitch accelerations are observed, a larger difference between maximum pitch actuator torque and maximum blade pitching moment is needed, up to about 5%.

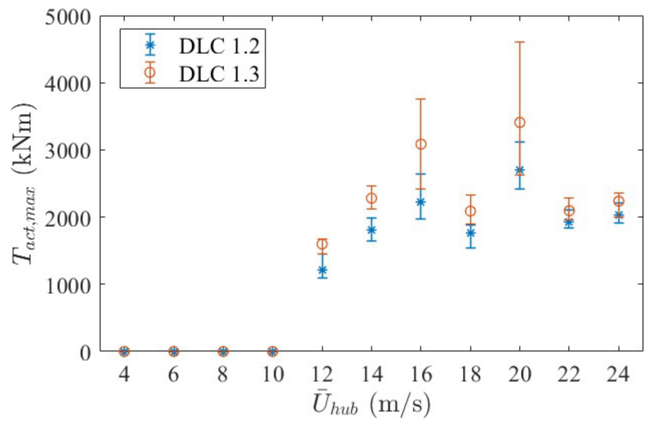

Figure 3-12. Maximum required pitch actuator torque estimated using OpenFAST data for all DLC 1.2 and 1.3 cases.

Although the maximum pitch rate and acceleration occurs at low Region 3 wind speeds, $T_{act,max}$ does not follow this trend as the amount of torque required to overcome the pitch inertia of the blade is much less significant than the moments due to aerodynamic and gravitational pitch loads. Consideration of blade geometry and flexibility in future rotor designs may help in balancing pitching moments and total pitch inertia such as to optimize costs and size of the pitch system. From this pitch system model, a pitch motor for a single blade should be rated to supply about 4000 kNm of torque for this 25 MW turbine in order to sufficiently respond to highly turbulent offshore wind conditions. However, when considering pitch bearing friction, the pitch motor rated torque would increase nearly proportionally to the increase in pitching moment due to pitch bearing friction. Overall, the OpenFAST simulations provided detailed insights into the pitch control requirements for the 25 MW turbine.

3.4 Analytical Scaling Method for Peak Pitch Requirements

The model developed in this study allows for estimation of pitch system requirements using computational analysis. However, generating turbulent inflow wind data for each specific turbine over a range of mean wind speeds and then running OpenFAST simulations for the tens of cases is time consuming. Therefore, an analytical scaling method is developed to quickly estimate pitching requirements based on OpenFAST predictions from multiple extreme-scale reference turbines. To derive this scaling method, further OpenFAST simulations are performed for five additional turbines under DLC 1.3 wind conditions for mean wind speeds in Region 3. Using these results, a power law is used to estimate the trends for maximum pitching moments due to aerodynamic, gravitational, and inertial effects ($T_{\mathrm{pitch,max}}$), maximum required pitch actuator torque ($T_{\mathrm{act,max}}$), and maximum pitching power $P_{\mathrm{pitch,max}}$ with a scaling factor defined as the product of blade mass (m_{bld}) and mean blade chord length ($\bar{c}$) to represent the blade structural pitch loads. Average chord was chosen as to be consistent with the typical definition of blade aspect ratio for a given rotor radius. Blade aspect ratio is useful in characterizing rotor aerodynamic and aeroelastic response [101]. Blade mass and inertia also tend to scale with average chord. Rotor solidity was considered as the scaling factor as well; however, a strong correlation was not observed.

The additional turbines included to investigate how peak torque and peak pitch vary with $m_{\mathrm{bld}}\bar{c}$ range from 5 − 50 MW. At the small end, the NREL 5 MW Reference turbine is used in both the original three-bladed version and a two-bladed version [93]. The two-bladed version has an adjusted chord distribution and blade mass density from the original model in order to maintain rotor mass and solidity. Both versions are simulated as downwind rotors. The SUMR-13i turbine is a 2-bladed, downwind design with a rated power of 13.2 MW [37]. An additional 25 MW turbine is simulated using the downwind SUMR-25 turbine [32]. The design of this rotor stems from an upscaling of the SUMR-13i rotor using power laws and defined scaling factors for different turbine components. Compared to the 25-DW2 design used in the remainder of this study, the SUMR-25 rotor has two blades that are slightly longer, about 30% lighter, and stiffer – particularly in the edgewise direction. The largest turbine used is the SUMR-50 rotor, a two-bladed, downwind design rated for 50 MW [63, 64].

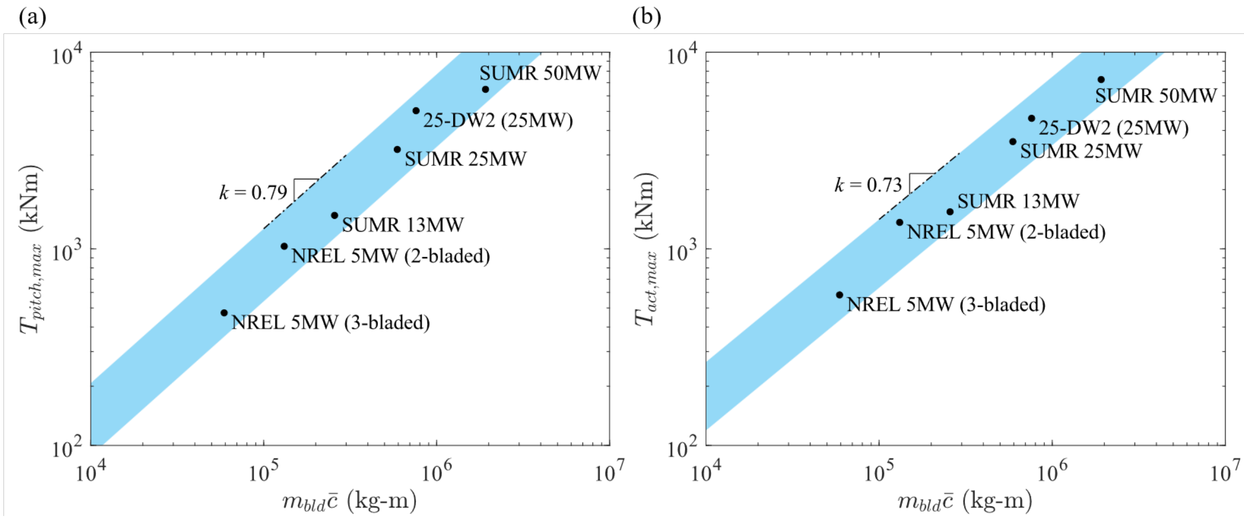

Figure 3-13. Power laws for a) maximum blade pitching moment; b) maximum pitch actuator torque. The blue banded regions mark the range of values where maximum pitching moment and actuator torque estimates fall within based on scaling with blade mass and average chord product.

The power law follows the form $T \propto (m_{\mathrm{bld}}\bar{c})k$ and both $T_{\mathrm{pitch,max}}$ and $T_{\mathrm{act,max}}$ are found to scale with $m_{\mathrm{bld}}\bar{c}$. The power law factor (k) is the slope of a best fit line on a log-log plot. While there are many aerodynamic, structural, and control variables involved that affect T_{pitch}, the OpenFAST data show $T_{\mathrm{pitch,max}}$ values to fall within the blue band illustrated in Figure 3-13a where k = 0.79. Translating the OpenFAST results into $T_{\mathrm{act,max}}$ estimates for each turbine, the data now align with a band where the power law factor k = 0.73 as shown in Figure 3-13b. This decrease in k is due to the higher maximum pitch acceleration that the smaller turbines achieve, resulting in a proportionally higher pitch actuator torque required than for the larger turbines under the same turbulent wind conditions.

While pitch motor specifications for commercial turbines greater than 5 MW was not available, a rough comparison can be made for $T_{\mathrm{pitch,max}}$ predictions using estimates based on pitch motor rated power values of commercial pitch motors from turbines rated for 1.5 MW and 2.5 MW [102]. Assuming the same tip-speed ratios as the NREL 5 MW reference turbine [93] and a wind shear exponent of 0.2, pitch actuation torque is estimated from Eq. **3.3** where maximum pitch rate is the direct result of change in wind speed across rotor diameter due to shear. The resulting estimated pitching moment for the 1.5 MW and 2.5 MW turbines are 195 kNm and 424 kNm respectively. Although $m_{\mathrm{bld}}\bar{c}$ is not available these two turbines, the estimates suggest that the pitch requirement predictions are of matching order of magnitude.

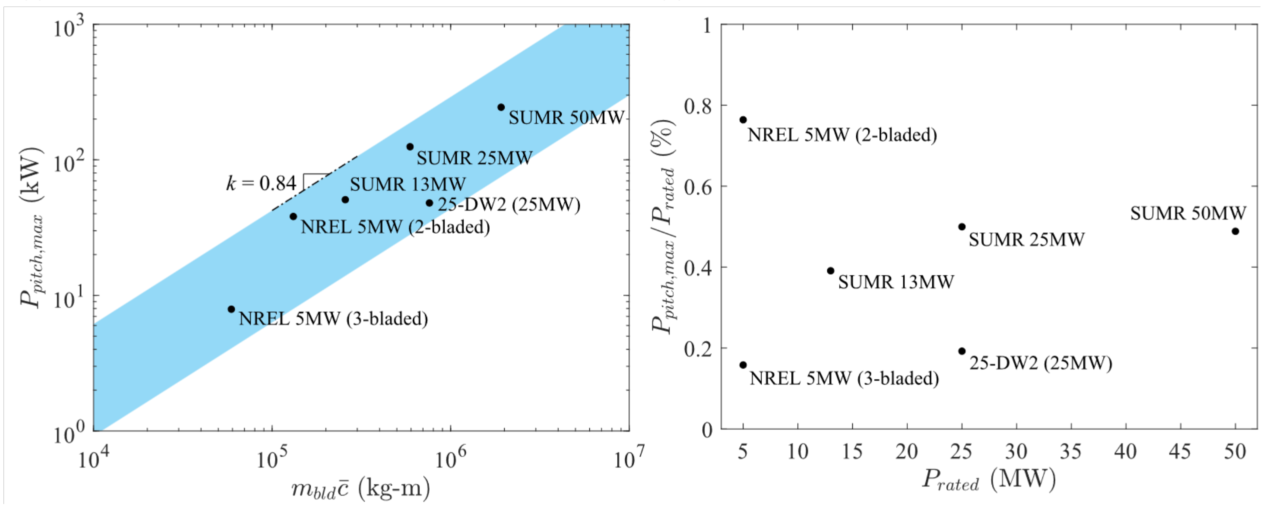

Figure 3-14. a) Power law for maximum pitching power per blade; b) maximum pitching power per blade relative to the turbine's rated power expressed as a percentage.

The maximum pitching power scaling is shown in Figure 3-14a and scales reasonably with $m_{\mathrm{bld}}\bar{c}$ for $k = 0.84$. Because $P_{\mathrm{pitch,max}}$ is also a function of the maximum pitch rate, the scaling falls within a wider band than in Figure 3-14a and Figure 3-14b as there is not a strong trend in maximum pitch rate with turbine or blade size. If the portion of total pitching moment from pitch bearing friction is assumed independent of turbine size, the three k values are expected to hold with pitch bearing friction included since required pitch actuator torque and pitching power are both strong functions of pitching moment. While $P_{\mathrm{pitch,max}}$ increases with $m_{\mathrm{bld}}\bar{c}$, relative to the rated power of the turbine, it remains on the same order of magnitude as turbine size grows. Figure 3-14b shows the proportion of a turbine's rated power that pitching power requires maximally as a percentage. None of the turbines required more than 1% of the turbine's rated power with the most at 0.76% for the two-bladed NREL 5 MW turbine. Interestingly, $P_{\mathrm{pitch,max}}/P_{\mathrm{rated}}$ is consistently higher for the two-bladed turbines compared to the three-bladed turbines. However, only two three-bladed turbines are used in this study (the three-bladed NREL 5 MW turbine and the 25-DW2 turbine) and the differences in pitching power between two-blade and three-bladed turbines should be further studied to assert this conclusion. The scaling law developed in this study provides a quick method for estimating peak pitching moments and pitch actuator torques based on blade mass and chord length. This approach simplifies the process of sizing pitching systems for large-scale wind turbines, supporting efficient and cost-effective turbine design.

3.5 Conclusions

As wind turbine scales increase, the longer, more flexible, and heavier blades require robust pitch systems to pitch blades quickly and precisely, especially in higher wind speeds and greater extreme turbulence levels found offshore. In this study, pitch system requirements for a 25 MW downwind offshore turbine with advanced blade pitch control are explored. A model for estimating peak pitching power and pitch actuator torque is developed and presented. In estimating pitch actuator torque, a scaling model for blade pitch inertia is developed that considers aeroelastic effects and pitch system dynamics. Highly turbulent Region 2 and 3 wind conditions are considered to predict maximum pitch rates/accelerations and blade pitching moments using coupled simulations. A Case study of a 25 MW turbine is presented using the developed model. The turbine is simulated using the OpenFAST code under DLC 1.2 and DLC 1.3 turbulent wind conditions and the results are used to estimate maximum pitch rates and accelerations.

The maximum pitch rates and accelerations predicted both peak in low Region 3 mean winds under DLC 1.3, highlighting these wind conditions as critical for determining peak pitch response requirements. Peak pitching power followed the same trend, peaking at a mean wind speed of 14 m/s. The peak pitching power for each blade suggests that the energy consumption impact due to pitching is weak. Although pitch bearing friction is not included due to the complexity in predicting its contribution to the pitching moment, conservative estimates still indicate pitch actuation to only consume a small amount of energy compared to the turbine's rated power. However, pitch systems can be significant capital and operational cost components of wind turbines, scaling with the rated torque requirements. Maximum pitch actuator torque peaks at higher Region 3 wind speeds, correlating with maximum pitching moments, as pitching moment contributed much more significantly to maximum pitch actuator torque than blade pitch inertia. The peak pitch requirements of additional reference turbines ranging from $5 - 50$ MW are explored using the same methodology. The results are utilized in developing an analytical power scaling law that approximately relates the product of blade mass and mean chord length to pitching moment, pitch actuator torque, and pitching power. This scaling law offers a quick method for estimating peak pitching moment and pitch actuator torque solely based on blade gross properties without requiring extensive simulations for various wind conditions.

This study offers new insights into pitch actuator power and torque requirements by studying the peak pitch responses of six different megawatt-scale reference turbines in highly turbulent wind conditions. It is recommended that subsequent studies should connect the pitching power and torque requirements to capital and operating costs, so the direct impact on LCOE can be captured, perhaps using regression analysis between rated torque and mass for typical electric pitch motors. Pitch bearing friction effects should be considered for such analysis. Further OpenFAST simulations may use the BeamDyn module for structural dynamics in order to account for the blade torsional degree of freedom. Additional wind conditions may be considered in OpenFAST simulations to include a broader range of inflow wind that turbines will need to handle such as extreme gusts or shut-down conditions. While this study assumed electric pitch systems, additional work is recommended for comparing the results of this study with estimates based on hydraulic systems to determine its applicability to hydraulic pitch systems. Furthermore, detailed mechanical design studies of pitch systems at these extreme scales will refine total pitch inertia estimates that improve the accuracy of the methodology used herein. Lastly, future work may consider trade-offs involving pitch control type, rotor orientation, yaw effects, or floating platforms to refine pitch actuator torque requirements further.

Chapter 4

Effects of Freestream Turbulence on Energy Harvesting of a Single Semi-Passive Oscillating Hydrofoil

Abstract

Riverine environments pose challenges for renewable energy device deployment due to shallow depths and variable, unsteady flow conditions. Vertically oscillating hydrofoil turbines appear well suited for such environments, able to accommodate changing depth conditions while potentially providing high efficiency and reduced impact on wildlife due to lower tip speeds. However, no studies have yet been published on the impact of freestream turbulence on oscillating hydrofoil turbine performance. In this study, a semi-passive hydrofoil turbine is experimentally tested in a water channel, operating at Reynolds numbers based on chord length and freestream velocity ranging from 69,000 to 91,000. To compare with conventional channel inflow conditions, data was also taken with a passive turbulence grid placed upstream to generate a nearly uniform turbulence intensity profile. In both cases, the velocity field just upstream of the hydrofoil was first characterized using hot-wire anemometry without the hydrofoils present. Baffle boards were placed on the top of the channel to mitigate free surface effects. Experiments with the hydrofoil powered by the flow were then conducted with and without the turbulence grid over a range of flow speeds to obtain kinematic data (pitch and heave) and vertical force data. The results indicate that increased turbulence levels enhance power production by increasing heave velocities and vertical forces throughout one oscillation period. The majority of these benefits are observed on the downstroke where the hydrofoil sees increased heave range and speed due to gravity and inertia. As a result, hydrodynamic efficiency was observed to increase by up to 12% due to the addition of the turbulence grid and the device was able to achieve a maximum hydrodynamic power efficiency of 52%.

4.1 Introduction

The modern-day demand for electricity requires substantial and consistent generation capabilities from renewable energy sources to reduce the consumption of fossil fuels. The intermittency of renewable energy sources like solar and wind necessitates harvesting energy from a variety of sources that can have reduced intermittency. Environments like rivers provide opportunities for more consistent power delivery to further increase renewable energy capacity at local and global scales. As compared to hydropower, such hydrokinetic technologies may be more minimally invasive relative to natural stream flows.

However, riverine environments are particularly challenging for hydrokinetic technologies due to shallow depths relative to their widths (with depths typically less than 5% of width) and potentially vastly different flow conditions from season to season (with average flow rates and depths in a given month varying by more than two-fold over the year) [10]. Employing conventional rotary turbines in such conditions is difficult since coverage is limited to circular swept areas that do not adapt well to complex and shallow bathymetry of rivers and cannot efficiently take advantage of confinement effects. In addition, the fixed circular swept area of a rotary hydrokinetic turbine becomes problematic in handling seasonal variations in river depth. Furthermore, rotary turbine blades are designed to produce a steady lift force and thus require high tip-speed ratios to maintain high efficiencies. To maximize efficiency, these types of hydrokinetic turbines tend to operate at tip-speed ratios ranging from 4 to 6, which in higher-speed rivers with up to 2 m/s flows, results in tip speeds that can approach 10 m/s [10, 11]. Such tip speeds pose significant threats to riverine wildlife. To that end, hydrokinetic turbines that use oscillating hydrofoils are well-suited for riverine environments [12, 103]. These turbines can produce high energy extraction efficiencies at low tip speeds and have scalable, rectangular swept areas that are less sensitive to changes in river depth [12]. In addition, they avoid design and structural complexities associated with rotating blades that require varying angles of attack along the length of the blade [12]. By having no twist or varying chord distribution, these hydrofoils can be designed manufactured much more simply than typical wind turbine blades. Regardless, note that codes like PROPID [35] cannot be used for oscillating hydrofoil design as it only uses models for steady aerodynamics and does not consider the unsteady Leading-Edge Vortex Shedding (LEVS) that is an important mechanism in high efficiency hydrofoil performance. Lastly, conventional rotary turbine blades require continuous flow attachment (minimal flow separation) while operating at high angles of attack. The high levels of turbulence in a riverine environment can cause the flow to separate, thereby reducing performance [104], and can increase fatigue since the blades are generally unsupported at their tip [105].

Oscillating hydrofoil turbines use the concept of unsteady lift to induce periodic pitching and heaving hydrofoil motions that can be converted into electricity via a power take-off system. The underlying concept of unsteady lift is learned from biological swimmers that use similar pitching and heaving motions to produce thrust at high efficiencies [106]. A quasi-steady analysis of a hydrofoil angle of attack under sinusoidal pitching and heaving motions shows that a large nominal pitch angle (θ_0) can be chosen such that the vertical component of the resultant force on the hydrofoil changes sign, allowing the hydrofoil to translate vertically (heave) in the same direction as the force and extract energy in the flow as opposed to produce thrust [14]. Instead of a steady attached flow, oscillating hydrofoils have a continuous flow separation and a shedding flow cycle whereby the influence of Leading-Edge Vortex Shedding has been identified as an important and beneficial characteristic in boosting power generation by allowing higher peak vertical forces on the hydrofoil than would be with steady hydrodynamics [12]. The suction induced by lower pressure vortices shedding and staying near the hydrofoil produces increases in vertical forces that in turn generate more power. Notably, 2-D numerical simulations have indicated that high-efficiency kinematics can be obtained regardless of LEVS as hydrofoil kinematics allowing for continuous flow attachment have still shown high power production [13]. However, 3-D simulations and experiments generally include LEVS for high power efficiency [108].

Different activation methods exist for oscillating hydrofoil operation. Sinusoidal kinematics (pitch and heave motions) are the conventional basis of the oscillating hydrofoil turbine concept and are most often used in both experimental and computational literature [13–15, 19, 22, 23, 107–112]. To achieve mathematically sinusoidal kinematics, both the heave and pitch motions are fully prescribed. Fully prescribed motions are useful for parametric studies where hydrofoil kinematics can be changed precisely to evaluate its impact on power extraction performance. In doing so, high hydrodynamic efficiencies, approaching the Betz limit, have been observed [15]. However, for practical applications, both degrees of freedom cannot be prescribed to generate power from the flow. At the other extreme, a fully passive system requires no input power as both pitch and heave motions are induced through instabilities caused by the flow [113]. Such systems are advantageous since pitch actuation is avoided and all power generated from both the heaving and pitching motions is net positive. However as both degrees of freedom are passive, the kinematics and thus energy harvesting performance is more sensitive to changes in flow conditions [113]. A semi-passive system allows for just the pitch degree of freedom to be actively controlled similarly to how wind turbine blades are cyclically pitched in operation. The resulting heave is determined by interactions between the fluid and hydrofoil. Electricity can then be generated from these fluid-structure interactions in the heave direction by using a Power Take-Off (PTO) system with a mechanism such as a Mechanical Motion Rectifier that converts oscillatory hydrofoil motions into unidirectional rotation [127]. Such a semi-passive system minimizes pitch actuation complexity while allowing indirect control of the heave range needed to adapt to changing river depths and speeds. As such, a semi-passive system is deemed the most viable oscillating hydrokinetic system for utility-scale riverine applications. However, one must account for the power required for semi-passive pitch actuation needs in the net energy harvested. Thus, minimizing pitch actuation power relative to heave-producing power is an important consideration in hydrofoil hydrokinetic design [16].

Existing literature on semi-passive systems is mostly computational, although some experimental work has also been published. Early numerical work on semi-passive devices used inviscid potential flow models to identify the mechanisms by which semi-passive activation extracts power from the flow [114]. However, this potential flow model could not consider LEVS and thus was limited to small pitch amplitudes. When considering viscous effects, it is important to characterize the hydrofoil Reynolds numbers, which can be defined based on fluid density (ρ), chord length (c), undisturbed flow velocity at the hydrofoil plane (U_{HP}), and fluid viscosity (μ) as

$$\mathrm{Re} = \frac{\rho U_{HP} c}{\mu} \qquad \text{Eq. 4.1}$$

Two-dimensional computational studies at low Reynolds numbers (Re ~ 1000) have investigated the effects of non-sinusoidal pitch kinematics that tend toward trapezoidal pitch motions [17, 115]. Results from these studies for a variety of pitch motions produced maximum hydrodynamic efficiencies of around 32 − 33%. A semi-passive system in shear flows was studied computationally at Re ranging from 50,000 to 200,000 and showed a decrease in efficiency when shear was introduced in the flow due to the lower velocity regions. A “block” mechanism was proposed to limit downward heave ranges, leading to increased maximum observed efficiencies of 51% based on heave and 49% after accounting for pitching power losses for a two-dimensional simulation [116]. Another computational investigation of a semi-passive system that captured LEVS observed that positive power output is dominated by vortex shedding dynamics and the net moment on the hydrofoil at the top of the heave range reduces the power required for semi-passive pitching [117]. In general, efficiencies for three-dimensional systems are expected to be lower than those for two-dimensional numerical systems due to finite hydrofoil span lengths [107]. Laboratory-scale semi-passive device experiments at Re = 45,000 for a hydrofoil with a 0.1 m chord and a nominal pitch angle $\theta_0 = 62^{\circ}$ (similar to the kinematics used in the present study) have been published [118]. However, the hydrofoil pitch axis was linked by aluminum rods to a primary pivot axis such that the hydrofoil heaving motion followed an arc trajectory rather than a conventional linear trajectory. These experiments reported a maximum hydrodynamic efficiency without pitch power of about 30%, which was reduced to 24% once accounting for the losses due to measured input power for pitching. The largest scale semi-passive device to date is the full-scale 150 kW Stingray device by Engineering Business Ltd. in the United Kingdom which operated at Re = 6,000,000 [119]. This device similarly followed an arc trajectory for hydrofoil heaving motions. However, due to the limited pitch angle range of the device, the mechanical efficiencies achieved by the Stingray fall far below theoretical limits at about 12% based on a swept area of 195 m^2 [120].

While much of the literature on oscillating hydrofoil turbines focuses on locating optimal operation points, little work considers the nature of the flow on energy extraction efficiency. Riverine flow conditions are inherently nonuniform and unsteady with potential field-sites reaching flow speeds up to 3.3 m/s during the summer months [10]. Turbulence intensity levels are also significant in field-site conditions. Sites along the Kvichak River located in Alaska have been measured to reach turbulence intensity levels of about 20% [26]. Only two studies have been published that experimentally investigate the effects of freestream turbulence on hydrokinetic turbine efficiency: one for a horizontal rotary system [121] and one for a vertical rotary system [104]. However, there have been no experimental studies that investigated the impact of turbulence on the oscillating hydrofoil turbine power efficiency.

The influence of riverine flow conditions on oscillating hydrofoil turbine performance is crucial in developing full-scale devices. This paper is the first to experimentally quantify the effects of freestream turbulence on a semi-passive oscillating hydrofoil performance for energy harvesting. Experiments were performed in the water channel facility at the University of Virginia (UVA). The hydrofoil testing apparatus was designed and built in-house and was equipped with sensors to measure the vertical forces on the hydrofoil as well as hydrofoil kinematics (pitch and heave motions). This testing apparatus is the first to incorporate a vertical rail system that allows for passive linear heaving, rather than the arced heaving mechanism used in the few existing studies on experimental semi-passive systems [118, 119]. Turbulence levels were increased within the channel using a passive turbulence grid placed upstream of the hydrofoil and quantified through hot-wire anemometry. Results from these experiments illustrate how freestream turbulence and flow velocity change hydrofoil kinematics, vertical forces, power and hydrodynamic efficiency. High hydrodynamic efficiencies of up to 52% were observed, rivaling results from 2-D numerical simulations [12]. No other experimental studies with semi-passive systems achieving such high efficiencies have been found. Only two experimental studies have observed similar efficiency levels, but only fully passive or fully prescribed systems were used where losses due to input power were not considered [22, 122]. This study presents novel insights that should be considered in designing full-scale oscillating hydrofoil systems that will need to operate in varying levels of turbulence found in real-world riverine environments. The following sections will cover theoretical considerations (Section 4.2), experimental facility and water channel flow characterization (Section 4.3), the oscillating hydrofoil experimental results (Section 4.4), and conclusions (Section 4.5).

4.2 Oscillating Hydrofoil Turbine Parameters

The motion of an oscillating hydrofoil can be described as a combination of two degrees of freedom: heave and pitch. Heave is the vertical displacement of the hydrofoil and pitch is the rotation of the hydrofoil about its pitch axis. By actively controlling the pitch angle (θ) over the course of a period, the heave vertical position (H) is passively controlled due to the resulting vertical forces acting on the hydrofoil, allowing for the conversion of mechanical power to electricity via a power take-off system. For a semi-passive system, positive power is generated from the heaving motion while active pitch control consumes power and thus reduces the net mechanical power generated. Therefore, the instantaneous total mechanical power is the summation of the net power from both the heaving motion (which is generally positive) and the pitching motion (which is generally negative) as shown in Eq. 4.2. The mean mechanical power over one period (P_{tot}) is calculated using a time average as described in Eq. 4.3 based on the average power from the heaving motion (which is positive) and the average power from the pitching motion (which is negative).

$$P_{\text{tot}}(t) = P_H(t) + P_\theta(t) \qquad \text{Eq. 4.2}$$

$$\overline{P_{\text{tot}}} = \overline{P_H} + \overline{P_\theta} \qquad \text{Eq. 4.3}$$

The heave component of mechanical power is measurable using data obtained from the vertical forces and displacement of the hydrofoil (described in subsequent sections) and is calculated as the product of the resultant vertical force on the hydrofoil (F_Y) and the heave velocity ($\dot{H}$).

In this study, the pitch actuation power consumption data was not directly obtained. Therefore, a pitching power fraction (p_{loss}) is used to estimate the relative power loss from pitching to include losses due to pitch control (Eq. 4.4).

$$\overline{P_{\text{tot}}} = (1 - p_{loss})\overline{P_H} = (1 - p_{loss})\overline{F_Y(t)\dot{H}(t)} \qquad \text{Eq. 4.4}$$

$$\overline{P_{\text{tot}}} = 0.8\overline{P_H} \qquad \text{Eq. 4.5}$$

In this study, p_{loss} is set to 0.2 corresponding to an estimated 20% loss in cyclic average power due to pitching over one period (resulting in Eq. 4.5). This fractional loss is based on a wide range of oscillating hydrofoil numerical and experimental results from Lehigh University which consider the same hydrofoil shape, heave-to-chord ratios and Strouhal numbers [123]. The percent loss due to pitch actuation has been shown to vary significantly with hydrofoil kinematics (heave-to-chord ratio, nominal pitch angle, sinusoidal/non-sinusoidal kinematics), but the p_{loss} used in this study falls within the typical range of values observed in the literature for cases with relatively similar kinematics [13, 17, 112, 115].

Since oscillating hydrofoil devices operate based on the concept of unsteady lift, it is useful to consider the changing angle of attack of the hydrofoil as it oscillates in the flow. Given the pitch and heave velocity as a function of time, the angle of attack (α) can be calculated as shown in Eq. 4.6.

$$\alpha(t) = \theta(t) - \tan^{-1}\left(-\frac{\dot{H}(t)}{U_{HP}}\right) \quad \text{Eq. 4.6}$$

A vertical force coefficient (C_H) is defined in order to nondimensionalize the heave force as shown in Eq. 4.7 where s and c are the hydrofoil span length and chord length respectively.

$$C_H = \frac{F_Y}{0.5\rho U_{HP}^2 sc} \quad \text{Eq. 4.7}$$

Similarly, the heave-based power coefficient is defined in order to nondimensionalize heave mechanical power as shown in Eq. 4.8.

$$C_{PH} = \frac{\overline{P_H}}{0.5\rho U_{HP}^3 sc} \quad \text{Eq. 4.8}$$

This represents the heave-based power based on the span area of the hydrofoil.

The hydrodynamic efficiency (η_{hydro}) is used to assess an oscillating hydrofoil system's ability to extract the power available in the incoming flow over a swept region. This is defined as the ratio of the mean mechanical power generated over one period to the available power from the river within the hydrofoil swept area. This swept area is the product of the span and a vertical swept distance. This vertical distance is sometimes defined as the vertical distance traversed by the pitch axis, but it is often more stringently defined as the larger vertical distance traversed by the trailing edge of the hydrofoil [124]. For this study, the latter definition based on the trailing-edge is employed since large pitch angles are employed, which yield significant excursions relative to the pitch axis. The pitch axis was set at one third of the chord (c) behind the leading edge in this study, to be consistent with the experiments by Lehigh University [123]. The trailing-edge swept distance (d) is then calculated based on the pitch and heave kinematics, yielding the hydrodynamic power efficiency defined in Eq. 4.9

$$\eta_{\text{hydro}} = \frac{\overline{P_{\text{tot}}}}{\frac{1}{2}\rho U_{HP}^3 ds} \quad \text{Eq. 4.9}$$

The limit of hydrodynamic efficiency is typically governed by the Betz limit as described by actuator disk theory for the maximum extractable power from a flow based on the swept area in an unbounded domain [125]. However, the hydrodynamic efficiency may exceed the Betz limit for conditions where flow confinement is present [125].

The last two relevant parameters defined here are the heave-to-chord ratio and the trailing-edge distance-to-chord ratio shown in Eq. 4.10 and Eq. 4.11 respectively. The definitions of H_0 and d are shown in Figure 4-2.

$$H^* = \frac{H_0}{c} \qquad \text{Eq. 4.10}$$

$$d^* = \frac{d}{2c} \qquad \text{Eq. 4.11}$$

The nominal heave distance (H_0) is defined as the cycle-averaged peak heave amplitude measured at the pitch axis relative to the average vertical position. Since the trailing-edge swept distance (*d*) is defined as the total vertical distance traversed by the trailing edge, a factor of 2 is included to represent the distance relative to the average vertical position, which allows H^* and d^* to be both be defined based on the excursions from the average vertical position. In general, a large H^* has the advantage of reducing chord length (and thus hydrofoil blade mass) for a given swept area, but a larger H^* requires an increase in the blade pitch angle and actuation, which can reduce hydrodynamic efficiency for $H^* > 2$ [124, 126].

The last relevant parameter used in describing oscillating hydrofoil kinematics is the Strouhal number (St), which characterizes the frequency of the hydrofoil oscillations relative to that of the freestream flow over the vertical trailing-edge swept distance as expressed in Eq. 4.12 [113].

$$\mathrm{St} = \frac{fd}{U_{HP}} \qquad \text{Eq. 4.12}$$

The Strouhal number is useful since it can be adjusted to ensure that LEVS from the hydrofoil contributes to high efficiency hydrofoil kinematics. High hydrodynamic efficiency has been shown experimentally to occur at Strouhal numbers in the range of 0.2 to 0.4, where lower heave-to-chord ratios ($H^* = 0.75$) have lower optimal St values [15].

4.3 Experimental Methodology

4.3.1 Hydrofoil Testing Apparatus Design

The testing apparatus (shown in Figure 4-1) was designed to allow the hydrofoil to move freely in the vertical direction while restricting its motion in the flow direction. To achieve this, a rectangular frame was constructed and mounted within the working section of the water channel, to minimize obstruction to the flow. The frame is made from 80/20 aluminum extrusions (manufactured by OpenBuilds) with dimensions of 80 mm in width and 20 mm in thickness, yielding a net flow cross-section area reduction of about 15%. Both the width and height of the frame were matched to the dimensions of the water channel test section, allowing it to be securely clamped in place. This configuration created a water passage that positioned the hydrofoil within the central plane of the frame.

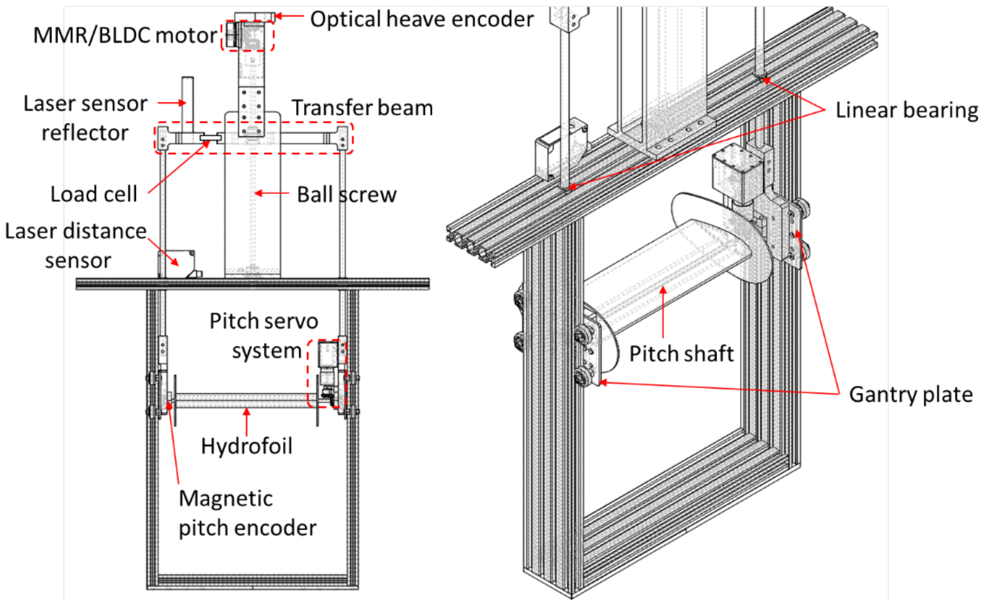

Figure 4-1. CAD model of hydrofoil testing apparatus.

The hydrofoil was mounted on two V-Slot gantries (OpenBuilds), with ball bearings on each side to support the hydrofoil. The gantries were constrained by four wheel-rollers fitted into the V-slots of the 80/20 beam, enabling free movement along the beam while limiting other degrees of freedom. The gantries were connected to the transfer beam via individual aluminum rods, which transfer the hydrofoil's heaving motion to the beam. Each rod was supported by a linear bearing mounted on the frame to ensure stability and smooth vertical movement. The laser sensor reflector was mounted on the transfer beam to measure the hydrofoil's heaving displacement for pitch control. Additionally, a 500 g Uxcell parallel load cell was installed on the transfer beam to measure the net vertical force on the hydrofoil simultaneously. A miniature magnetic pitch encoder (RLS) was integrated into the gantry assembly to record the hydrofoil's instantaneous pitch angle. The pitch encoder data was combined with the heave position data for calculating the hydrofoil's full swept trailing-edge distance (d) shown in Figure 4-2, which typically ranged from about 167 mm to 204 mm.

A ball screw (THK) was used to convert translational motion into rotational motion by back-driving the nut. The resulting rotational motion was transmitted to an EC 45 *flat* brushless DC motor (Maxon), functioning as a generator, through a Mechanical Motion Rectifier (MMR) [127]. The MMR converts the bi-directional rotation into a uni-directional output, preventing the DC motor from reversing direction when the hydrofoil changes heave direction. The ball screw, MMR, and DC motor were mounted on a 3D-printed stand (see Figure 4-1), which was carefully aligned and attached to the top beam of the frame. While the hydrofoil's heaving speed could be calculated using the time derivative of the laser displacement measurement, this approach introduces significant error due to the high noise levels of the laser sensor. To mitigate this issue, an optical encoder (US Digital) was installed at the top of the ball screw to measure the angular position of the ball screw (to be converted into heave position and velocity), providing a more accurate calculation of the heaving speed.

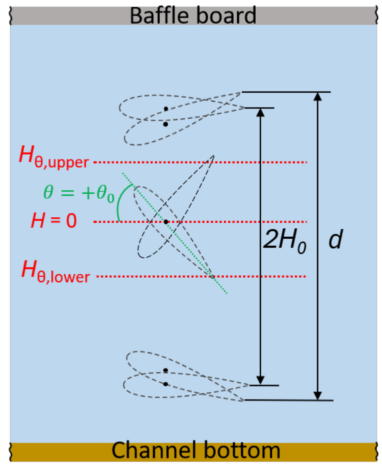

Figure 4-2. Heave position limits for pitch control used on the hydrofoil testing apparatus (not to scale). The definitions of nominal heave range, trailing-edge distance, and positive nominal pitch angle are also denoted.

To create oscillatory heaving motions, the hydrofoil pitch angle was actively controlled via the pitch servo system shown in Figure 4-1. Pitch motion of the hydrofoil was driven by the pitch servo system which consists of a PTK-170S servo motor (AMain Hobbies) and a pair of metal miter gears (McMaster-Carr). The miter gears allowed for a 90-degree redirection of the pitch drive, optimizing space utilization. The pitch was actuated when the laser sensor noted that the heave had reached the target upper limit ($H_{\theta,\text{upper}}$) or target lower limit ($H_{\theta,\text{lower}}$). Upon actuation, the pitch angle changed from -60° to +60° and then back. The house of the servo was fabricated by an in-house 3D printer (Stratasys F370) and waterproofed with an elastomer infiltration method [106]. This pitch control method results in very fast pitch rotation with peak pitch rates around 13 rad/s. Note that this approach can be expected to consume more power due to the high pitch angular accelerations required than a more typical sinusoidal pitch motion. There was no assumed phase difference between the pitch and heave motions.

The pitch control of the hydrofoil was managed using an Arduino MKR Zero microcontroller. A custom control algorithm was developed to define the heaving motion (illustrated in Figure 4-2) using filtered laser sensor data. For operation, heave limits for pitch control were set narrower than the desired heave range as the hydrofoil would otherwise heave beyond these limits due to inertia and gravity as depicted in Figure 4-2. The noisy raw laser sensor data was filtered in real-time using a Kalman filter to use in the pitch control. The servo motor was programmed to reverse the hydrofoil's pitch angle dynamically when these heave boundaries are reached.

Pitch control included a 60° nominal pitch angle (θ_0) for all cases and a target ± 10 mm heave condition about the heave center location ($H = 0$) was used for the pitch control system, i.e. $|H_{\theta,\mathrm{upper}}| = |H_{\theta,\mathrm{lower}}| = 10\ \mathrm{mm}$. Due to inertia, gravity, and system latency, the actual heave range of the hydrofoil surpassed the target range of ± 10 mm in both directions (especially in the downward direction) but these particular target values were set to maximize the hydrofoil's heave range without approaching the baffle boards and the channel bottom within one chord length.

The connection diagram of the experimental setup is shown in Figure 4-3. Simultaneous data acquisition of key performance metrics, including the hydrofoil's pitch angle, heaving displacement, vertical force, and the angular position of the ball screw, was conducted using the cDAQ-9174 data acquisition system from National Instruments. The data then was collected via an in-house written code using the LabView software (National Instruments).

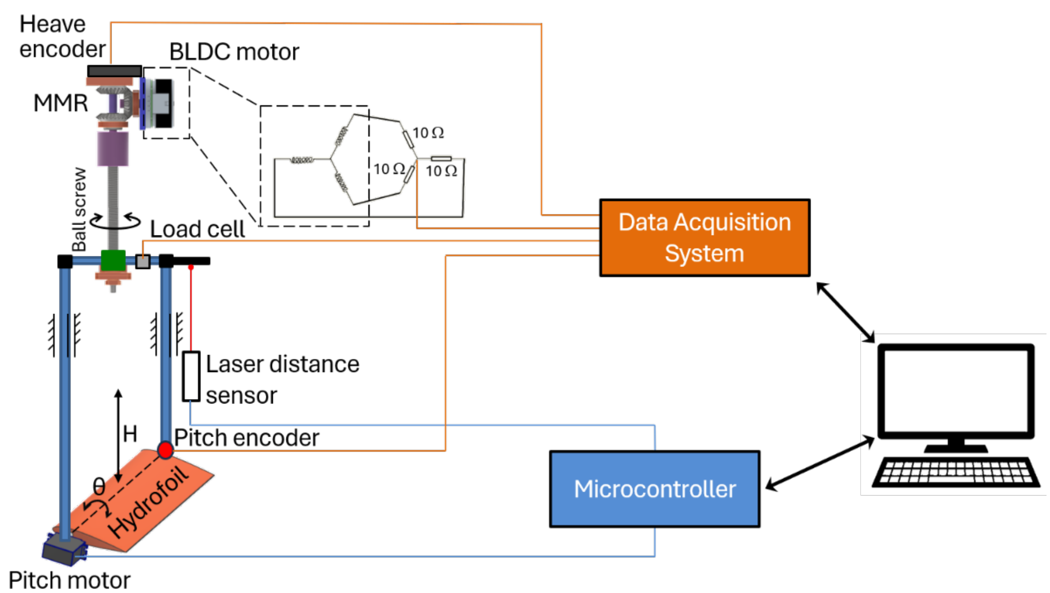

Figure 4-3. Experimental setup sensors and actuation connection diagram.

This setup enabled precise synchronization of measurements for comprehensive analysis. The pitch control system was separately connected to a computer for power and implementation of the pitch control algorithm. While voltage from the back-driven brushless DC motor could also be measured, this study focuses on hydrodynamic performance and thus presents experimental data on mechanical power and efficiency and does not include analysis of MMR dynamics or efficiency. Additionally, the three 10 Ω resistors connected to the output of the BLDC motor (shown in Figure 4-3) to limit generator load result in increased resistance to the hydrofoil heaving motion. For the experiments performed in this study, the resistive load was configured to balance out heave forces and maximize heave range within the test section without contacting the baffle boards and water channel bottom at the higher flow speeds achievable.

Additional work should look to optimize the resistance in this circuit to maximize hydrodynamic efficiency when considering the full mechanical-to-electrical efficiency of the system.

The hydrofoil installed in the testing apparatus was 3-D printed from Nylon 12 as shown in Figure 4-4. A 6 mm aluminum shaft was inserted through the pitch axis on which a miter gear was attached to allow the pitch servo motor to actuate pitch angle (shown in Figure 4-1). Endplates that are 2 mm thick were attached at each end of the hydrofoil and extended *c*/3 outward from the hydrofoil profile. Specifications of the hydrofoil are shown in Table 4-1.

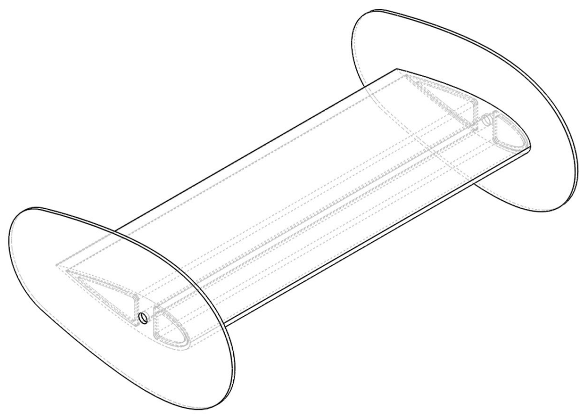

Figure 4-4. NACA0025 hydrofoil with endplates used in experiments.

Table 4-1. 3-D printed hydrofoil specifications.

Parameter	Value
Profile	NACA0025
Chord	100 mm
Pitch axis location	1/3c
Pitch shaft diameter	6 mm
Hydrofoil Aspect ratio	2.54
Material	Nylon 12
Mass	0.18 kg
Endplate thickness	2 mm

Two-dimensional numerical simulations have predicted increased hydrodynamic efficiencies with increased hydrofoil thickness up to 25% when using four-digit symmetrical NACA profiles [128]. Blades with such thickness are more structurally efficient. Accordingly, a 25% thick, symmetric NACA airfoil was used with a chord length of 10 cm and an aspect ratio of 2.54. The internal structure of the hydrofoil was left predominantly hollow and sealed water-tight with epoxy. This allowed for reduced hydrofoil mass and about 2.6 N of buoyancy, both of which allowed for the hydrofoil to passively heave at lower flow speeds.

4.3.2 Flow Channel, Turbulence Generator, and Flow Speeds

The UVA water channel testing facility used in this study (Rolling Hills 1520) contains a 1520 mm long, 450 mm tall, and 380 mm wide test section with open channel flow and can reach flow speeds up to 1 m/s. As noted previously, the key objective of this study is to investigate the impact of free stream turbulence (as would be seen in an actual riverine environment) on the hydrodynamic performance of a single semi-passive oscillating hydrofoil. To provide increased turbulence into the water channel flow experimentally, a passive turbulence grid (shown in Figure 4-5) was placed in the water channel upstream of the hydrofoil testing apparatus. This turbulence grid contains six columns and eight rows of vanes that can each be adjusted to a specific angle of attack, allowing users to vary the mean levels of turbulence intensity as well as create turbulent shear flows along the height and/or width of the channel. The square vanes are 1.63 inches in length but are oriented within the turbulence grid such that the diagonal length of the vanes is parallel with streamwise flow when the vane angle of attack is set to 0°. For the flow speeds used in the hydrofoil testing apparatus experiments, the Kolmogorov length and time scales associated with the vane diagonal length is on the order of 1×10^{-4} m and 0.1s respectively. In this study, the angle of attack of the turbulence grid row vanes alternated between $\pm25^{o}$, as shown in Table 4-2, to create nearly uniform turbulence throughout the channel depth. Higher angles of attack were avoided to prevent excessive pressure drops, which could limit the flow capacity provided by the channel pump motor. All vane columns in the generator were aligned parallel to the flow (0° angle of attack) to minimize pressure drop.

Figure 4-5. Passive turbulence grid set to vane angles shown in Table 4-2.

Table 4-2. Passive turbulence grid row vane angles.

Row	Vane angles
1	+25°
2	-25°
3	+25°
4	-25°
5	+25°
6	-25°
7	+25°
8	-25°

The flow speed in the upstream portion of the test section as measured using an ultrasonic flowmeter where the transducers are fixed on the channel wall as shown below in Figure 4-6. During experimental operation, the flowmeter was located upstream of both the hydrofoil and turbulence grid. Due to the open-loop nature of the water channel flow speed control, variations in flow depth and the introduction of objects in the test section induced fluctuations in the flow velocity at the hydrofoil plane.

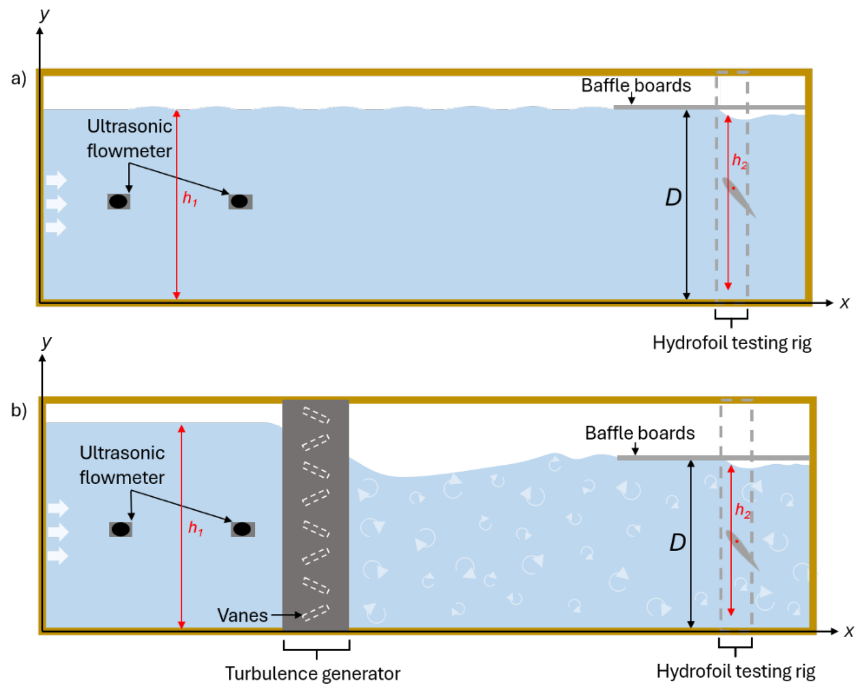

Figure 4-6. Schematic of a) Baseline flow experimental set up and b) generated turbulence flow experimental setup.

The experimental setup for the Baseline flow case without the turbulence grid is shown in Figure 4-7a and the setup for the turbulence grid cases are shown in Figure 4-7b-c. The hydrofoil testing apparatus, turbulence grid, and baffle boards are shown in Figure 4-7c looking upstream toward the hydrofoil.

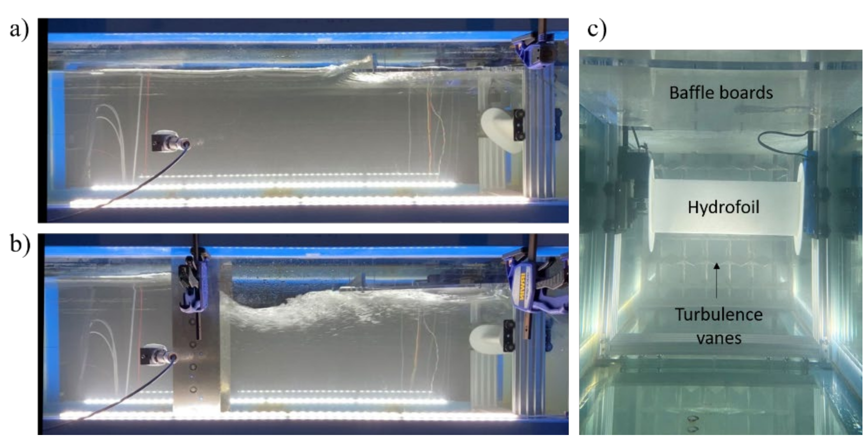

Figure 4-7. Photographs of experimental setup in UVA water channel facility. a) Side view of Baseline flow experiments, b) Side view of generated turbulence flow experiments, c) back view of generated turbulence flow experiments.

The disturbance to the water channel flow that the turbulence grid induces caused a hydraulic jump to occur as the flow passes through it (Figure 4-7b). The ultrasonic flowmeter attached to the water channel side wall allowed for measurements to be taken upstream of the turbulence grid (U_{FM}). However, to accurately estimate hydrodynamic efficiency, undisturbed flow speed measurements at the hydrofoil plane are required. Based on the principle of mass conservation, an indirect method for estimating the flow speed at the hydrofoil plane was considered. The ratio of cross-sectional area at the flow meter relative to the area at the hydrofoil plane was used to estimate the flow speed at the hydrofoil plane (U_{HP}) as shown in Eq. 4.13 where h_1 and h_2 represent the water height at the flowmeter and hydrofoil plane, respectively.

$$U_{HP} = \frac{w_1 h_1}{w_2 h_2} U_{FM} \qquad \text{Eq. 4.13}$$

The depth at the hydrofoil plane excludes the thickness of the hydrofoil testing apparatus's bottom frame. These height dimensions can be seen in Figure 4-6. The width of the channel (w) varies due to the thickness of the side frames.

For each flow speed tested, data were collected once water flow reached its steady state, as determined by the ultrasonic flowmeter. Multiple 30-second data sets were then taken while the hydrofoil was in operation. During the data recording, an average ultrasonic flowmeter reading was taken to use as U_{FM} in Eq. 4.13. Measurements for h_1 and h_2 were also obtained during this period. This process was repeated for both flow conditions. Each set of data contains roughly 33 full heave cycles. To calculate cycle averages of kinematic, force, and power extraction parameters, the dataset was divided into individual heave cycles, which were then each analyzed. The data was then binned based on hydrofoil plane flow speed (U_{HP}) and mean values for the parameters studied were calculated at each U_{HP}. The values for U_{HP} from Eq. 4.13 were subsequently used to access hydrofoil performance using Eqs. 4 – 8.

4.3.3 Water Channel Flow Characterization

Hot-wire anemometry was used in this study to measure streamwise mean velocity profiles and turbulence intensity profiles at the hydrofoil plane. To accomplish this, a hot-wire probe was placed in the water channel at approximately the same streamwise location as where the hydrofoil testing apparatus was placed as defined in Figure 4-6. The flow characterization experiments were performed with and without the turbulence grid for a range of flow speeds, but were all taken with the hydrofoil and its testing rig removed. As such, the flow speed measurements obtained from the hot-wire probe differ somewhat from the flow speeds seen by the hydrofoil in experiments since it does not account for the hydrofoil rig blockage effects due to changes in width (Eq. 4.13). However, the baffle boards are included in the hot-wire measurements.

At the hot-wire location, measurements were taken with at a sampling rate of 1 kHz over various depths from *y/D* = 0.38 – 0.65 where *y* is the local depth of the hot-wire probe and *D* is the depth of the channel below the baffle board at the hydrofoil. Filtering was not applied to the hot-wire data as noise levels were low. To investigate the impact of turbulence on hydrodynamic performance, flow characterization experiments were performed under two different flow conditions: with and without the turbulence grid in the water channel. For each flow condition, hot-wire measurements were taken at multiple flow speeds at each *y/D* location. To eliminate channel system transients within the water channel, the channel was run for approximately 15 minutes prior to taking hot-wire data for each flow speed. Each measurement consisted of 30 seconds of data collection which was translated into a mean flow speed and turbulence intensity using Eq. 4.14, where $u_{HW}{}'$ are streamwise velocity fluctuation about the mean hot-wire flow speed $\overline{U_{HW}}$.

$$\mathrm{TI} = \frac{\sqrt{\overline{(u_{HW}{}')^2}}}{\overline{U_{HW}}} \qquad \text{Eq. 4.14}$$

The results provide characterization of the mean velocity profile and turbulence levels obtained within the water channel under both flow conditions.

4.4 Experimental Results

This section discusses the results from water channel flow characterization and oscillating hydrofoil experiments to assess the impact of elevated turbulence levels on the hydrodynamic performance of a single oscillating hydrofoil.

4.4.1 Hot-wire Anemometry Results

Results from the hot-wire anemometry are shown below in Figure 4-8. The “Baseline flow” data represents measurements taken in the channel without the turbulence grid in place while the “Generated turbulence” data are measurements with the turbulence grid. The maximum heave range achieved throughout all the subsequent oscillating hydrofoil experiments are also shown based on the pitch axis. As desired, the mean velocity profiles in Figure 4-8a confirm fairly uniform flow speeds throughout the relevant depth of the water channel for both Baseline flow (BLF) and Generated turbulence flow (GTF) conditions. The turbulence generator data was obtained at the same set point for the flow meter for each set but was reduced due to the open loop nature of the water channel flow control and the extra drag caused by the turbulence grid generator.

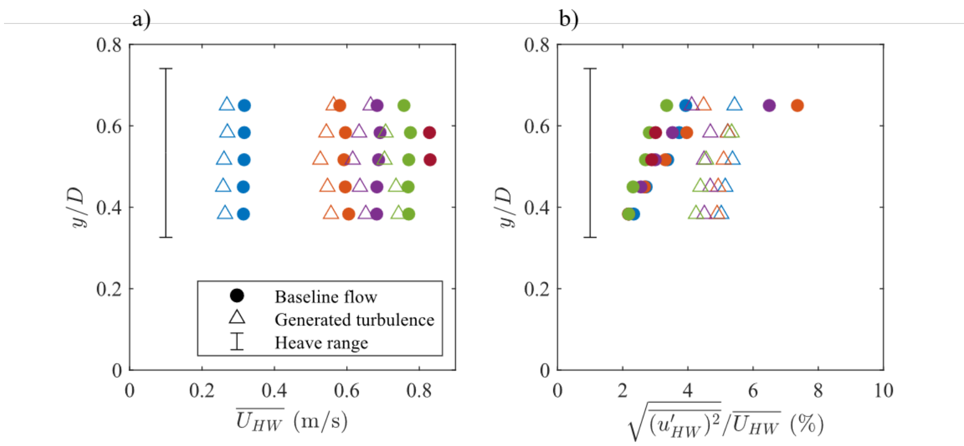

Figure 4-8. Hot-wire anemometry results for a) mean velocity profile and b) turbulence intensity profile. Each marker color represents a specific water channel pump pressure tested.

The corresponding turbulence intensity profiles are shown in Figure 4-8b. The Generated turbulence flow (GTF) has higher mean turbulence intensity levels than that of the Baseline flow (BLF) for the *y/D* values below 0.6 for all flow speeds. In general, the turbulence intensity levels for GTF case also remain relatively consistent within the hydrofoil heaving range and with increasing flow speeds at an average of 4.82% and ranging from 4.5% – 5.2%. The BLF turbulence intensities are generally lower, as would be expected, but indicate a clear increase with *y/D* > 0.6 that is not observed in GTF. Furthermore, for the data at the mean flow speed of 0.6 m/s and 0.68 m/s, the turbulence intensity for BLF exceeds that of GTF at *y/D* = 0.65. This increase is attributed to free surface unsteadiness caused by the baffle boards used in this study. While the baffle boards are used to mitigate free surface effects on an average sense, there are addition interactions between the baffle board and waves that influence the water channel flow for BLF. In particular, video observations at the higher water channel flow speeds showed that the free surface becomes increasingly deformed and unsteady, exciting the baffle boards and periodically causing a thin layer of water (relative to the channel depth) to flow over top of the upstream board.

These unsteady free surface-baffle board interactions result in momentary dips in the flow speed below the boards, where the hot-wire anemometry is performed. This effect can be observed as dips in the hot-wire data as shown in Figure 4-9, where streamwise velocity fluctuations at a flow speed of 0.69 m/s (purple circles in Figure 4-8) are shown at two different *y/D* values for BLF. The data at *y/D* = 0.65 corresponds to a turbulence intensity of 6.5% while the data at *y/D* = 0.58 yields a turbulence intensity of 3.5%. This also results in mean flow speeds at *y/D* = 0.65 which are slightly lower than at lower *y/D* values. As such, the results for BLF should be considered to be low turbulence for only most of the heave range. Fortunately, the GTF case was not significantly impacted by flow unsteadiness associated with the baffleboard.

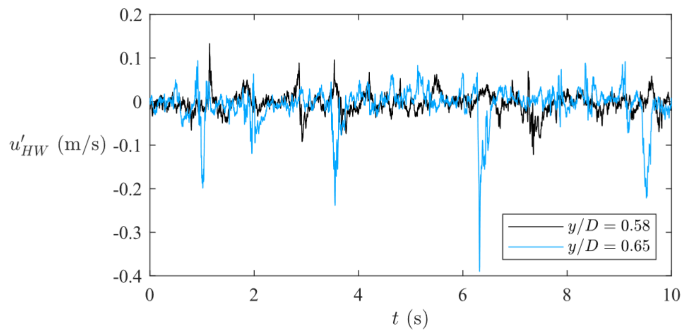

Figure 4-9. Hot-wire streamwise velocity fluctuations at a mean hydrofoil plane flow speed of 0.69 m/s at 0.65 and 0.58 of total depth under the baffle boards for the Baseline flow.

4.4.2 Hydrofoil Kinematics and Forces

The resulting kinematics of a semi-passive hydrofoil system are explored in this section. Figure 4-10 shows heave (referenced at the pitch axis) and angle of attack kinematics as well as the corresponding vertical force coefficients and heave-based power coefficients for both flow conditions at three different hydrofoil plane flow speeds (U_{HP}). The horizontal axis spans one full heave period (T) and is shown using normalized time t/T. The beginning of a period ($t/T = 0$) is defined at the bottom of the heave range as the hydrofoil begins to heave upwards, and the ending ($t/T = 1$) occurs when the hydrofoil returns to the back to the bottom. The signals shown in Figure 4-10 represent the average path of each parameter over approximately 33 consecutive periods. A simple moving average filter is used on each average path for the purposes of presentation to highlight the larger features that occur over an average period.

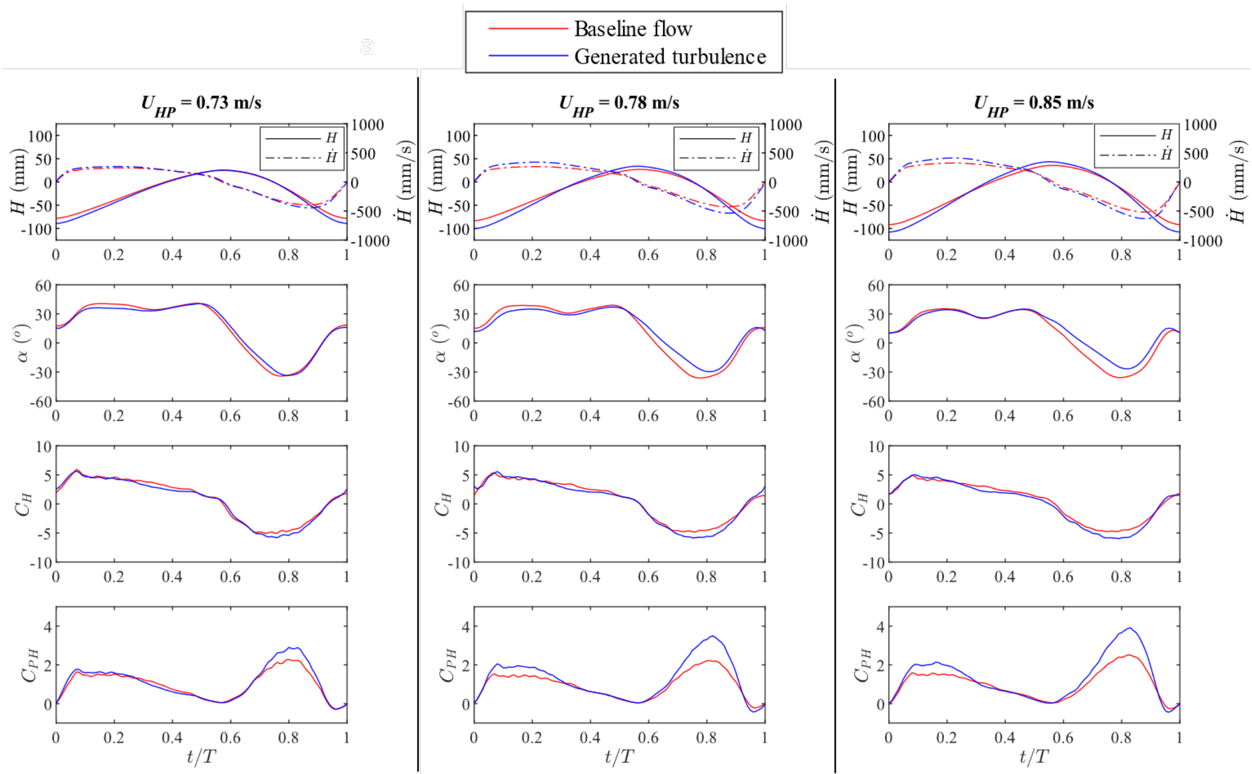

Figure 4-10. Experimental data for a single period showing heave kinematics (based on the pitch axis), angle of attack, vertical force coefficient, and heave-based mechanical power coefficient for various hydrofoil plane flow speeds.

In all cases, the heaving oscillations are periodic but not symmetric about both the target zero heave location (H = 0) and t/T = 0.5. Due to gravity and the inertia of the hydrofoil, the passive heave motion results in a faster and longer downstroke. Buoyancy due to the hollow structure of the hydrofoil reduces some of the vertical asymmetry in the heave motion, but additional measures could be considered later to further improve symmetry. The maximum positive heave was reached consistently between t/T = 0.55 – 0.57. In general, GTF and BLF have the same qualitative variations in time and the quantitative differences are mostly minor. However, GTF increases the heave range of the hydrofoil across all flow speeds, as much as 14% at U_{HP} = 0.85 m/s, when compared to BLF. This is attributed to higher downward vertical hydrodynamic forces that control the extent of the lower heave range which is consistent with larger negative vertical force coefficients (C_H) for GTF seen at t/T = 0.8.

The heave velocities are calculated via central finite differencing using the heave encoder data and are also shown in Figure 4-10. While the qualitative features are again similar, maximum heave velocities on the upstroke occur slightly earlier in GTF on average over all U_{HP} at t/T = 0.21 compared to t/T = 0.25 in BLF. The peak downstroke heave velocities occur at t/T = 0.87 on average in both flow conditions and are higher in magnitude than peak upstroke heave velocities due to the benefit of gravity. At comparable values of U_{HP}, GTF resulted in higher peak heave velocity magnitudes over a full heave period. Such differences are again attributed to higher downward vertical hydrodynamic forces.

The angle of attack (α) variations over one period is shown in Figure 4-10 where a positive angle of attack follows the same sign convention as an upward pitched hydrofoil ($\theta > 0$). Again, the variations are also asymmetric about $t/T = 0.5$ where the slower and shorter upstroke results in an oscillating positive angle of attack followed by a single fall to a negative angle of attack. In both cases, at the end of the upstroke, the hydrofoil begins to pitch down and the resulting drop in lift initiates the beginning of the downstroke. Thus, there is fairly good synchronization between pitch and heave and the drop in angle of attack just prior to the maximum heave in terms of t/T. However, on the downstroke, due to gravity and the inertia of the hydrofoil, the hydrofoil ends its downward heave motion later than when pitch actuation occurs relative to the upstroke. Slight fluctuations in the angle of attack attributed to backlash in the pitch servo motor are observed during the heave upstroke between $t/T = 0.2 – 0.4$. This aspect, along with the impact of gravity and inertia on the synchronization of hydrofoil kinematics should be considered in the design of full scale semi-passive oscillating hydrofoil devices.

Comparing the GTF and BLF in terms of angle of attack, the maximum positive angle of attack was similarly about 41° on average for both cases. However, GTF yielded a decreased maximum negative attack angle with increasing flow speed up to $U_{HP} = 0.85$ m/s where the maximum negative attack angle is only -32° for GTF compared to -38° for the BLF. This indicates that the increased downward hydrodynamic force for the GTF case may be due to improved hydrodynamics rather than larger angle of attacks. This suggests increased hydrodynamic robustness of the GTF case in terms of the LEVS, which should be explored further.

Vertical force coefficients (C_H) are also presented in Figure 4-10 as calculated by Eq. 4.7. On the upstroke, the magnitudes of the vertical force coefficients do not differ significantly under the two flow conditions at similar U_{HP}. The peak vertical forces occur shortly after the hydrofoil begins to change heave directions in both strokes which correspond to an angle of attack between 21° – 26°. After peak vertical force coefficients are reached, the decaying vertical forces cannot continue to overcome gravitational forces and friction in the system and the hydrofoil slows until $\dot{H} = 0$ where the angle of attack and C_H becomes negative. Subsequently, there is a rapid drop in C_H as it becomes negative. This rapid drop in C_H can be attributed to the kinematic asymmetry stemming from the gravitational force.

It is interesting that the minimum distance observed between the hydrofoil pitch axis and baffle boards is approximately one chord length. This may provide a confinement benefit. However, it is unclear if there is any benefit from LEVS present in at the end of upstroke based on the force dynamics despite the good synchronization of pitch and heave. There does not appear to be any indication of LEVS on the downstroke from the C_H curves due to the poor synchronization of the pitch and the heave, although larger peak C_H magnitudes are achieved for the downstroke than the upstroke, especially at higher flow speeds. Further investigation using fluid imaging techniques such as Particle Image Velocimetry are necessary to confirm the impact of dynamic stall and/or flow confinement effects in this experiment.

Heave based power coefficients (C_{PH}) are calculated using Eq. 4.8. Over one period, C_{PH} appears to be mostly positive, indicating good synchronization between heave velocity and vertical force overall. The only region where C_{PH} becomes slightly negative is at the end of a period beyond $t/T \sim 0.93$ due to the larger offset in t/T between pitch actuation and the minimum heave location, as mentioned previously. When comparing the upstroke and downstroke, higher peak C_{PH} values are clearly observed during the downstroke. Despite the relatively poor synchrony between pitch and heave at the end of the downstroke, the higher heave speed and slightly larger vertical force magnitudes result in greater maximum C_{PH}. Evaluating the mean C_{PH} over the upstroke and downstroke of the heave motion separately shows that the downstroke produces more power than the upstroke by 16% in BLF and by nearly 40% in GTF across all flow speeds. This illustrates that a semi-passive oscillating hydrofoil turbine can still produce significant power under less-than-ideal pitch and heave synchronization. Returning to the comparison of the two flow conditions, both BLF and GTF produced relatively similar average C_{PH} values on the upstroke (slightly higher for GTF), but varied significantly on the downstroke, with GTF producing approximately 23% higher average downstroke C_{PH}. Over an entire period ($t/T = 0 - 1$), GTF results in a 12% higher average C_{PH} than BLF across the tested flow speeds, primarily attributed to the higher peak C_{PH} reached during the downstroke.

Mean kinematic parameters are shown in Figure 4-11 and Figure 4-12 for all of the experimental data obtained, binned by hydrofoil plane flow speed (U_{HP}). Due to the blockage from the turbulence grid, the U_{HP} values achieved for GTF were limited to 0.85 m/s while BLF speeds exceeded 0.9 m/s. However, experiments for both flows were obtained for a significant range of overlapping U_{HP} to allow direct comparison.

Figure 4-11a shows the Strouhal number (St) as calculated by Eq. 4.12. Recall that the pitch control system was based on heave position only, so the oscillating frequency was not prescribed but rather was an output of the forces and kinematics. There is little variation in St with U_{HP} under both flow conditions with the mean St across U_{HP} tested for both flow conditions of about 0.25, indicating the system frequency (f) tends to increase linearly with flow speed (U_{HP}). For the heave amplitudes seen in Figure 4-11b, d^* is consistently between 14 – 17% greater than H^* for both flow conditions due to the constant pitch axis location (c/3) and similar synchronization of pitch and heave, and both increase significantly with increases in flow speed. In particular, d^* for BLF increases by about 19% for a 32% increase in flow speed. Since the chord length is fixed and the Strouhal number is nearly constant and given by St = fd^*c/U_{HP}, this indicates that frequency (f) increases by about 9% over the same range. This weaker change in frequency may be attributed to the system inertia and stiffness providing a natural frequency that is approximately independent of flow speed and which tends to limit the driving frequency. In addition, GTF results in larger heave ranges and higher d^* than BLF, especially at higher U_{HP} (as discussed previously). In particular, the difference St, d^* or H^* between the two flow conditions is only a few percent for $U_{HP} \leq 0.8$ m/s but increases up to 14% at $U_{HP} = 0.85$ m/s where St = 0.27 for GTF. This difference is consistent with the results seen in Figure 4-10.

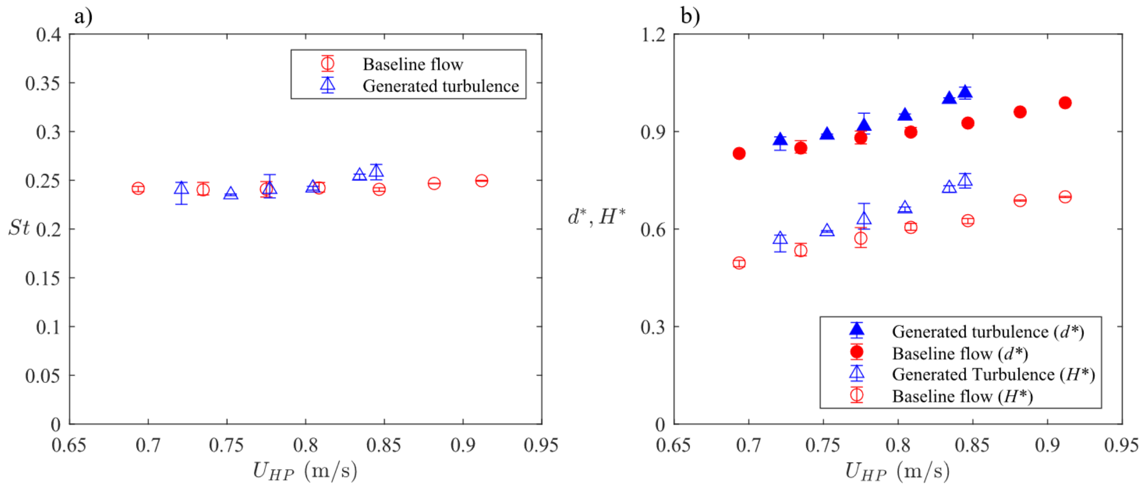

Figure 4-11. a) Strouhal number and b) trailing-edge distance-to-chord and heave-to-chord over hydrofoil plane flow speeds.

The heave velocities for the two flow conditions are illustrated in Figure 4-12a. Both flow conditions exhibit more than a 50% higher average peak heave speed during the downstroke compared to the upstroke, with increases up to 61% in BLF and 77% in GTF at $U_{HP} = 0.85$ m/s. On the upstroke, the peak upstroke heave speeds under GTF are only marginally higher than in BLF up to $U_{HP} = 0.8$. Beyond this, the difference grows to approximately 20% at $U_{HP} = 0.85$. Downstroke peak heave speeds vary more, approximately 11% – 18% greater on average for GTF than for BLF. As presented with C_{PH}, these higher downstroke velocities contribute to higher average heave-based power in the GTF cases over a full period.

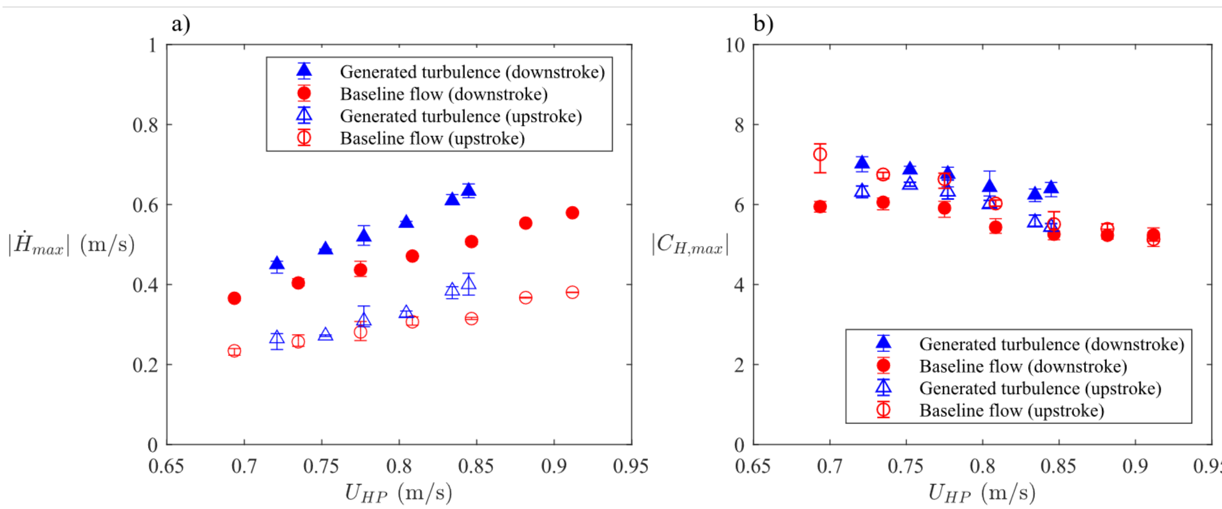

Figure 4-12. a) Average peak heave speeds and b) average peak vertical force coefficients for heave upstroke and downstroke across hydrofoil plane flow speeds.

The peak vertical force coefficients ($C_{H,\max}$) are shown for each flow condition in Figure 4-12b. Specifically for GTF, the downstroke produced higher $C_{H,\max}$ than the upstroke at all U_{HP}. However, the opposite is observed under BLF for $U_{HP} < 0.85$ m/s where the upstroke produces a $C_{H,\max}$ up to 22% greater than that during the downstroke at the slowest U_{HP} tested. As U_{HP} increases, $C_{H,\max}$ on the upstroke and downstroke converge to similar values for BLF. Overall, there appears to be a slight decrease in $C_{H,\max}$ for U_{HP} above approximately 0.75 m/s under both flow conditions. On the downstroke, GTF consistently shows higher $C_{H,\max}$ compared to BLF from 14% – 22% with the largest difference occurring at $U_{HP} = 0.85$ m/s. However, $C_{H,\max}$ values are fairly similar between the two flow conditions on the upstroke. The higher peak C_{PH} observed on the upstroke under GTF in Figure 4-10 is thus a result of the higher heave velocities as shown in Figure 4-12a as opposed to larger peak vertical forces.

4.4.3 Power and Hydrodynamic Efficiency

The experimental data was used to estimate total power (P_{tot}) and hydrodynamic efficiency (η_{hydro}). As shown in Figure 4-13, the cycle-averaged total mechanical power (P_{tot}) is calculated using Eq. 4.4 and Eq. 4.5 and assumes a 20% loss from pitch actuation ($p_{\text{loss}} = 0.2$). The mean mechanical power solely from heave (P_H) is also plotted. The cycle-averaged power extracted in GTF is higher than that of BLF across all flow speeds. The difference between the two flow conditions grows as U_{HP} increases up to 34% at $U_{HP} = 0.85$ m/s. While the narrow range of flow speeds achieved in the water channel makes the data appear linear, cycle-averaged power is expected to increase proportionally to U_{HP}^3. This significant increase in cycle-averaged power is promising for real-world operation of oscillating hydrofoil systems where riverine flows have high turbulence and even higher flow speeds than those tested in this study [10, 26]. However, it should be considered that in these experiments, larger heave ranges for the GTF case bring the hydrofoil closer to the baffle boards and channel floor where flow confinement effects are expected to occur. These confinement effects could explain part of the power enhancement for cycle-averaged power between the two flow conditions. This enhancement highlights another potential opportunity to further increase power capture whereby the proximity of the hydrofoil to the free surface in a river can provide a similar effect, when the free surface is nearly level.

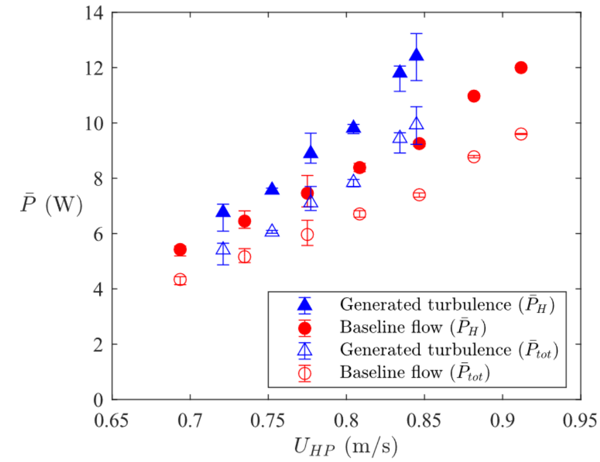

Figure 4-13. Cycle-averaged mechanical power for both flow conditions across tested flow speeds for heave-power (P_H) and total power (P_{tot}).

Finally hydrodynamic efficiency (η_{hydro}) is presented in Figure 4-14, with values based on $p_{loss} = 0.2$ (corresponding to P_{tot}) and $p_{loss} = 0$ (corresponding to P_H, which does not include losses to pitching power). Once again, the hydrofoil performs better in GTF. Over the range of flow speeds tested, GTF efficiencies are enhanced by about 5% – 12% over that of BLF at comparable U_{HP}. The average η_{hydro} value with pitch losses included is higher than that of BLF across all flow speeds and appears to remain fairly consistent, ranging from 50% to 52% as flow speed increases. However, there is a clear decrease in efficiency with U_{HP} in BLF. The average efficiency drops 5% over just a 0.2 m/s increase in flow speed for $p_{loss} = 0.2$.

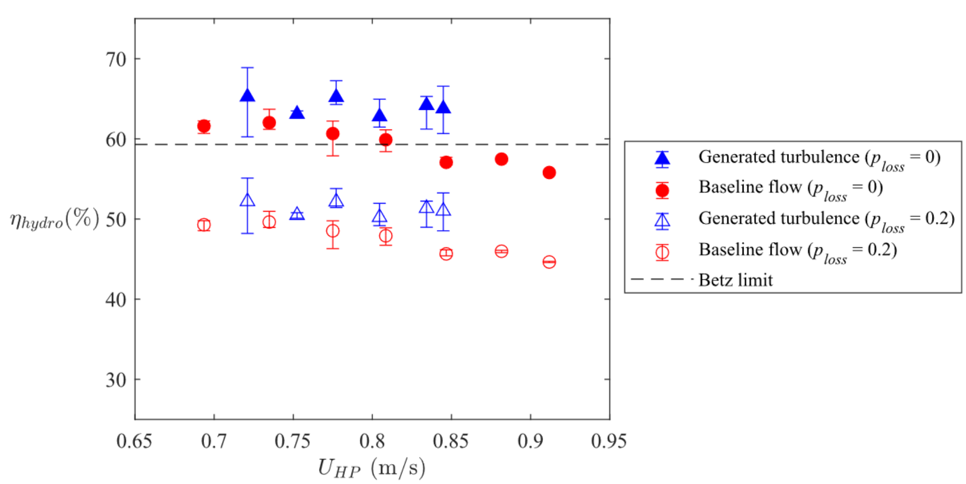

Figure 4-14. Hydrodynamic efficiencies for both flow conditions plotted against hydrofoil plane flow speed assuming 0% and 20% losses due to pitch actuation.

Power extraction efficiency solely from heave based mechanical power without pitch actuation losses ($p_{loss} = 0$) surpasses the Betz limit for all Generated turbulence flow speeds and most Baseline flow speeds. Yet the efficiency based on true power extracted is always less than the Betz limit. The relatively high values of 50% or more indicates that there may be some benefits of flow confinement and future work should consider this aspect in more detail. However, confinement levels for a single wall with an oscillating hydrofoil that has a minimum gap of one chord length (similar to that found in this study) have been found in experiments to be relatively small (about 1% improvement) [22]. Additionally, the greater peaks in vertical force observed in Generated turbulence flow occur before the hydrofoil reaches the extremes of the heave ranges where confinement levels are greater than one chord length. Therefore, most of the benefits in cycle-averaged power extraction and hydrodynamic efficiency are attributed to the higher turbulence levels.

4.5 Conclusions

Oscillating hydrofoil turbines show strong potential for use in riverine environments where limited depth and flow speeds make it more challenging to implement conventional rotary hydrokinetic turbines. This study aims to be the first to understand the impact that free stream turbulence has on the performance of a semi-passive oscillating hydrofoil turbine. In doing so, an experimental hydrofoil testing apparatus was designed and built to measure hydrofoil forces and kinematics. Damping related to converting mechanical to electrical power was added through the small-scale power takeoff system. Experiments were performed in the water channel under various flow speeds with and without the presence of a passive turbulence grid, which was used to increase turbulence intensity in the channel flow.

Hot-wire anemometry confirmed uniform mean streamwise velocity profiles under both flow conditions throughout the range of water channel flow speeds measured. Slight decreases in mean flow speed were observed at higher y/D due to interactions between the baffle board and free surface. The turbulence grid configuration used produced fairly uniform turbulence intensity profiles around 5% at all flow speeds. The Baseline flow with lower turbulence levels appears to increase in turbulence intensity with y/D, likely due to these baffle board-free surface interactions.

From the oscillating hydrofoil experiments, the Generated turbulence flow consistently resulted in improved performance both in terms of kinematics (peak heave velocities magnitudes and higher heave-to-chord ratios), forces, and power extraction. For the two flow conditions tested, both showed similar asymmetric heave and pitch motions due to gravity and the inertia of the hydrofoil. The downstroke motion consistently produced higher peak and average heave-based power coefficients than the upstroke at all speeds. Strouhal numbers did not vary significantly with flow speed or flow condition. Slight increases in frequency correspond with significant increases in heave-to-chord ratios which in turn leads to more power generation. Increased turbulence intensity levels in the flow may reduce flow separation around the hydrofoil during periods where pitch is held constant, resulting in greater vertical forces and heave velocities that contribute to increased power generation. However, the influence of Leading-Edge Vortex

Shedding is not clearly observable using the experimental methodology presented and requires further investigation. Total mechanical power is estimated assuming a 20% loss from pitch actuation per cycle (based on separate results provided from Lehigh University) and again showed better power generation in higher turbulence levels, especially as flow speeds increased. Lastly, there is a slight decrease in hydrodynamic efficiency with flow speed in the Baseline flow condition that is not apparent under the Generated turbulence flow. However, hydrodynamic efficiencies vary more from cycle to cycle in Generated turbulence flow due to the increased freestream unsteadiness. The maximum efficiency observed was under Generated turbulence flow, at about 52%. Confinement effects are also likely involved in the high efficiencies observed in this study, but are expected to be secondary to the effects of turbulence.

This study leads to many recommendations for future work. First, real-world riverine environments may have even higher levels of turbulence than what was used in this study in which performance may be improved even more. Water channel turbulence characterization may additionally be achieved using fluid imaging techniques like Particle Image Velocimetry (PIV) that may allow for more accurate estimates of streamwise flow velocities, which influence hydrodynamic efficiency values, by taking measurements simultaneously with the hydrofoil testing apparatus experiments. Increasing the turbine size can also provide benefits as the Reynolds number is increased to regimes more relevant to riverine conditions. Future studies could incorporate fluid imaging methods to further explore the fluid dynamics of semi-passive oscillating hydrofoils in turbulent flows and confinement effects. In addition, differences in LEVS and hydrofoil flow separation between flow conditions may be studied both experimentally and computationally with inflow turbulence to determine the fluid physics behind the observed efficiency benefits. Total power and hydrodynamic efficiency measurements can be made more accurate by directly measuring pitching power consumption, e.g., by measuring electrical current from the pitch servo system. Confinement effects from the baffle boards and channel side walls should also be further explored. Due to the limited dimensions of the water channel, numerical simulations using direct Navier-Stokes flow solvers may be better suited for such work. Although baffle boards were implemented to mitigate free surface effects, real riverine flow conditions will not only have higher levels of turbulence, but also a velocity profile and free surface effects. Both can be incorporated into the current setup by removing baffle boards and adjusting the turbulence grid vane angles to further assess oscillating hydrofoil turbines performance in more realistic riverine flow conditions. Lastly, while maximizing hydrofoil mechanical efficiency through fluid-structure interactions is crucial, the conversion from mechanical to electrical power is just as important. The conversion of mechanical to electrical power can be studied using the small-scale Power Take-Off (PTO) system on the testing apparatus used in this study. Adjusting the resistance connected to the output of the back driven brushless DC motor will have direct consequences on hydrofoil kinematics, and should be optimized to determine ideal resistance values needed.

Chapter 5

Confinement Benefits with Dual Oscillating Hydrofoils at Field Scale Reynolds Numbers

Abstract

In order to understand the flow dynamics and potential energy harvesting performance of a vertically-stacked dual hydrofoil system in a full-scale riverine environment, simulations were conducted to compare single vs. dual hydrofoils, compare low lab-scale Reynolds numbers (10,000) vs. full-scale field Reynolds numbers (378,000), and to compare unbounded vs. various types of vertical confinement conditions. The two-dimensional Navier-Stokes numerical approach was validated with lab-scale experimental results and the predictions were shown to capture the highly unsteady dynamics of the lift forces and pitching moments. Predicted hydrodynamic efficiencies were reasonable compared to three-dimensional lab-scale experiments in terms of the influence of nominal pitch angle and Strouhal number, though some small differences were found, which can be primary attributed to finite aspect ratio effects. Using this computational approach, conditions at full-scale Reynolds numbers were considered and it was found that there are two main vertical confinement effects: confinement due to hydrofoils dynamically approaching each other and confinement due to a level free surface above confined with a level riverbed below. The latter confinement was much more pronounced and led to hydrodynamic efficiencies (based on true swept area) as high as 80%, which are significantly above the Betz-limit of 59%, and perhaps the highest yet reported. These results indicate that confinement due to hydrofoil proximity to the free surface and/or riverbed can be utilized to significantly improve energy harvesting performance. However, effects of three-dimensionality, inflow turbulence, velocity shear and non-planar variations in the free surface and riverbed should be considered in future research.

5.1 Introduction

The increasing focus on renewable energy coupled with environmental limits on hydropower, have placed an increased emphasis on hydrokinetic energy extraction from rivers and flows with currents. Riverine environments are typically shallow (with depths typically less than 5% of their widths) and have seasonal variations in local depths, which introduce unique challenges to deploy renewable energy devices in [10]. To account for this geometry, horizontal oscillating hydrofoils are of increasing of interest [103] since these systems have swept areas that can more readily adjust to changes in river depth [12] and have lower tip speeds (compared to rotary turbines) which allows them to be more environmentally friendly to aquatic animals.

Oscillating hydrofoil turbines are characterized by a chord length (c), a spanwise length (s) and employ a combination of periodic pitching and heaving (vertical displacement) hydrofoil motions to generate power via the concept of unsteady lift [106]. Instead of a steady attached flow as is typical for rotary turbines, oscillating hydrofoils have a continuous flow separation and a shedding flow cycle controlled by Leading-Edge Vortex Shedding (LEVS) that can provide improved hydrodynamic efficiency [12]. Locating the pitch center at a location $c/3$ downstream of the leading edge has been shown to increase hydrodynamic efficiency as compared to the conventional $c/4$ location used for rotary systems [14]. For an upstroke of a hydrofoil, a positive pitch angle is used to create a positive angle of attack to provide a lifting force and upward velocity of the hydrofoil. For the ensuing downstroke, the pitch angle is reversed to produce a negative angle of attack for a downward force and velocity. Thus, in both directions, the combination of force and velocity provides a positive mechanical power that can be extracted from the flow and converted to electrical energy [14, 113]. In an actual harvesting system, the synchronization of vertical force and heave velocity for larger portions of the cycle can be achieved with sufficiently large pitch angles and a controlled pitch motion. This allows for the heave degree of freedom to be passive with a controlled or passive pitch motion [113, 117, 129]. The pitch is often set to vary smoothly using a sinusoidal function in order to reduce peak loads and load fluctuations on the hydrofoil.

Full-scale riverine conditions are expected to include chord lengths of 30 cm and flow speeds of around 1 – 2 m/s, corresponding to Reynolds numbers of about 300,000 – 600,000, and with significant vertical confinement aspects. However, most work has focused on single hydrofoils and/or hydrofoils in unbounded domains and mostly at low Reynolds numbers [14, 130, 131]. Such previous work has investigated parametric spaces associated with varying hydrofoil pitch through the nominal pitch angle (θ_0), heave frequency through the Strouhal number (St). A two-dimensional numerical study by Kinsey and Dumas at Re = 1100 have found optimal hydrodynamic efficiencies to occur for θ_0 between 70° – 80° and for St between about 0.3 – 0.45 [14]. This study by Kinsey and Dumas focused on a single hydrofoil with a computational domain extending in excess of 70 chord lengths in both streamwise and heave directions, so that the flow was effectively unbounded. A similar unbounded study at Re = 500,000 showed that optimum θ_0 and St points for a single unbounded hydrofoil are both slightly higher than at Re = 1100 with larger heave-to-chord ratios (H_0/c) resulting in increased optimal θ_0 and lower optimal St [124]. Extensive experimental work for a single hydrofoil was carried out by Simpson at Re = 13,800 to study similar parametric spaces experimentally and the results showed similar trends in Strouhal numbers and nominal pitch angle [15]. Flow visualization, either from numerical simulations or Particle Image Velocimetry (PIV) techniques were employed in these previous studies [14, 15, 124] to better understand the role of Leading-Edge Vortex Shedding (LEVS) on hydrofoil performance. Results indicate that LEVS can boost hydrodynamic efficiency, though high efficiencies ($\eta_{\text{hydro}} > 30\%$) can still be achieved without LEVS [13].

In practice, multiple hydrofoils can be implemented in a riverine flow to generate even more electricity. Tandem dual hydrofoils have been considered where one hydrofoil is placed downstream of another and operates in a phase shift of 180° with the upstream hydrofoil [132]. Results from two-dimensional numerical simulations indicate that with appropriate horizontal spacing between the hydrofoils, the downstream foil may produce extremely high efficiencies ($\eta_{\text{hydro}} > 50\%$), potentially even surpassing the Betz limit, due to interactions with the wake vortex structures coming from the upstream hydrofoil [132, 133].

However, for actual riverine conditions, vertically stacked dual hydrofoils can be beneficial since they can balance out the net forces on the system and since they can be designed to take advantage of the confinement effects associated with shallow flows. Therefore, there is significant interest in considering dual hydrofoils operating in vertically confined conditions. A turbine in confinement can increase the power extraction (compared to that in an unbounded domain) because the velocities are accelerated around surfaces. Notably, vertical confinement for dual-oscillating hydrofoils can arise from three different sources:

1) Confinement due to the solid surface riverbed below the hydrofoils
2) Confinement due to the free surface above the hydrofoils, especially if this surface stays nearly level
3) Confinement between hydrofoil surfaces, especially if they become close to each other

The last type of confinement is specific to conditions with multiple vertically spaced foils which are mirrored so that the upper hydrofoil is lowest when the lower hydrofoil is highest. In such cases where the pitch centers are in the upstream portion of the hydrofoil (in front of $c/2$), the smallest gap between two foils tends to occur between the two trailing edges.

There have only been a few studies that have directly looked at the various confinement effects. Theoretically, Garrett and Cummins [134] examined confinement for a rotary turbine using one-dimensional mass and momentum conservation and compared these to the Betz limit for an unconfined turbine, which has a maximum efficiency of 16/27=59.3%. They found that confinement increases the maximum efficiency by a factor of $(1-A/A_c)^{-2}$, where A is the swept area of the turbine, A_c is the cross-sectional area of the channel, and A/A_c is defined as the blockage ratio. Notably, this approach predicts non-physical efficiencies greater than 100% for blockage ratios that exceed 23%.

There have also been experiments and simulations that considered blockage for oscillating hydrofoils. A converging duct was considered for tandem hydrofoils numerically at Re = 100,000 where it was found that hydrodynamic efficiency increased by 27% for a downstream hydrofoil heaving up to one chord length away from the duct walls (measured from the pitch center) [23]. Experimentally, one-wall and two-wall confinements were compared to unconfined conditions in a water channel at Re = 50,000 and a nominal pitch angle of 75° with various St values [22]. The results for the unconfined system yielded an efficiency of 24%. While one-wall confinement resulted in limited improvements in efficiency regardless of the gap between the hydrofoil, two-wall confinement significant enhancement with efficiency increasing from about 24% for an unconfined condition to 50% for a dual confinement with a blockage of 35%. This relative increases is approximately consistent with that predicted by the ratio of $(1-A/A_c)^{-2}$. These efficiency improvements indicate significant potential for riverbed and free surface confinement, but it is not clear if such performance increases can be expected at field-scale Reynolds numbers (which are about 10 to 100 times higher) and when using high nominal pitch angles (which produce higher baseline hydrodynamic efficiencies). Another study by LeFrancois as investigated the third type of confinement from two flat plates interacting at a close vertical distance at a low Reynolds number of 1100 [135]. The plates did not approach each other as mirror images along a horizontal plane and the gap between plates was on the order of the chord length, so the net confinement effect was weak. It is unclear whether a significant confinement benefit would exist if the geometries were modified to hydrofoils, if the hydrofoils acted as mirror images (symmetric movement), if the trailing edge became much closer (a small fraction of a chord length), and if the Reynolds numbers were closer to that of full-scale conditions. Perhaps the study that is most relevant to the present work was conducted by Gauthier et al. which examined confinement effects for a single hydrofoil at a tidal field-scale Reynolds number of 3×10^6 [136]. Given this high value, the flow over the hydrofoil can be expected to be turbulent and thus a Reynolds-Averaged Navier Stokes (RANS) with a Spalart-Allmaras turbulence model was used for this study. The test conditions used a NACA0025 hydrofoil pitching at a location of 0.4c from the leading edge with a nominal pitch angle of 80°, Strouhal numbers from 0.08 to 0.22 and a $H_0/c = 1$, where H_0 is the maximum heave excursion of the pitch center relative to the average pitch center location. They then focused on blockage ratios ranging from 0.2% to 50%, where A was based on the hydrofoil area swept by the pitch center, i.e. A_{pc}. The results indicated that confinement greatly increased the hydrodynamic efficiency based on A_{pc} with maximum values approaching 80% for Strouhal numbers ranging from 0.1 to 0.2. Notably, if one employs the more commonly used hydrofoil area swept by the trailing edge, i.e. A_{TE}, these maximum hydrodynamic efficiencies are reduced to about 63% (surpassing the Betz limit) and the blockage ratios are increased to about 64%. However, the hydrofoil aspect ratio of 6 used in these experiments likely limited these efficiencies. Motivated by the above studies, especially Gauthier et al., the present study sought to investigate the following set of test conditions:

- Laminar flow at Reynolds number of 378,000 in order to better align with riverine field-scale conditions (instead of tidal field-scale conditions) and to avoid the empiricism of RANS turbulence modeling
- Two-dimensional flow (infinite aspect ratio) in order to better understand basic fluid physics and to characterize the maximum efficiency possible with a very high aspect ratios (and potential top end plates) that may be expected for energy harvesting in riverine conditions
- A pitch center located at $c/3$ from the leading edge and a NACA0015 hydrofoil since these conditions were found to produce high hydrodynamic efficiencies for laminar flow conditions.
- Investigate higher nominal pitch angles (up to 90º) and Strouhal numbers (up to 0.6), since these can further increase hydrodynamic efficiency
- Investigate higher blockage ratios, as high as 61% based on A_{TE} since these can further increase hydrodynamic efficiency and may be realistic for riverine-sited oscillating hydrofoils
- Investigate the potential local confinement effects when using two vertically-stacked hydrofoils with mirrored dynamics (90º of out of phase) since these can allow the trailing edges to become very close and since this arraignment can allow a more balanced net force on the combined system (at any given time upward heave forces for one foil would be balanced by downward heave forces for the other foil)

As such, this study seeks to investigate conditions that are specific to a riverine and which may allow the highest possible hydrodynamic efficiencies.

Based on the above, the present study seeks to computationally investigate the two-dimensional fluid dynamics of single vs. dual hydrofoils operating in free vs. confined conditions at field-scale Reynolds numbers. A finite volume-based code was used to simulate hydrofoil pitching and heaving motions in steady flow at Re = 378,000. To validate the Navier-Stokes numerical approach, simulations were compared to experimental results at Re = 10,000 to ensure consistent lift forces, pitching moments, and hydrodynamic efficiency. Time and grid dependence studies were also performed at both laboratory experiment and field scales. Once single hydrofoil simulations with moderate confinement were validated, dual hydrofoil simulations were considered. This is the first study to investigate a vertically-stacked dual hydrofoil configuration to explore potential advantages of flow confinement between the foils with symmetric (mirrored) movement for energy harvesting and to allow for a more force-balanced system. Additionally, also the first study to use measured flow characteristics of a potential field site river to scale up Navier-Stokes simulations (without any turbulence modeling). The field scale simulations were based on flow data from a site in the Kvichak River located in Alaska [26]. Furthermore, this is the first study to address confinement benefits within the scope of real-world flow limitations associated with shallow riverine depths and presents a dual-foil configuration that can take advantage of confinement in multiple ways (through interactions with the flow free surface and with other hydrofoils). Herein, the efficiency and blockage will be based on the true swept area instead of the nominal swept area.

The following describes the hydrofoil motion and performance characterization (Section 5.2), the computational methods and experimental validation (Section 5.3), the dual oscillating hydrofoil simulation approach (Section 5.4), dual hydrofoil results (Section 5.5) and finally conclusions with recommendations (Section 5.6).

5.2 Oscillating Hydrofoil Kinematics

5.2.1 Equations of Motion

The periodic motion of a single oscillating hydrofoil can be defined as a combination of a vertical displacement (heave) and pitch degree of freedom. In an experimental system with driven pitching, the pitch motion is prescribed so the heave motion becomes a consequence of the hydrodynamic forces, the PTO system forces, and the inertia of the coupled moving system. For high efficiency, the resultant heave motion is approximately sinusoidal [17, 115]. To avoid the complexity associated with computing a resultant heave motion and to provide a more generalizable solution (not specific to a single inertia and PTO), herein the both heave and pitch motions are fully prescribed and sinusoidal. A prescribed heave motion also allowed direct comparison with experiments (as discussed in Section 5.3.2). The equations of motion for both heave (H) and pitch (θ) are given below as a function of time (t) as,

$$H(t) = H_0 \sin\,(\omega t + \varphi_2) \qquad \text{Eq. 5.1}$$

$$\theta(t) = \theta_0 \sin\,(\omega t + \varphi_1 + \varphi_2) \qquad \text{Eq. 5.2}$$

The frequency of the heave and pitch motion are set equal as ω, and the associated time period is $T = 2\pi/\omega$. The nominal heave (H_0) is the maximum heave displacement of the hydrofoil pitch axis location relative to its average value, as illustrated in Figure 5-1. The nominal pitch angle (θ_0) is the maximum pitch angle achieved by the hydrofoil and is depicted in Figure 5-1. The phase shift φ_1 is the phase difference between the heave and pitch motions for a single hydrofoil (for which φ_2=0). In this study, $\varphi_1 = \pi/2$ such that the nominal pitch angle is achieved at the zero-heave location ($H = 0$) which occurs at $t/T = 0$ for a single hydrofoil.

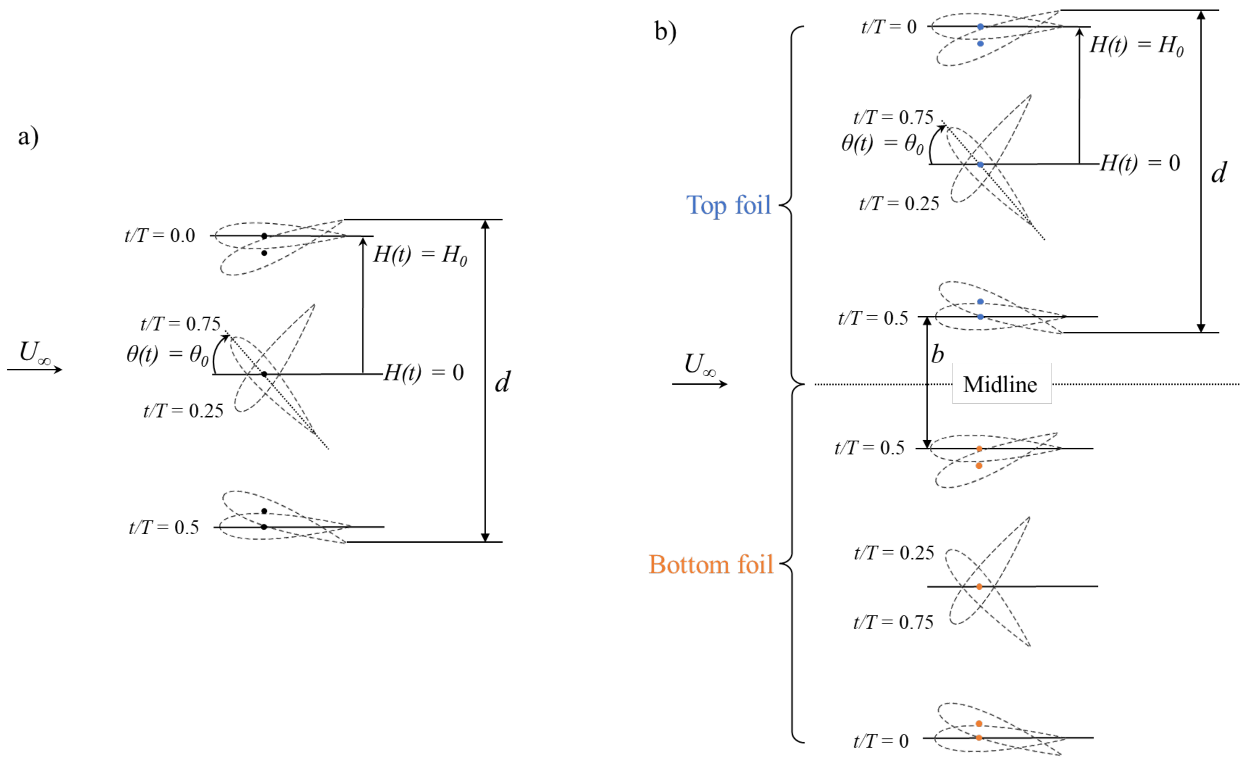

Figure 5-1. Kinematics of single and dual oscillating hydrofoils.

For the case where two hydrofoils are employed as shown in Figure 5-1b, the first (top) hydrofoil employs φ_2=0 for its motion (as is the case for a single hydrofoil) while the motion second (bottom) hydrofoil employs a phase difference of $\varphi_2 = \pi/2$. In this way, the two hydrofoils move in opposite directions (mirrored effect) and are farthest from each other at $t/T = 0$ and are nearest to each other at $t/T = 0.5$. As shown in Figure 5-1, the minimum vertical spacing between the two hydrofoil pitch centers at this time is denoted b. The midline between the two hydrofoils is the horizontal plane halfway between b. In addition, the total vertical distance traversed by the trailing edge of each hydrofoil is defined as d. The non-dimensional vertical range of the hydrofoil (d^*) was defined as the ratio of trailing-edge travel (d) to the chord length (c). If defines the hydrofoil span (s), the swept area of the hydrofoil based on pitch center is based on the nominal heave, i.e. $A_{pc} = 2H_0s$, while that based on the hydrofoil trailing edge is given as $A_{TE} = ds$. As such, A_{TE} is the true swept area and A_{pc} is the nominal swept area. This distinction is important when large pitch angles are employed, which yield significant excursions relative to the pitch axis, as is the case with the present study. It should also be noted that U_∞ corresponds to the flow speed far upstream of the hydrofoils.

5.2.2 Power Generation and Hydrodynamic Efficiency

The motion of an oscillating hydrofoil can be described as a combination of two degrees of freedom: heave and pitch. Heave is the vertical displacement of the hydrofoil and pitch is the rotation of the hydrofoil about its pitch axis. For fully prescribed simulations like the ones in this study, power is calculated from both degrees of freedom and the summation of the two components provides the instantaneous total mechanical power is (P_{tot}). Moments about the hydrofoil pitch axis are referenced to the pitch axis location at $c/3$. The net instantaneous power from both the heaving motion and the pitching motion is shown in Eq. 5.3. Note that these equations solely consider the resulting power due to the forces and moments on the foil from the fluid interactions and do not consider any cost of actuation or system efficiency that would be present in a physical device. The mean mechanical power over one period ($\overline{P_{\text{tot}}}$) is calculated using a time average as described in Eq. 5.4 based on the average power from the heaving motion and the average power from the pitching motion.

$$P_{\text{tot}}(t) = P_H(t) + P_\theta(t) = L\dot{H} + M\dot{\theta} \tag{Eq. 5.3}$$

$$\overline{P_{\text{tot}}} = \overline{P_H + P_\theta} \tag{Eq. 5.4}$$

The lift coefficient is used to nondimensionalize the lift force and is defined in Eq. 5.5 as the ratio of the instantaneous lift force to the product of dynamic pressure and the hydrofoil planform area where s and c are the hydrofoil span length and chord length respectively. Similarly, the pitching moment coefficient shown in Eq. 5.6 is used to nondimensionalize the moments around the hydrofoil pitch center (at $c/3$ for this study). For two-dimensional simulations, C_l and C_m are given per unit span.

$$C_l = \frac{L}{0.5\rho U_\infty^2 sc} \tag{Eq. 5.5}$$

$$C_m = \frac{M}{0.5\rho U_\infty^2 sc^2} \tag{Eq. 5.6}$$

A power coefficient is used to nondimensionalize the net instantaneous power generated from both heaving and pitching motions as show in Eq. 5.7.

$$C_P = \frac{P}{0.5\rho U_\infty^3 sc} \tag{Eq. 5.7}$$

The hydrodynamic efficiency (η_{hydro}) is used to assess an oscillating hydrofoil system's ability to extract the power available in the incoming flow over a swept region. This is defined as the ratio of the total mean mechanical power generated ($\overline{P_{\text{tot}}}$) over one period to the available power from the river within the hydrofoil swept area and is defined in Eq. 5.8. This swept area is the product of the span (*s*) and a vertical swept distance (*d*). This vertical distance is sometimes defined as the vertical distance traversed by the pitch axis but is often more stringently defined as the larger vertical distance traversed by the trailing edge of the hydrofoil [124].

$$\eta_{\text{hydro}} = \frac{\overline{P_{\text{tot}}}}{\frac{1}{2}\rho U_{HP}^{3} d s} \qquad \text{Eq. 5.8}$$

For this study, the latter definition based on the trailing-edge is employed since the large pitch angles are employed, which yield significant excursions relative to the pitch axis. The pitch axis was set at the $c/3$ behind the leading edge in this study, to be consistent with the experiments performed at Lehigh University [123]. The trailing-edge swept distance (*d*) is then calculated based on the pitch and heave kinematics, yielding the hydrodynamic power efficiency defined in Eq. 5.8. Note that for the dual hydrofoil simulations, η_{hydro} is calculated only for one of the two hydrofoils rather than both foils combined.

Since the 2-D numerical approach used in the present study was validated using three-dimensional experimental results, finite aspect ratio corrections were considered to explain differences. While there is no theoretical aspect ratio correction for an oscillating hydrofoil with shed vortices, as a first approximation one may consider the theoretical aspect ratio correction for a wing in steady conditions with a single bound vortex. In particular, Prandtl's finite wing theory [137] can be used to determine the circulatory forces due to downwash from the tip vortices to translate a 2-D lift coefficient (infinite span) to a 3-D lift coefficient (finite span). The theoretical result is a reduction in lift by the ratio of $AR/(AR+2)$ where AR is the wing aspect ratio defined as the ratio of the span to the chord, i.e. $AR = s/c$ [138]. If the moment about the pitch center is assumed to be due to just lift (neglecting drag), the same correction can be assumed to apply to the pitching moments. Under these assumptions along with the proportionality between power and lift force as well as between hydrodynamic efficiency and power, this scaling is applied directly to the 2-D hydrodynamic efficiencies from numerical simulations to estimate the hydrodynamic efficiency of a foil with a finite *AR* as shown in Eq. 5.9. The same approach can be used using Helmbold's relation for low *AR* wings resulting in Eq. 5.10 [139].

$$\eta_{Hembold} = \eta_{\text{hydro}} \left(\frac{AR}{\sqrt{AR^2 + 4} + 2} \right) \qquad \text{Eq. 5.9}$$

$$\eta_{Prandtl} = \eta_{\text{hydro}} \left(\frac{AR}{AR+2}\right) \quad \text{Eq. 5.10}$$

These 3-D aspect ratio corrections were applied to the numerical validation cases to help interpret the comparison to the experimental efficiencies.

The last two relevant parameters used in describing oscillating hydrofoil kinematics is the Strouhal number (St), which characterizes the frequency of the hydrofoil oscillations relative to that of the freestream flow over the vertical trailing-edge swept distance as expressed in Eq. 5.11 [113].

$$\text{St} = \frac{fd}{U_{HP}} \quad \text{Eq. 5.11}$$

The Strouhal number is useful since it can be adjusted to ensure that LEVS from the hydrofoil contributes to high efficiency hydrofoil kinematics and also helps determine the maximum foil speed relative to the freestream speed.

The Froude number (defined in Eq. 5.12) is a dimensionless quantity used to describe the relative impacts of inertia and gravity on fluid motion and is useful in characterizing free surface conditions in open channel flow as in riverine flow [134]. The limit of Fr → 0 represents flows where hydrostatic forces dominate such that there is little variation in the free surface. At the other limit Fr >> 1, hydrostatic forces become negligible and the free surface shape is mostly influenced by other sources, e.g. hydrofoil heaving motions.

$$\text{Fr} = \frac{U^2}{gh} \quad \text{Eq. 5.12}$$

The Froude number limits are effectively explored in this study as they pertain to the extremes of confinement benefits between the hydrofoil and the free surface.

5.3 Numerical Methods

5.3.1 Numerical Approach

Two-dimensional, pressure-based, transient simulations were performed using the commercial finite volume code Ansys Fluent to solve the unsteady viscous Navier-Stokes equations. The pressure-velocity coupling used is based on the fully-implicit scheme that couples the momentum and pressure-based continuity equations. With the overset meshing used this study, a bounded second-order implicit scheme is used to discretize time for higher accuracy compared to the alternative first-order implicit scheme. Second-order schemes are used for the spatial discretization of pressure and momentum equations. A least square cell-based method is used to determine gradients within the cell (determined by minimizing the squared errors between the cell's value and the extrapolated values from neighboring cells). Finally, to ensure spatial and temporal independence, the number of cells and reduce the timestep size until minimal changes in forces, moments, and hydrodynamic efficiency were obtained for a baseline flow condition (as discussed in Section 5.3.3).

To simulate pitching and heaving hydrofoil motions while maintaining fixed, slip horizontal walls, the numerical simulations were performed using an overset mesh approach, where a component mesh is overlaid on a background mesh, allowing for prescribed motions of the component mesh within the flow domain of the background mesh, which is held stationary to include upper and lower walls. Field values from the background mesh are interpolated to the cells in the component mesh at each time step. The component mesh motion is defined at each time step in terms of hydrofoil pitch velocity, heave velocity, and pitch axis location. For the oscillating hydrofoil simulations, the component mesh contains the hydrofoil with a no slip exterior condition surrounded by a structured O-mesh as shown in Figure 5-2. The background mesh is a cartesian grid with varying resolution in the streamwise direction for computational efficiency and has dimensions of the desired flow domain size. The area of the mesh elements in outermost layer of the component O-mesh are within 9% of those in the finer background mesh region for all simulations performed in this study.

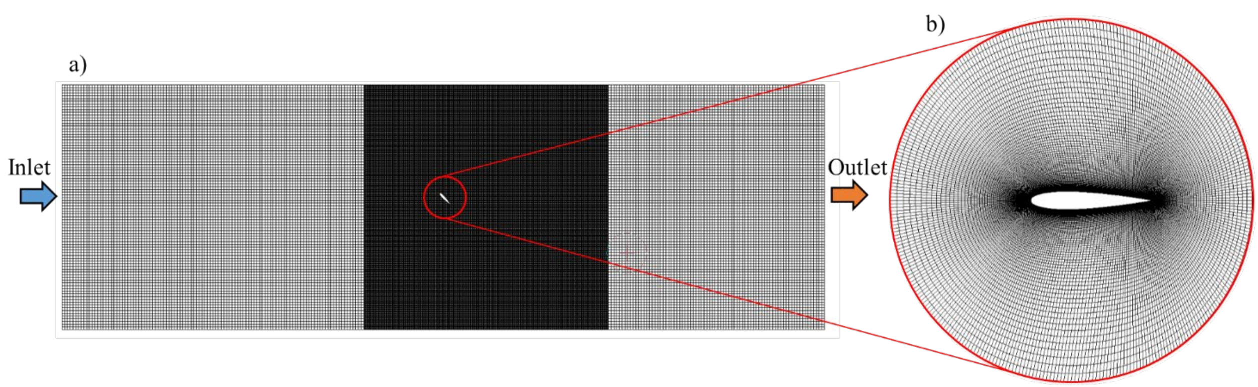

Figure 5-2. Meshes used for overset meshing approach for the validation simulations: a) stationary background mesh showing hydrofoil at a given instant, b) moving component mesh around the moving hydrofoil.

The inflow conditions were set as steady while the outflow boundary conditions were set using pressure. A no-slip viscous boundary condition was used on the hydrofoil surface while an inviscid slip boundary condition was used on the horizontal walls. For a single hydrofoil, this effectively neglects the boundary layers forming on the wall surface, but this is deemed as reasonable since the focus is on the localized flow around the hydrofoil. For the dual hydrofoil condition, the lower wall was set at the midline between the two hydrofoils, so that only the upper hydrofoil need be computed. Simulations where both hydrofoils were included provided the same results, as expected.

It should be noted that the use of two-dimensional Navier-Stokes equations presents limitation to the results. For the lab-scale Reynolds number of 10,000, the boundary layers over the hydrofoils are expected to be highly laminar and two-dimensional if aspect ratio effects are not considered. However, three-dimensional features will form due to instabilities in the separated shear layers, and these can greatly impact the wake structures. Fortunately, the impact of the localized flow around the hydrofoil surface (which determines the instantaneous lift and drag and thus energy extraction efficiency) is expected to be primarily two-dimensional based on experiments at similar Reynolds numbers [123].

For the field-scale Reynolds number used here of 378,000, the boundary layers over the hydrofoils are still expected to be laminar but the wake is expected to transition quickly into turbulent flow conditions. In this case, the assumption of two-dimensional flow around the hydrofoil is not as reasonable. A more accurate approach is to employ a three-dimensional grid and a numerical method that also captures the aspect ratio effects as well as three-dimensional flow features due to instabilities, which can greatly impact the wake structures. However, higher three-dimensionality is expected at field-scale Reynolds numbers. Based on the requirements for grid independence, this would be expected to require running such simulations with the full Navier-Stokes equations and a finite aspect ratio would be require more than one hundred million grid cells for a single case (and take more than 500 times longer to compute). This is impractically large if one also wishes to conduct a parametric study with (many cases) as is the objective here. Another option is to employ turbulence modeling or Large Eddy Simulations at the field-scale Reynolds numbers [136]. However, the present study sought to avoid empiricism of turbulence modeling or subgrid turbulence modeling and also sought to use two-dimensional Navier-Stokes to be consistent with the approach used for validation with the lab-scale simulations. However, it is recognized that the lack of three-dimensionality is a significant limitation of this study and it recommended that future work examine the impact of three-dimensionality on the hydrofoil forces and energy extraction efficiency.

5.3.2 Experimental Setup and Test Conditions

Validation of the present numerical method was performed using data from tow tank oscillating hydrofoil experiments performed in the Unsteady Flow Interactions Lab at Lehigh University [123]. These experiments were performed at chord-based Reynold number of 1×10^4 with a surface piercing single-hydrofoil rig. The kinematics of the hydrofoil can be fully prescribed and thus can be matched with the present numerical simulations. The experiments employed a semi-submerged hydrofoil with a submerged vertical depth of $6c$. Given that the free surface acts like a mirror condition for these experiments, the results would be consistent with a full span of 12 chords with end tips on either side (AR = 12). The experimental setup is equipped to measure the vertical forces and pitching moments on the hydrofoil as it oscillates. Upon running simulations with comparable kinematics, force coefficients are compared between the experimental and numerical results. Experimental parameters are shown in Table 5-1.

Table 5-1. Experimental conditions.

Parameter	Value
c	0.055 m
H_0/c	0.656
d/c	2
Re	10,000
U_∞	0.182 m/s
St	0.3, 0.4, 0.5
θ_0	60°, 75°

5.3.3 Validation with 2-D Simulation Method

The size of the computational domain is matched to the size of the tow tank used in the experiments at Lehigh University to consider the same levels of confinement. A six-period simulation (6*T*) was run at each mesh resolution and the resulting 2-D hydrodynamic power efficiency (η_{hydro}) was calculated as per Eq. 5.8. To remove initialization effects, only the last five periods were used in evaluating η_{hydro}.

A timestep resolution study was completed for Re = 1×10^4 with $\mathrm{St} = 0.3$ and $\theta_0 = 75°$ (based on the conditions in Table 5-1). For these conditions, an increase in the number of timesteps per period ($T/\Delta t$) is consistent with a decrease in timestep and thus approaches a temporally-resolved solution. Changes in the time-dependent the lift coefficient (C_l) and pitch moment coefficients (C_m) are shown in Figure 5-3. While all resolutions gave very similar results, the results with 400 timesteps per period showed some significant underpredictions compared to the other three resolutions at around t/T = 0.65 and t/T = 0.85 in the lift curve. The results with 400 timesteps per period also produced different oscillations in the pitch moment for t/T between 0.4 and 0.6 and between 0.9 and 1.0. This suggested, that at least 800 timesteps per period was needed. In addition, convergence with respect to hydrodynamic efficiency was considered as shown in Table 5-2, where it was found that the variations were less 1% between 800 and 1200 $T/\Delta t$. As such, 800 timesteps per period was deemed reasonable and was used for validation with experimental results.

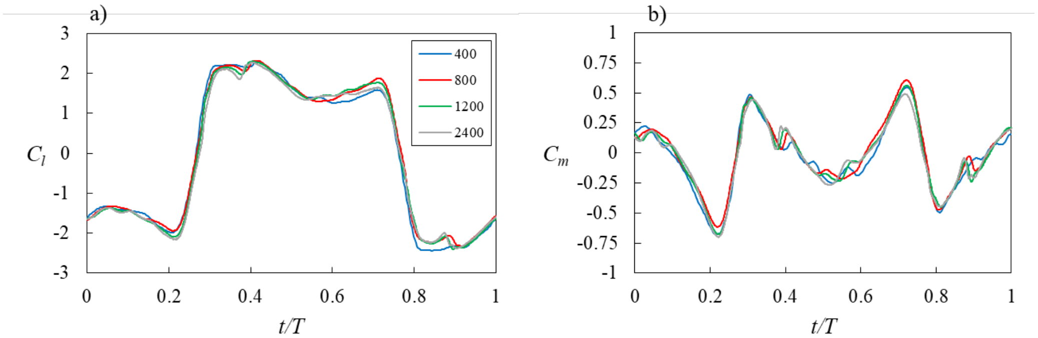

Figure 5-3. Timestep resolution study results; a) lift coefficient and b) pitch moment coefficient.

Table 5-2. Timestep resolution efficiency results.

Table 1.

$T/\Delta t$	η_{hydro} (2-D)
400	36.9%
800	36.3%
1200	36.6%

A mesh resolution study was also performed, and the number of elements in both the background and component mesh combined are shown as a function of the hydrodynamic power efficiency in Table 5-3. The background mesh consisted of fine and course mesh regions as shown in Figure 5-2. The finer mesh region spans from 5c upstream to 10c downstream of the hydrofoil to more accurately capture vortex structures from the leading edge and in the wake. The resolution of the finer mesh regions aimed to match the resolution of the outermost layers of the component mesh farthest from the hydrofoil. Mesh refinement was primarily produced by increasing resolution within the component mesh, particularly near the hydrofoil where resolution of the Leading-Edge Vortex structures directly impacts lift and pitching moments and thus efficiency. For the boundary layer two mesh resolutions tested, the increase in component mesh resolution corresponds to a decrease in the height of the first layer at the hydrofoil surface from 90 μm to 45 μm. Negligible difference was observed in the hydrodynamic efficiency between the two cases. Based on these results, 167,873 cells were found to be reasonable for the lab-scale conditions (Re=10^4). Although the resolution used was efficiently handled with the computational resources available, an even courser mesh could be sufficient in resolving the necessary flow structures for increased computational efficiency.

Table 5-3. Boundary layer mesh Resolution Efficiency Results.

Surface mesh height	Total mesh elements	Component mesh elements	η_{hydro} (2D)
45 μm	178,873	34,960	35.8%
90 μm	167,873	24,960	35.7%

Based on the above mesh resolution and timestep size, four cases were simulated for validation with the experimental data. The four different cases simulated vary in both Strouhal number and nominal pitch angle (θ_0). To compare the results, both experiments and simulation were converted to lift coefficient (C_l) and pitch moment coefficient (C_m) as shown in Figure 5-4.

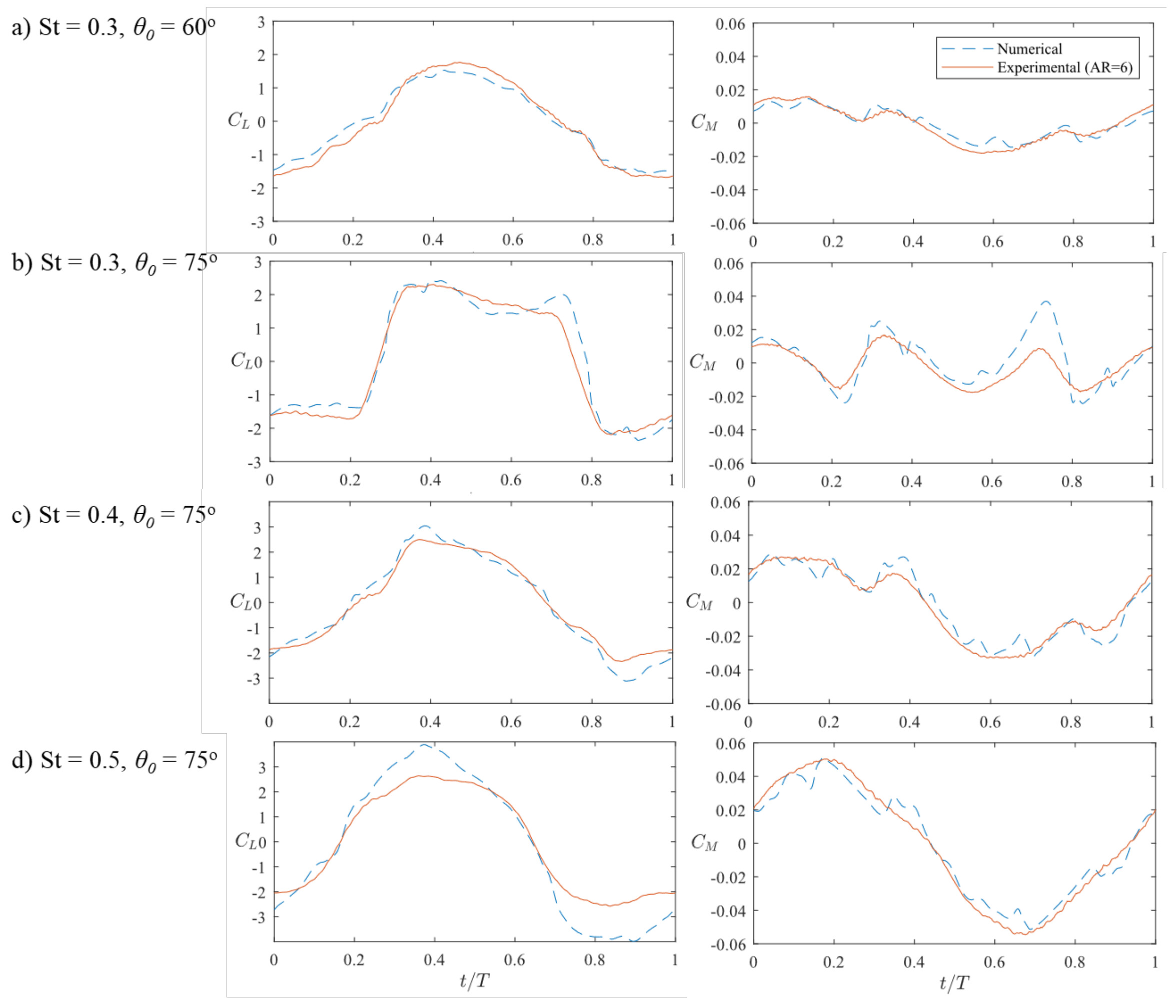

Figure 5-4. Lift coefficient and pitch moment comparison between numerical and experimental results at varying Strouhal numbers and nominal pitch angles.

In Figure 5-4a, c and d, the experimental lift coefficient varied somewhat sinusoidally due to effects of leading-edge vortex formation which can allow much higher lift coefficients than can be achieved for a steady-state flow. However, the conditions of Figure 5-4b showed rapid changes, which are associated with leading edge dynamic stall effects, due to pronounced angles of attack. All these experimental trends for lift were captured by the simulations. However, the simulations tended to predict more pronounced lift coefficients as the Strouhal number increased, especially for Figure 5-4d. In particular, this simulation predicted a very high peak lift coefficients (>3), which would be expected to be reduced if finite aspect ratio effects (tip vortices) would be included.

In terms of the moment coefficients, the trends and peak values were reasonably reproduced, but the simulations included additional high-frequency fluctuations. This can be attributed to small scale flow features associated with the two-dimensional simulations whereas such features are likely to be impacted by three-dimensional effects for the experiment and less likely to be pronounced due to spanwise integration.

The hydrodynamic efficiency was also compared between the simulations and experiments and is shown in Figure 5-5. The two-dimensional numerical and three-dimensional experimental efficiencies are calculated based on Eq. 5.8. For the cases shown in Figure 5-4a-c, the 2-D numerical efficiencies differ from the experimental efficiencies by less than 3% with the numerical values consistently higher than the experimental values. These differences are due to variations in lift force and pitch moment over one period. The close C_l and C_m curves shown in Figure 5-4 produce efficiency values that are likewise similar. However, over-prediction of the peak C_l at higher Strouhal numbers in Figure 5-4c-d are the primary reason for the overprediction of hydrodynamic efficiencies seen in Figure 5-5b. This can be related to three-dimensional effects and the finite aspect ratio.

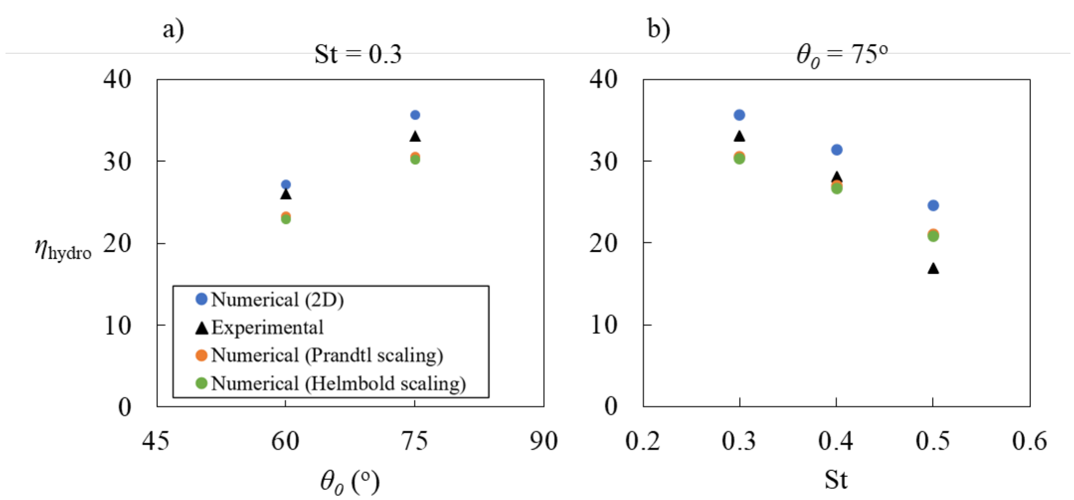

Figure 5-5. Single-foil hydrodynamic efficiency comparison between numerical and experimental results at varying Strouhal numbers and pitch angles.

To approximately account for finite aspect ratio effects present in the experimental results, the classic lifting-line theory Prandtl and Helmbold corrections (Eqs. 7a and 7b) were applied based on a full-span aspect ratio (AR) of 12. When Prandtl and Helmbold efficiency corrections are used, the numerical efficiencies underpredict hydrodynamic efficiency by 1 – 3% for the cases at St = 0.3 and 0.4 but still overpredict at St = 0.5. While the two-dimensional simulation has the same degree of confinement in the heave direction as used in the experiments, it should be noted that the experimental efficiencies may be enhanced from the additional confinement due to the proximity of the hydrofoil spanwise end tip to the tank floor, which can serve to minimize tip losses. In such a case, the Prandtl and Helmbold equations would cause an overcorrection, which is consistent with experimental data generally lying in between the bounds of the simulations with corrections and those without corrections. Furthermore, these corrections are based on a stationary bound vortex whereas the flow fields here are highly complex and include continually shed vortices. In addition, a practical hydrofoil system may include vertical struts at the ends, which would reduce tip losses, (e.g. act like winglets). Most importantly, the results indicate that the simulations can capture the same trends in unsteady lift and moment coefficients and can capture the same trends for the changes in hydrodynamic efficiency in terms of pitch angles and Strouhal numbers, where St=0.3 and θ_0=75° gives the highest hydrodynamic efficiency both experimentally and numerically.

5.4 Dual Hydrofoil Numerical Test Conditions

5.4.1 Dual-foil Symmetry Approach

Following the experimental validation of the overset mesh approach, a second hydrofoil was considered to examine the impact of a dual-foil configuration at laboratory Reynolds numbers. The second foil is vertically spaced from the first hydrofoil as shown in Figure 5-1b. The use of a symmetry boundary at the midline was employed as shown in Figure 5-6 to generally save computational costs needed for running dual hydrofoil simulations. This symmetry condition was verified by running a case (St = 0.3 and $\theta_0 = 70°$.) with two hydrofoils and comparing the results. Both approaches produced the same 2-D hydrodynamic efficiency of 41.2% and there were minimal differences in the C_l and C_m curves and in the leading-edge vortex shedding (LEVS) patterns around the hydrofoil. Based on these results, the mirrored approach was adopted for the subsequent full-scale dual hydrofoil simulations due to the significantly reduced computational cost compared to the fully modelled mesh. In particular, this same dual-foil configuration using a symmetry boundary condition was scaled up to field-scale Reynolds numbers and three confinement conditions were generated to consider the Froude number extremes and to quantify the effects of the dual hydrofoil configuration on hydrodynamic efficiency. More details of the field-scale Reynolds numbers and Froude number extremes are discussed in the following.

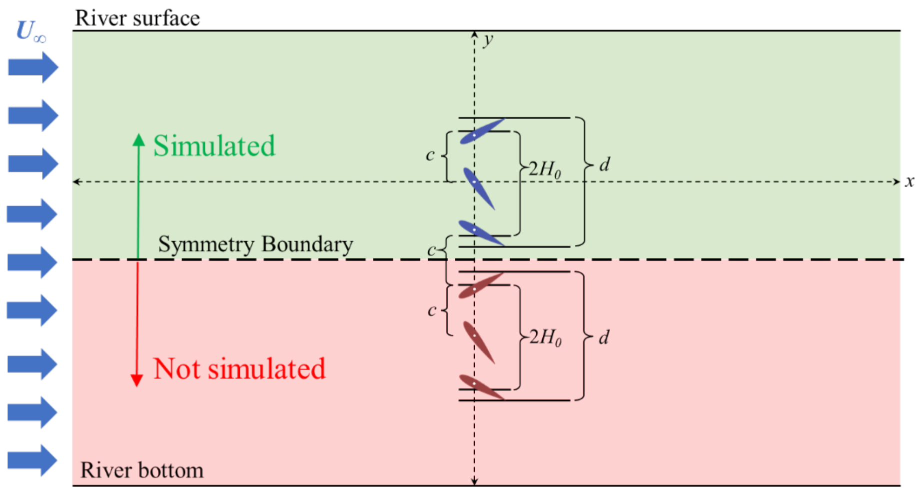

Figure 5-6. Schematic of the mirrored approach with symmetry boundary condition.

5.4.2 Field-scale Conditions

The dual hydrofoil simulations were scaled up based on a potential field site in the Kvichak River, located in Alaska [26]. While the riverine flow conditions and bathymetry vary with location and season, average values of the Kvichak River were considered for the full-scale simulations. Based on the average river depth of 2.4 m, the hydrofoil pitch centers were set to have a vertical heave range ($2H_0$) in the middle of this depth such that the full vertical span covered by the hydrofoils covered 1.5 m. This allowed 0.45 m clearance to the free surface and to the riverbed as shown in Figure 5-7. The free surface clearance is helpful to avoid potentially damaging interactions with floating logs and branches (it is assumed that this portion of the river would be closed to boat traffic) while the riverbed clearance is helpful to avoid rocks and topographical surface variations (due to currents and sediment) that might lead to a foil impact. These clearances may be adjusted with a more in-depth assessment of the site conditions and environmental risks.

To be approximately consistent with the lab-scale conditions, the vertical heave range was set at $2c$ ($H_0/c = 1$) based on a pitch axis location of $c/3$. Notably, the trailing edge vertical travel (d) is greater than that of pitch center travel due to the motion defined by Eqs. 1a and 1b. Based on $\theta_0 = 70^{\circ}$ (the mean θ_0 value used in generating the efficiency maps shown in Section 5.5.2), this resulted in $d = 2.5c$ for a single hydrofoil, about 25% larger than the heave range. The vertical hydrofoil spacing (b) was then set to the ratio relative to chord was $b^* = b/c = 1$. As a result, the total vertical distance spanned by both hydrofoils combined (referenced at the trailing-edge) is $5.5c$ as shown in Figure 5-7. For this to fit within the 1.5 m useable range, the hydrofoil chord length is calculated to be 0.273 m. Based on the average flow speed of the Kvichak River of 1.4 m/s, the chord-based field-site Reynolds number (Re_{field}) is approximately

$3.78{\times}10^5$. It should be noted that these are not optimized conditions but can be considered typical values for a field-scale demonstration test.

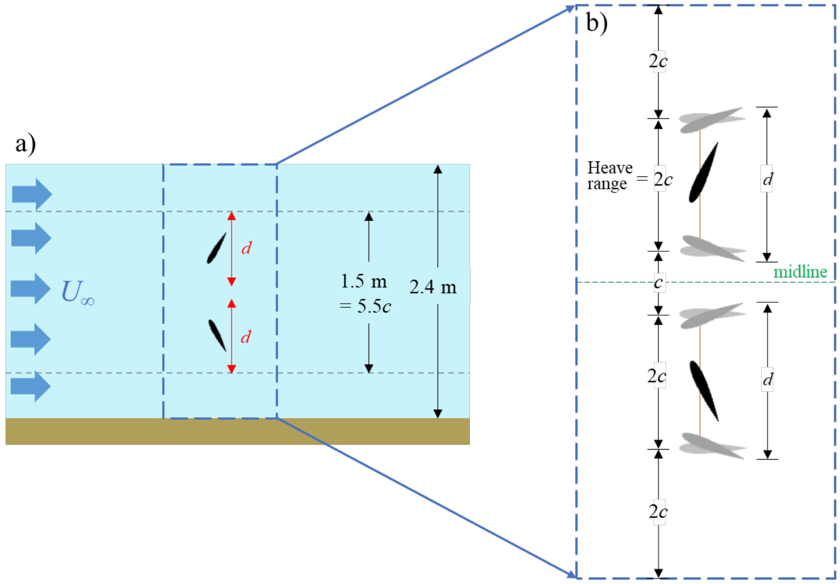

Figure 5-7. Kvichak River assumptions used to scale up simulations to field-site Reynolds numbers.

The streamwise extent of the field-site background mesh was set as 25*c* upstream and downstream of the hydrofoils for a total of 50c (shown in Figure 5-8a). As was done in the laboratory scale simulations, a more refined mesh region was generated from 5*c* upstream to 10*c* downstream of the hydrofoil in order to capture the higher resolution leading-edge and wake vortex structures. Since the Reynolds number was increased from 10,000 to 378,000, the mesh resolution and timestep size were reevaluated using the same approach as described in Section 5.3.3. From this, it was determined that 1200 timesteps/period and 243,750 mesh elements (148,200 in the background mesh and 95,550 in the component mesh) was sufficient to simulate the necessary flow structures and allow for hydrodynamic efficiency to converge to within 1%. Notably, Gauthier et al. conducted similar resolution studies and found a similar temporal resolution of 1,000 timesteps/period flow was reasonable but that only 70,000 grid cells were needed on a plane, where their lower spatial resolution is due to their use of turbulence modeling, which was consistent with their higher Reynolds number for a tidal system, and their interest in including three-dimensional effects [136].

5.4.3 Dual-Foil Benefits and Froude Number Limits

As noted in the introduction, dual-oscillating hydrofoils can benefit from confinement effects arising from three different sources:

1) Confinement between the hydrofoils (when their trailing edges approach)
2) Confinement due to the riverbed below

3) Confinement due to the free surface above.

The first effect can be examined by comparing a single hydrofoil to a dual hydrofoil configuration, as will be shown in the next section. The single hydrofoil simulations used the background mesh shown in Figure 5-8c where the mesh in Figure 5-8b is mirrored about the midline and the average hydrofoil heave position is now along the midline as well. The second and third effects are included with the flow domain described in Figure 5-8, where there is only a $2c$ gap to the solid wall conditions and the free surface is assumed to be always level. To investigate the difference associated with these effects, additional simulations were run where the gap to the solid wall was increased to $25c$ as shown in Figure 5-8b. This can be considered as the limit for a very deep river where the hydrofoils are far from the surface and far from the riverbed (negligible flow blockage). This will be denoted as the "unconfined dual-foil" and will be compared to the "confined dual-foil" of Figure 5-8 in the next section. The unconfined condition can also be notionally similar to the condition where the free surface readily deflects due to the presence of the top hydrofoil and the riverbed is far enough below to produce negligible blockage.

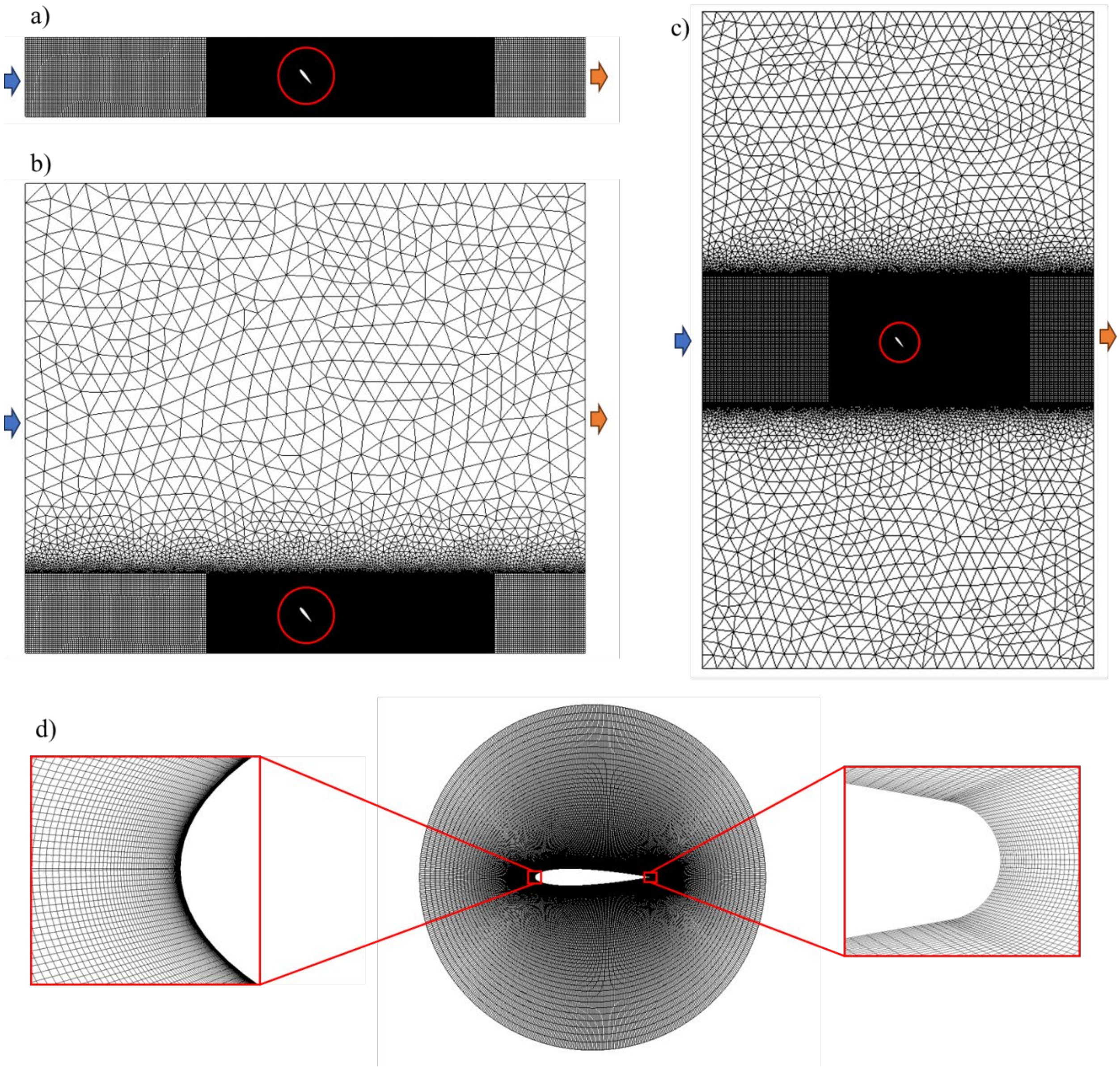

Figure 5-8. Meshes used in field scale numerical simulations. a) Confined dual-foil background mesh, b) unconfined dual-foil background mesh, c) unconfined single foil background mesh, d) component mesh with close up of leading and trailing edge mesh elements.

In particular, Figure 5-9 shows a notional diagram of the free surface effects for various Froude numbers (Fr), as defined by Eq. 5.12. The dual hydrofoil mesh with a completely level free surface is consistent with Fr = 0 condition, where hydrostatic effects dominate so the hydrofoil heaving motion has no effect on free surface deformations, as shown in Figure 5-9a. While not realistic, this case should be expected to produce the maximum level of confinement effects between the top hydrofoil and top boundary. At the other extreme, a case where Fr >> 1 and the riverbed is very deep is considered with the unconfined dual hydrofoil mesh. This limit assumes that the free surface fully deforms to adapt to the heaving motion of the top hydrofoil such that confinement effects are negligible as shown in Figure 5-9c. Realistically, a dual hydrofoil system will perform in between these two extremes on the order of Fr ~ 1 (Figure 5-9b). For the conditions of Figure 5-7 where h = 2.4 m and U_∞ = 1.4 m/s based on the Kvichak river, the river Froude number is 0.083 so the free surface can be assumed to be nearly level in terms of flow blockage effect [134]. However, there will also be free surface fluctuations based on the hydrofoil vertical movement and proximity to the free surface. In this case, a trailing edge hydrofoil Froude number can be defined based on the average hydrofoil vertical speed and the minimum gap between the trailing edge and the free surface. This Froude number is about tenfold higher indicating unsteady confinement effects may be important.

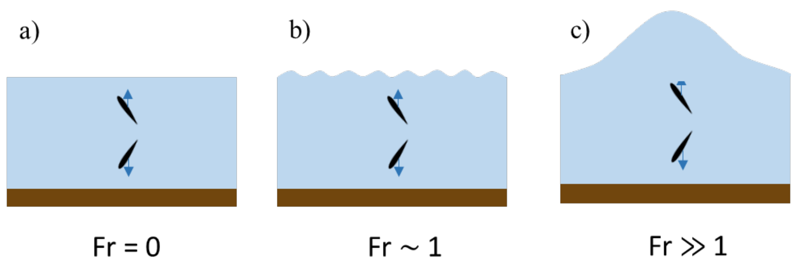

Figure 5-9. Froude number limits assumed in dual hydrofoil simulations for a) Fr = 0, b) Fr ~ 1, and c) Fr>>1.

Numerical simulations were performed for a range of St and θ_0 for all three confinement configurations cases (confined dual-foil, unconfined dual-foil, and unconfined single-foil). Confinement effects were especially investigated for conditions where high efficiency was expected. The confined dual-foil case and the unconfined single-foil case was also run for more detailed conditions with θ_0 ranging from 50º to 90º in increments of 10º to generate efficiency maps.

5.5 Results and Discussion

5.5.1 Confinement effects

To investigate the various effects of confinement (confined dual-foil, unconfined dual-foil, and unconfined single-foil), six cases at the field-scale Re were selected to simulate based on the conditions where peak hydrodynamic efficiency is expected: St = 0.4, 0.5, and 0.6 as well as θ_0 = 80º and 90º.

The power coefficient curves shown in Figure 5-10 indicate the portions where the dual-foil confined case outperforms the other two confinement levels. There are two main portions of one heave period that enhance C_P of the confined dual-foil cases. The peaks in C_P at t/T ~ 0.2 and t/T ~ 0.95 occur when the hydrofoil is close to the confined free surface. Likewise, the peaks in C_P at t/T ~ 0.35 and t/T ~ 0.6 occur when the hydrofoil is close to the midline where the dual-foils are the closest. The peaks at t/T ~ 0.35 and

$t/T \sim 0.95$ appear to be from momentary increases in C_l due to dynamic stall effects while the peaks at $t/T \sim 0.2$ and $t/T \sim 0.6$ are caused by the greater C_l magnitude in these regions due to confinement as seen in Figure 5-10. Pitching moment contributes to power much less significantly than lift forces but primarily provide benefits around $t/T \sim 0.95$.

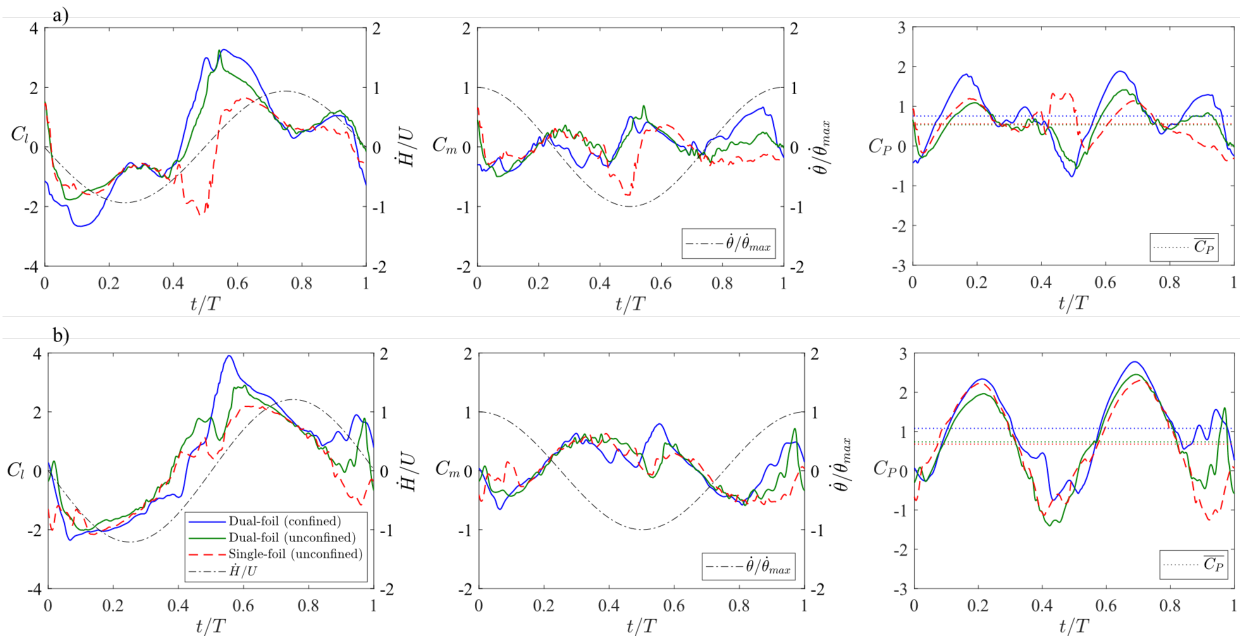

Figure 5-10. Lift coefficients, pitching moment coefficients, and power coefficients for all three levels of confinement at a) St = 0.4 and θ_0 = 90º and b) St = 0.5 and θ_0 = 80º.

The unconfined dual-foil cases show similar trends in C_l and C_m to the confined dual-foil cases but have smaller magnitudes around $t/T \sim 0.2$ and $t/T \sim 0.95$ on average across all six simulations likely due to the lack of confinement where the free surface is (Fr >> 1). The C_l and C_m for unconfined single-foil cases did not always match the trends for the dual-foil simulations as seen in Figure 5-10a where LEVS at $t/T = 0.5$ is significant compared to the other two confinement levels. The specific differences between the single-foil and dual-foil curves varied depending on St and θ_0. Across all six simulations however, there is a consistent reduction in C_l around $t/T = 0.5 – 0.6$ for the unconfined single-foil cases compared to either of the dual-foil cases, indicating that the confinement between the hydrofoils enhances C_l in this region. Although the differences between C_l and C_m curves between the unconfined dual-foil and single-foil simulations varied from case to case, the resulting average C_P was consistently nearly the same while the average C_P of the confined dual-foil cases was consistently higher.

Vorticity contours for the St = 0.5, θ_0 = 80º case shown in Figure 5-11 further illustrate the differences between the three confinement levels. Larger and more coherent vortex structures are observed shedding along the hydrofoil for the confined dual-foil case at $t/T = 0.18$, $t/T = 0.38$, and $t/T = 0.88$. It is less clear at $t/T = 0.56$, however, the Cl curves in Figure 5-10 indicate that there are benefits when the two hydrofoils become close to each other. Differences between the unconfined single-foil and dual-foil vorticity contours may be expected to appear at $t/T = 0.38$ and $t/T = 0.56$ of the t/T values shown, however, visually it is difficult to assess the difference in strength of the shed vortex structures between the two.

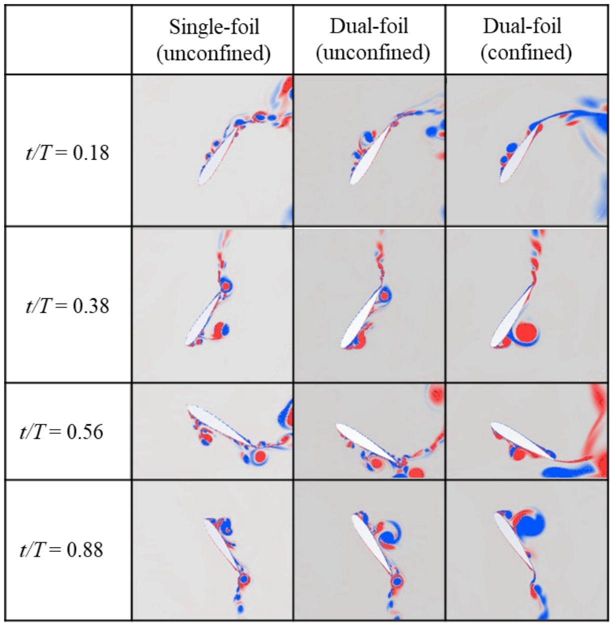

Figure 5-11. Vorticity contours at various t/T points for all three levels of confinement at St = 0.5 and θ_0 = 80º.

Hydrodynamic efficiency was also compared for the three confinement levels and can be considered relative to the theoretical actuator disk limit for an unconfined turbine, i.e. the Betz limit of 16/27 = 59.3%. The values for a confined turbine given theoretically by Garrett and Cummins [134] and empirically by Su *et al.* [164] are not shown since they both yield non-physical efficiencies of greater than 100% for the nominal blockage ratio (A_{TE}/A_c) of 4/9, where the true blockage ratio is even higher.

For the unconfined cases, there is no consistent indication that the unconfined dual-foil configuration improves efficiency of just one hydrofoil. For example, at a nominal pitch angle of 80º, the unconfined dual-foil efficiency at St = 0.5 is higher by about 3% but the single-foil case produced practically an identical efficiency at St = 0.4 and even surpassed the unconfined dual-foil efficiency at St = 0.6 by almost 3%. However, at a nominal pitch angle of 90º, the unconfined dual-foil efficiencies are consistently larger than that of the single-foil between 2 – 5%. This indicates that confinement effects due to the proximity of the hydrofoils on hydrodynamic efficiency when they are closest to each other at the midline can be positive, but is relatively small despite the increased C_l observed in Figure 5-10. In contrast, a much larger improvement was found when considering the confined dual-foils, owing to the confinement benefits of the riverbed and the assumption of a completely level free surface. This benefit increases with Strouhal number, especially for a nominal pitch angle of 90º. At this high pitch angle the d value is reduced which may explain the improvement. These results are consistent with the results found by Su et al. where one-wall confinement was found to have limited benefits on efficiency while two-wall confinement showed significant benefits [22].

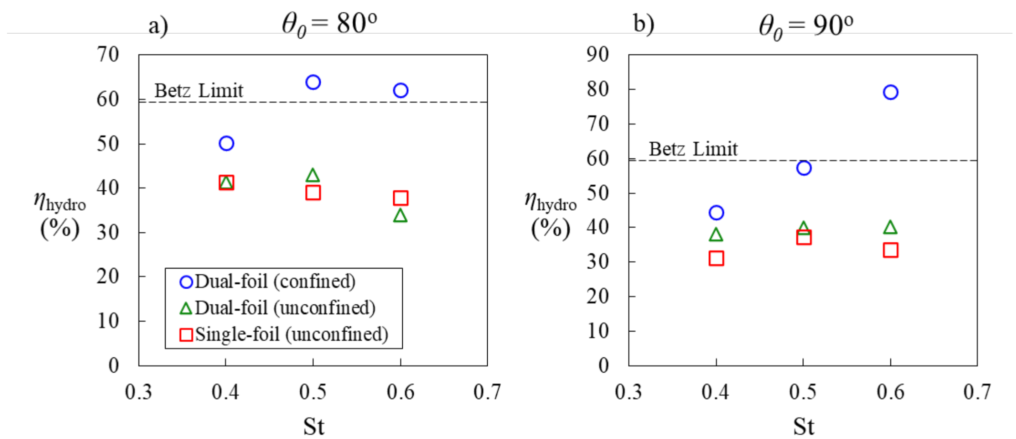

Figure 5-12. Hydrodynamic efficiency comparison of three confinement configurations simulated at nominal pitch angles of a) 80 degrees and b) 90 degrees.

As discussed previously, the confined and unconfined dual-foil simulations qualitatively represent two extreme Froude number limits if considering only the top hydrofoil. Thus, realistic efficiencies for the top hydrofoil are expected to fall within the range of efficiencies from these two levels of confinement. At Strouhal number increases, this predicted range grows for both the 80° and 90° nominal pitch angles, suggesting that although a single unconfined hydrofoil produced maximum efficiency around St = 0.4, higher Strouhal numbers produce better efficiencies in scenarios with sufficient flow confinement.

These results show that flow confinement due to riverine bed and free surface can produce significant benefits to hydrodynamic efficiency yet has been often neglected for the purpose of evaluating single hydrofoil performance in ideal conditions. The design of oscillating hydrofoil systems can be improved in terms of efficiency and cost by taking advantage of flow confinement benefits. While the results of this study suggest that determining the proximity of the hydrofoils to the free surface has more potential for increasing hydrodynamic efficiency, using a dual hydrofoil configuration may provide some additional performance enhancement at high nominal pitch angles. However, additional work is recommended to support this conclusion.

5.5.2 Dual vs. Single Foil Efficiencies

The efficiency maps for the confined dual-foil and unconfined single-foil simulations are shown below in Figure 5-13. From the present single-foil efficiency map (Figure 5-13a), the kinematics producing the highest efficiency yielded 41.5% at St = 0.4 and $\theta_0 = 80^o$. This point closely matches the optimum point found by Kinsey & Dumas in their parametric study of a single NACA0015 hydrofoil at a Re = 1100 [14].

Due to the significantly higher Re used in this study, there is boost in efficiency of about 7%, which is consistent with increases seen in previous studies [128].

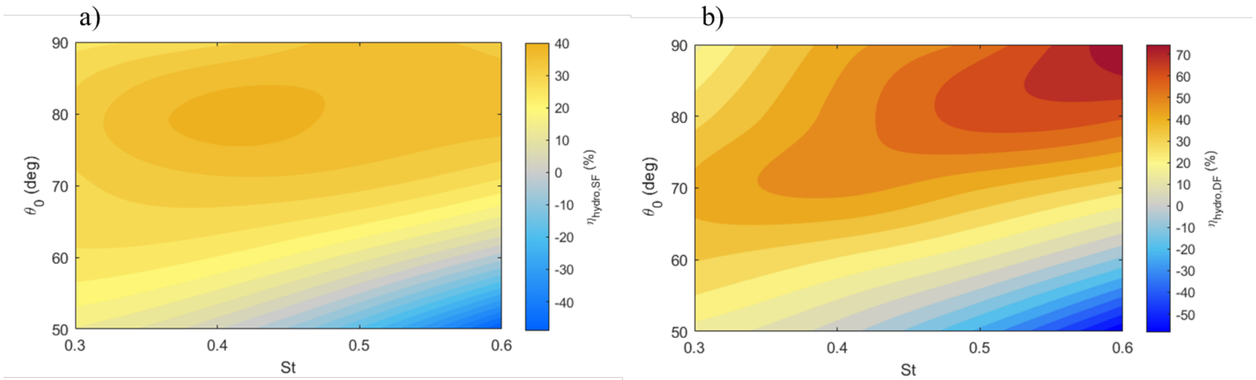

Figure 5-13. Hydrodynamic efficiency maps with Hembold scaling for a) unconfined single-foil simulations and b) confined dual-foil simulations.

When comparing to the confined dual-foil efficiencies shown in Figure 5-13b, clear differences are observed. At the single-foil optimum point of St = 0.4 and θ_0 = 80º, the dual-foil efficiency increases in comparison to 50.1%, a nearly 10% overall increase (and ~20% relative increase) in efficiency. Interestingly, the optimum point of the dual-foil case is even higher and occurs at a different condition. In particular, the confined dual-foil efficiency generally increases with both St and θ_0 with the highest efficiency occurring at St = 0.6 and θ_0 = 90º with a value of 79%, nearly twice that of the single-foil optimum. These results suggest that the dual-foil confinement used in the confined dual-foil simulations (due to dual-foil spacing and flow domain limits) can enhance hydrodynamic efficiency and potentially even surpass the Betz limit. For both configurations, high St and low θ_0 result in negative efficiencies. These areas of energy consuming kinematics remain the same on both single- and dual-foil efficiency maps.

The difference in efficiency between the confined dual-foil and unconfined single-foil simulations is shown in Figure 5-14. For the majority of the parametric space studied, the confined dual-foil configuration increases efficiencies, with largest difference of about 34% at St = 0.6 and θ_0 = 90º and a local maximum of about 15% at St = 0.4 and θ_0 = 70º. In some regions of the parametric space, the single-foil efficiency appears to surpass that of the dual-foil case as observed in the top left and bottom right corners of the map shown in Figure 5-14. However, the bottom right corners (high St, low θ_0) have negative efficiencies and so the system would not practically operate in this region. The upper left corner (low St and high θ_0) may be more practical if the Strouhal numbers are constrained by load limits (which can impact structural mass and cost) or inertial limits (which can depend on the system mass including that of the PTO). For example, at St = 0.3 and θ_0 = 90º, there is an approximately 6% drop in efficiency for the dual-foil configuration.

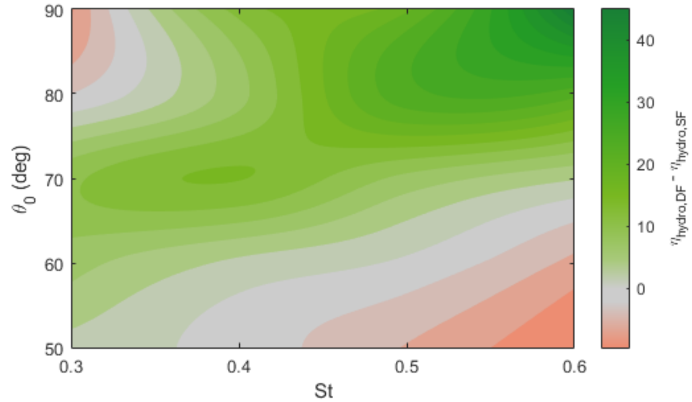

Figure 5-14. Difference between confined dual-foil and unconfined single-foil efficiencies.

5.6 Conclusions

Vertically-stacked dual hydrofoils can take advantage of confinement effects that arise due to the shallow depths in riverine environments to increase hydrodynamic efficiency. This study is the first to investigate the effects of confinement on dual hydrofoils oscillating symmetrically about a horizontal midplane at field-scale Reynolds numbers. In such configurations, flow confinement developed from interactions between the hydrofoils and the free surface, riverbed, and other hydrofoils. This study considers those interactions with the hydrofoil and an additional hydrofoil by considering Froude number limits where hydrodynamic efficiency values are expected to fall within.

Using a numerical methodology validated with lab-scale Reynolds number of 10,000 experiments, two-dimensional simulations were conducted at full-scale field Reynolds numbers of 378,000 to investigate various types of vertical confinement conditions on the fluid dynamics and energy extraction performance of vertically-stacked oscillating hydrofoils. This included a hydrofoil-induced confinement due to a dual-foil configuration where the hydrofoils dynamically approached other (mirrored about a horizontal midplane) and a river-geometry confinement where the level free surface above and a level riverbed below were modeled as solid but inviscid slip walls. The results showed that the hydrofoil dual-foil confinement resulted in strong differences in the local fluid dynamics. In particular, the shed vortices when the hydrofoils were near other yielded larger vortices with a much lower downstream convection speed. However, the hydrofoil-induced confinement impact on hydrodynamic efficiency was small and actually negative in some cases. In contrast, the river-geometry confinement had a much stronger influence on the hydrodynamic efficiency. The dependence of nominal pitch angle and Strouhal number on hydrodynamic efficiency (for energy extraction) for the river confined conditions was particularly strong, and conditions with St=0.6 and θ_0 = 90° yielded a hydrodynamic efficiency as high as 80%, significantly above the Betz-limit of 59%. This indicates that designing hydrofoils to take advantage of free surface and riverbed confinement can have very high benefits. However, computational investigation to examine the three-dimensional effects coupled with higher Reynolds number experiments are needed to determine whether such high efficiency benefits can be obtained in realistic conditions, especially once surface Froude number effects are considered. While considering Froude number limits allowed for simplification of free surface modelling in the simulations performed, future work may directly include free surface deformations as a comparison to the limits of hydrodynamic efficiencies predicted in this study. Additionally, the impact of vertically-stacked dual hydrofoils on downstream energy extraction potential (tandem dual hydrofoil systems) is important to consider in weighing the benefits of this dual-foil configuration. Furthermore, the cost of actively pitching a hydrofoil is expected to decrease hydrodynamic efficiency and mitigate some of the benefits due to confinement. This cost will be a necessary calculation for oscillating hydrofoil systems (single or multiple foil) to reach commercial deployment.

Chapter 6

Conclusions

6.1 Summary and Key Results

In Chapter 2, a rotor design methodology was developed for extreme scale wind turbines and applied to generate three 25 MW downwind rotor designs of different chord length distributions. This methodology included a new optimization approach for rotor geometry to consider optimum rotor tilt and coning based on aeroelastic deflections at sub-rated conditions. The primary design objectives were to both maximize power production while minimizing rotor mass, and thus minimize Levelized Cost of Energy. Rotor aerodynamic geometry was optimized by developing a design space using new empirical correlations to model 2-D flatback airfoil characteristics in terms of maximum lift coefficient and drag coefficient. Within this design space, lift coefficient and chord distributions were developed for three rotors. The three different design stages (PROPID, OpenFAST, WISDEM) were used to design the three rotors and the results indicated that the design with the moderate chord distribution (Design 2) was the optimum by having the highest power coefficient (PROPID), the highest power production (OpenFAST), as well as the lightest blade and lowest LCOE (WISDEM).

In Chapter 3, pitch system requirements for a 25 MW downwind offshore turbine with advanced blade pitch control are explored. A model for predicting pitching power and pitch actuator torque was presented and applied to turbines ranging from 5 MW to 50 MW to determine scaling laws for peak pitch moments, actuator torque, and pitching power consumed. The results indicate that the maximum pitch rates and accelerations both are largest for low Region 3 mean wind speeds (just above rated wind speeds), highlighting that the combination of high thrust and high turbulence as critical for determining pitch system power requirements. Maximum required pitch actuator torque was found to be greatest at higher Region 3 wind speeds, correlating with maximum pitching moments. Additionally, the OpenFAST simulations performed in this chapter verified reliable performance of the 25 MW rotor design from Chapter 2 under extreme turbulent wind conditions.

Chapter 4 transitions from wind energy to riverine hydrokinetics. The effect of freestream turbulence on hydrodynamic efficiency was investigated experimentally, with a semi-passive hydrofoil (where pitch is controlled but heave is driven by fluid forces). Results from the laboratory scale semi-passive testing apparatus suggested that turbulent flow (around 5% turbulence intensity) consistently improved energy harvesting performance both in terms of kinematics (peak heave velocities magnitudes and higher heave-to-chord ratios), forces, and power extraction. The difference in hydrodynamic efficiency between the baseline and turbulent flow conditions tested grew with flow speed. The reason for this improvement may be due to increased turbulence intensity levels in the flow reducing flow separation around the hydrofoil during periods where the pitch is held nearly constant, resulting in greater vertical forces and heave velocities that contribute to increased power generation. However, there was no clear indication of the impact of turbulence on Leading-Edge Vortex Shedding, which is considered an important characteristic of oscillating hydrofoil systems. Regardless, efficiencies in excess of 50% were achieved with turbulent flow conditions, the highest seen among experimental studies using semi-passive systems.

Lastly, in Chapter 5, confinement effects due to shallow riverine depths and vertically-stack dual hydrofoils were numerically investigated at field-scale Reynolds numbers using two-dimensional Navier-Stokes equations with steady inflow and a fully prescribed trajectory for both pitch and heave. Compared to an unconfined single hydrofoil, the dual foil configuration (also without confinement) provided minimal benefits in terms of hydrodynamic efficiency despite noticeable differences in local fluid dynamics from the interaction between the dual hydrofoils. However, when a horizontal free surface and riverbed confinement was introduced, the hydrodynamic efficiency increased to values as high as 80%, significantly exceeding the 59.2% Betz limit for unconfined performance. This improvement in efficiency due to confinement was sensitive to changes in hydrofoil kinematics and tended to occur at high St and θ_0 for these field-scale Reynolds numbers. These results indicate that confinement due to hydrofoil proximity to the free surface and/or riverbed can be utilized to significantly improve energy harvesting performance. However, three-dimensional effects were not included in these simulations even though the flow is expected to have significant spanwise velocity fluctuations and turbulent structures. In addition, the hydrofoil is expected to have tip vortices and power losses due to finite aspect ratios. Furthermore, the free surface and riverbed are unlikely to be entirely horizontal, which will generally reduce the confinement benefits. Finally, the impact of turbulence and semi-passive control (consistent with riverine energy harvesting as noted in Chapter 4) should also be explored.

6.2 Contributions to the Field

This dissertation contributes to the field of offshore wind energy in several ways. First, a new robust rotor design methodology (Chapter 2) was developed for designing extreme scale rotors. This methodology is expected to be applicable to a wide range of turbines regardless of upwind/downwind configurations, number of blades, or rotor size. The resulting best 25 MW design also serves as a reference turbine that can be utilized in future research. Similarly, the approach developed in Chapter 3 for peak pitch requirements is applicable to turbines at various scales, although pitch drive inertia data from larger existing turbines may improve estimates as extreme scale turbines continue to grow even larger. Chapter 3 additionally introduces a novel scaling model for blade pitch inertia was developed that considers aeroelastic effects and pitch system dynamics to estimate pitch actuator torque. In evaluating peak pitch requirements for turbines ranging from 5 MW to 50 MW, power laws were found for scaling peak pitching moments, actuator torque, and pitching power with the product of blade mass and average blade chord length.

This dissertation also contributes to the field of oscillating hydrokinetic hydrofoils in the following ways: The experimental work demonstrated that turbulence improves energy harvesting performance and especially at higher flow speeds (up to ~5% efficiency improvement at a flow speed of 0.85 m/s). The dynamics of a semi-passive system, particularly the influence of gravity on hydrofoil kinematics and thus efficiency, is also better understood from analysis of hydrofoil pitch and heave motions. Numerically, the benefits toward hydrodynamic efficiency due to flow confinement were characterized for a fully prescribed dual hydrofoil system at realistic Reynolds numbers. In doing so, techniques for potentially exceeding the Betz limit are suggested.

6.3 Recommended Future Work

In Chapter 2, as the focus of this study was on rotor aerodynamics, structural and controller considerations in the design process may be included to produce a more comprehensive design approach. Future work may also study the parametric spaces of pre-cone angle and shaft tilt angle under more realistic unsteady wind conditions to further maximize rotor swept area.

In Chapter 3, while the method developed estimates required actuator torque and pitching power, it is crucial to consider how these requirements will impact costs that drive commercial growth of offshore turbines. It is recommended that subsequent studies should connect the pitching power and torque requirements to capital and operating costs, so the direct impact on LCOE can be captured. Pitch drive inertia data from larger turbines needed to scale drive inertias up is expected to improve the accuracy of the methods presented. Pitch bearing friction effects should be considered in future analysis. In addition, future work may consider trade-offs involving pitch control type, rotor orientation, yaw effects, or floating platforms to refine pitch actuator torque requirements further.

The results in Chapter 4 present many opportunities for future work. The turbulence levels achievable in the experimental set up are lower than what hydrofoils may experience in real riverine flow conditions. Increasing turbulence intensity in the current facility may be possible, however, 3-D numerical simulations are also recommended to further investigate the flow physics behind the increasing in efficiency observed in more turbulent flow. Additionally, riverine flow will have a shear velocity profile which was not accounted for in this chapter. Fluid imaging techniques may provide similar insights experimentally and are recommended as well. The turbulence generator used is capable of producing sheared inflow and can be used in future work to address this effect. Lastly, the limited size of the water channel is expected to have induced flow confinement on the hydrofoil. These experiments can be paired with numerical simulations to quantify confinement effects in the experimental results.

The most significant drawback of the simulations performed in Chapter 5 is the lack of three-dimensionality. Especially at the higher Reynolds numbers at which hydrofoils will operate in, 3-D effects are expected to reduce hydrodynamic efficiency due to finite aspect ratios and should be studied. Future simulations should transition from 2-D to 3-D to investigate these effects. Utilizing 3-D simulations will also allow for injecting turbulence and/or shear in the flow as recommended from Chapter 4. Furthermore, the free surface and riverbed are unlikely to be entirely horizontal and the impact of these surface variations are important to consider. In addition, the impact of turbulence, flow shear, free surface effects and semi-passive control (consistent with riverine energy harvesting as noted in Chapter 4) should also be explored.

References

[1] IEA, 2017. Energy Technology Perspectives 2017: Catalysing Energy Technology Transformations. OECD, Paris, France. https://doi.org/10.1787/energy_tech2017-en

[2] U.S. Energy Information Administration. (2024). Short-Term Energy Outlook. EIA. https://www.eia.gov/outlooks/steo/

[3] U.S. Energy Information Administration. (2024). ElectricPower Monthly [Data report]. EIA. https://www.eia.gov/electricity/monthly/

[4] McCoy, A., Musial, W., Hammond, R., Hernando, D. M., Duffy, P., Beiter, P., Pérez, P., Baranowski, R., Reber, G., & Spitsen, P. (2024). Offshore Wind Market Report: 2024 Edition (Technical Report NREL/TP-500-90525). National Renewable Energy Laboratory

[5] Shields, M., Beiter, P., Nunemaker, J., Cooperman, A., Duffy, P., "Impacts of turbine and plant upsizing on the levelized cost of energy for offshore wind," Applied Energy 298, 117189, 2021. http://dx.doi.org/10.1016/j.apenergy.2021.117189.

[6] Loth, E., Steele, A., Qin, C., Ichter, B., Selig, M. S., Moriarty, P., "Downwind pre-aligned rotors for extreme-scale wind turbines," Wind Energy, Vol. 20, 1129-1311, 2017. https://doi.org/10.1002/we.2092

[7] Muljadi, E., & Butterfield, C. P. (2001). Pitch-controlled variable-speed wind turbine generation. IEEE Transactions on Industry Applications, 37(1), 240–246. https://doi.org/10.1109/28.903156

[8] Bossanyi, E. A. "Wind turbine control for load reduction." *Wind Energy: An International Journal for Progress and Applications in Wind Power Conversion Technology* 6.3 (2003): 229-244.

[9] Bossanyi, Ervin A. "Further load reductions with individual pitch control." *Wind Energy: An International Journal for Progress and Applications in Wind Power Conversion Technology* 8.4 (2005): 481-485.

[10] ACEP. (2020). Tanana River Test Site (TRTS)—MHK Device Design Criteria [River Energy Resource Assessment]. Alaska Center for Energy and Power.

[11] El Fajri, O., Bowman, J., Bhushan, S., Thompson, D., & O'Doherty, T. (2022). Numerical study of the effect of tip-speed ratio on hydrokinetic turbine wake recovery. Renewable Energy, 182, 725–750. https://doi.org/10.1016/j.renene.2021.10.030

[12] Young, John, Joseph CS Lai, and Max F. Platzer. "A review of progress and challenges in flapping foil power generation." *Progress in aerospace sciences* 67 (2014): 2-28.

[13] Picard-Deland, M., Olivier, M., Dumas, G., & Kinsey, T. (2019). Oscillating-foil turbine operating at large heaving amplitudes. *AIAA Journal*, *57*(12), 5104-5113.

[14] Kinsey, T., & Dumas, G. (2008). Parametric study of an oscillating airfoil in a power-extraction regime. *AIAA journal*, *46*(6), 1318-1330.

[15] Simpson, B. J. (2009). Experimental studies of flapping foils for energy extraction [Thesis, Massachusetts Institute of Technology]. https://dspace.mit.edu/handle/1721.1/55283

[16] Deng, J., Teng, L., Pan, D., & Shao, X. (2015). Inertial effects of the semi-passive flapping foil on its energy extraction efficiency. Physics of Fluids, 27(5), 053103. https://doi.org/10.1063/1.4921384

[17] Teng, L., Deng, J., Pan, D., & Shao, X. (2016). Effects of non-sinusoidal pitching motion on energy extraction performance of a semi-active flapping foil. Renewable Energy, 85, 810–818. https://doi.org/10.1016/j.renene.2015.07.037

[18] Webb, P. W. (2002). Kinematics of plaice, Pleuronectes platessa, and cod, Gadus morhua, swimming near the bottom. Journal of Experimental Biology, 205(14), 2125-2134.

[19] Xu, W., Xu, G., Duan, W., Song, Z., & Lei, J. (2019). Experimental and numerical study of a hydrokinetic turbine based on tandem flapping hydrofoils. Energy, 174, 375–385. https://doi.org/10.1016/j.energy.2019.02.188

[20] Kinsey, T., Dumas, G., Lalande, G., Ruel, J., Méhut, A., Viarouge, P., Lemay, J., & Jean, Y. (2011). Prototype testing of a hydrokinetic turbine based on oscillating hydrofoils. Renewable Energy, 36(6), 1710–1718. https://doi.org/10.1016/j.renene.2010.11.037

[21] Dahmani, F., & Sohn, C. H. (2020b). Effects of the downstream spatial configuration on the energy extraction performance of tandem/parallel combined oscillating hydrofoils. Journal of Mechanical Science and Technology, 34(5), 2035–2046. https://doi.org/10.1007/s12206-020-0425-8

[22] Su, Y., Miller, M., Mandre, S., & Breuer, K. (2019). Confinement effects on energy harvesting by a heaving and pitching hydrofoil. Journal of Fluids and Structures, 84, 233–242. https://doi.org/10.1016/j.jfluidstructs.2018.11.006
[23] Dahmani, F., & Sohn, C. H. (2020a). Effect of convergent duct geometry on the energy extraction performance of tandem oscillating hydrofoils system. Journal of Fluids and Structures, 95, 102949. https://doi.org/10.1016/j.jfluidstructs.2020.102949
[24] Wu, J., Qiu, Y. L., Shu, C., & Zhao, N. (2014). Pitching-motion-activated flapping foil near solid walls for power extraction: A numerical investigation. Physics of Fluids, 26(8), 083601. https://doi.org/10.1063/1.4892006
[25] Wu, J., Yang, S. C., Shu, C., Zhao, N., & Yan, W. W. (2015). Ground effect on the power extraction performance of a flapping wing biomimetic energy generator. Journal of Fluids and Structures, 54, 247–262. https://doi.org/10.1016/j.jfluidstructs.2014.10.018
[26] Guerra, M., & Thomson, J. (2019). Wake measurements from a hydrokinetic river turbine. Renewable Energy, 139, 483–495. https://doi.org/10.1016/j.renene.2019.02.052
[27] U.S. Department of Energy (DOE), "Wind Vision: A New Era for Wind Power in the United States," 2015.
[28] The White House, "Biden Administration Jumpstarts Offshore Wind Energy Projects to Create Jobs," 2021, [accessed April, 2023]. https://www.whitehouse.gov/briefing-room/statements-releases/2021/03/29/fact-sheet-biden-administration-jumpstarts-offshore-wind-energy-projects-to-create-jobs/.
[29] Siemens Gamesa Renewable Energy, "Powered by Change: Siemens Gamesa Launches 14 Offshore Direct Drive Turbine with 222-meter Rotor," Press Release, 2020 [accessed February, 2022]. https://www.siemensgamesa.com/en-int/-/media/siemensgamesa/downloads/en/newsroom/2020/05/siemens-gamesa-press-release-turbine-14-222-dd-en.pdf.
[30] Costoya, X., DeCastro, M., Carvalho, D., Gómez-Gesteira, M., "On the Suitability of Offshore Wind Energy Resource in The United States of America for the 21st Century," Applied Energy 262, 114537, 2020. https://doi.org/10.1016/j.apenergy.2020.114537.
[31] Caglayan, D. G., Ryberg, D. S., Heinrichs, H. U., Linssen, J., Stolten D., Robinius, M., "The Techno-Economic Potential of Offshore Wind Energy with Optimized Future Turbine Designs in Europe," Applied Energy 255, 113794, 2019. https://doi.org/10.1016/j.apenergy.2019.113794.
[32] Qin, C., Loth, E., Zalkind, D., Pao, L., Yao, S., Griffith, T., Selig, M., Damiani, R., "Downwind Coning Concept Rotor for a 25 MW Offshore Wind Turbine," Renewable Energy, Vol. 156, 314-327, 2019. https://doi.org/10.1016/j.renene.2020.04.039.
[33] Griffith, T. D., Ashwill, T. D., "The Sandia 100-meter All-glass Baseline Wind Turbine Blade: SNL100-00," Technical Report SAND2011-3779, Sandia National Laboratories, 2011.
[34] Selig, M. S., Tangler, J. L., "Development and Application of a Multipoint Inverse Design Method for Horizontal Axis Wind Turbines," Wind Engineering, Vol. 19, No. 5, 91–105, 1995.
[35] Selig, M. S., "PROPID for Horizontal Axis Wind Turbine Design," 1995-, https://m-selig.ae.illinois.edu/propid.html.
[36] Selig. M. S., "PROPID User Manual Version 5.3.1," UIUC Applied Aerodynamics Group, 2012.
[37] Ananda, G. K., Bansal S., Selig, M. S., "Aerodynamic Design of the 13.2 MW SUMR-13i Wind Turbine Rotor," AIAA Paper 2018–0094, Wind Energy Symposium, 2018. https://doi.org/10.2514/6.2018-0994.
[38] NREL: WISDEM, v3.2.0, GitHub [code], available at: https://github.com/WISDEM/WISDEM.
[39] NREL: OpenFAST, v2.5.0, GitHub [code], available at: https://github.com/OpenFAST/openfast.
[40] TPI Composites, Inc., "Innovative Design Approaches for Large Wind Turbine Blades," Technical Report SAND2004-0074, Sandia National Laboratories, 2004. https://doi.org/10.2172/809617.
[41] Drela, M., "XFOIL: An Analysis and Design System for Low Reynolds Number Airfoils," Low Reynolds Number Aerodynamics. Lecture Notes in Engineering, Vol. 54, 1-12, 1989. https://doi.org/10.1007/978-3-642-84010-4_1.
[42] Drela, M., "XFOIL Subsonic Airfoil Development System," 2000- [accessed April, 2021]. http://web.mit.edu/drela/Public/web/xfoil/.
[43] Coder, J. G., Maughmer, M. D., "Comparisons of Theoretical Methods for Predicting Airfoil Aerodynamic Characteristics," Journal of Aircraft, Vol. 51, No. 1, 183-191, 2014. https://doi.org/10.2514/1.C032232.
[44] Stone, C., Barone, M., "A Computational Study of the Aerodynamics and Aeroacoustics of a Flatback Airfoil Using Hybrid RANS-LES," AIAA Paper 2009-273, 47th AIAA Aerospace Sciences Meeting, 2009. https://doi.org/10.2514/6.2009-273

[45] Metzinger, C. N, Chow, R., Baker, J. P., Cooperman, A. M., van Dam, C. P., “Experimental and Computational Investigation of Blunt Trailing-Edge Airfoils with Splitter Plates,” AIAA Journal, Vol. 56, 3229-3239, 2018. https://doi.org/10.2514/1.J056098.

[46] Baker, J. P., Mayda, E. A., van Dam, C. P., "Experimental Analysis of Thick Blunt Trailing-Edge Wind Turbine Airfoils," Journal of Solar Energy Engineering, Vol 128, 422-431, 2006. https://doi.org/10.1115/1.2346701.

[47] Ning, S. A., “AirfoilPrep.py Documentation Release 0.1.0,” NREL/TP-5000-58817, National Renewable Energy Laboratory, Golden, CO (US), 2013.

[48] Moriarty, P.J., Hansen, A.C., “AeroDyn Theory Manual,” NREL/TP-500-36881, National Renewable Energy Laboratory, Golden, CO (US), 2005.

[49] Escalera Mendoza, A. S., Griffith, D. T., Qin, C., Loth, E., Johnson, N., “Rapid approach for structural design of the tower and monopile for a series of 25 MW offshore turbines,” The Science of Making Torque from Wind (TORQUE 2022), 2022. https://doi.org/10.1088/1742-6596/2265/3/032030

[50] Yao, S., Cheta, M., Griffith, T. D., Escalera Mendoza, A. S., Selig, M. S., Martin, D., Kianbakht, S., Johnson, K., Loth, E., “Aero-structural design and optimization of 50 MW wind turbine with over 250-m blades,” Wind Engineering, Vol 46, 273-295, 2022. https://doi.org/10.1177/0309524X211027355

[51] International Electrotechnical Commission, “IEC 64100-1, Third Ed. 2005-2008, Wind Turbines – Part I: Design Requirements,” IEC, 2005.

[52] Timmer, W. A., van Rooij, R. P. J. O. M, “Summary of the Delft University Wind Turbine Dedicated Airfoils,” Journal of Solar Energy Engineering, Vol. 124, 488-496, 2003. https://doi.org/10.1115/1.1626129.

[53] Berg. D., Barone, M. F., “Aerodynamic and Acoustic Properties of a Flatback Airfoil (Will it Rumble or Whisper),” Technical Report SAND2008-4306P, Sandia National Laboratories, 2008.

[54] Barone, M. F., Berg, D., “Aerodynamic and Aeroacoustic Properties of a Flatback Airfoil: An Update,” Technical Report SAND2008-8243C, Sandia National Laboratories, 2008. https://doi.org/10.2514/6.2009-271.

[55] Manolesos, M., Voutsinas, S. G., “Experimental Study of Drag-Reduction Devices on a Flatback Airfoil,” AIAA Journal, Vol. 54, 3382-3396, 2016. https://doi.org/10.2514/1.J054901.

[56] Yilmaz, O., Timmer, W. A., “Experimental Evaluation of a Non-Conventional Flat Back Thick Airfoil Concept for Large Offshore Wind Turbines,” AIAA Paper 2018-3827, AIAA Applied Aerodynamic Conference, 2018. https://doi.org/10.2514/6.2018-3827.

[57] Althaus, D., “Niedriggeschwindigkeitsprofile: Profilentwicklungen und Polarenmessungen im Laminarwindkanal des Instituts für Aerodynamik und Gasdynamik der Universität Stuttgart,” Vieweg, 1996.

[58] Ribnitzky, D., Berger. F., Petrovic, V., Kuhn, M., “Hybrid-Lambda: A Low Specific Rating Rotor Concept for Offshore Wind Turbines,” Wind Energy Science, Preprint, 2023.

[59] Escalera Mendoza, A. S., Mishra, I., Griffith, T. D., “An Open-Source NuMad Model for the IEA 15 MW Blade with Baseline Structural Analysis,” AIAA Paper 2023-2093, AIAA SciTech Forum, 2023. https://doi.org/10.2514/6.2023-2093.

[60] GE Vernova. Haliade-x offshore wind turbine.

[61] Minyang Smart Energy Group. Offshore wind turbines.

[62] M. Jeong, E. Loth, C. Qin, M. Selig, and N. Johnson. Aerodynamic rotor design for a 25 MW offshore downwind turbine. Applied Energy, 353:122035, 2024.

[63] S. Kianbakht, D. Martin, K. E. Johnson, D. Zalkind, L. Y. Pao, E. Loth, J. Simpson, S. Yao, M. Chetan, and D. T. Griffith. Design space exploration and decision-making for a segmented ultralight morphing 50-MW wind turbine. Wind Energy, 25(12):2016–2035, 2022.

[64] S Escalera Mendoza, S. Yao, M. Chetan, and D. T. Griffith. Design and analysis of a segmented blade for a 50 MW wind turbine rotor. Wind Engineering, 46(4):1146–1172, 2022. Publisher: SAGE Publications.

[65] C. Anderson. Wind turbines: theory and practice. Cambridge University Press, 2020.

[66] K. Kragh, M. Hansen, and L. Henriksen. Sensor comparison study for load alleviating wind turbine pitch control. Wind Energy, 17(12):1891–1904, 2014.

[67] E. A. Bossanyi. Individual blade pitch control for load reduction. Wind Energy, 6(2):119–128, 2003.

[68] E. A. Bossanyi. The design of closed loop controllers for wind turbines. Wind Energy, 3(3):149–163, 2000.

[69] E. Bossanyi, A. Wright, and P. Fleming. Controller field tests on the NREL CART2 turbine. Technical Report NREL/TP-5000-49085, 1001440, National Renewable Energy Laboratory, 2010.

[70] M. Chiang. A novel pitch control system for a wind turbine driven by a variable-speed pump-controlled hydraulic servo system. Mechatronics, 21(4):753–761, 2011.

[71] X. Yin, Y. Lin, W. Li, Y. Gu, X. Wang, and P. Lei. Design, modeling and implementation of a novel pitch angle

control system for wind turbine. Renewable Energy, 81:599–608, 2015.

[72] J. Walgern, K. Fischer, P. Hentschel, and A. Kolios. Reliability of electrical and hydraulic pitch systems in wind turbines based on field-data analysis. Energy Reports, 9:3273–3281, 2023.

[73] James Carroll, Alasdair McDonald, and David McMillan. Failure rate, repair time and unscheduled O&M cost analysis of offshore wind turbines. Wind Energy, 19(6):1107–1119, 2016.

[74] R. I. Pelin, P. D. Bˆarsˇanescu, and I. Ti¸ta. Hydraulic systems used for pitch control of wind turbines: a literature overview. IOP Conference Series: Materials Science and Engineering, 444:042013, 2018.

[75] R. Gao and Z. Gao. Pitch control for wind turbine systems using optimization, estimation and com- pensation. Renewable Energy, 91:501–515, 2016.

[76] J. C. Dai, Y. P. Hu, D. S. Liu, and X. Long. Modelling and characteristics analysis of the pitch system of large-scale wind turbines. Proceedings of the Institution of Mechanical Engineers, Part C: Journal of Mechanical Engineering Science, 225(3):558–567, 2011. Publisher: IMECHE.

[77] J. Zhu, K. Ma, A. Hajizadeh, M. Soltani, and Z. Chen. Fault detection and isolation for wind turbine electric pitch system. In 2017 IEEE 12th International Conference on Power Electronics and Drive Systems (PEDS), pages 618–623. IEEE, 2017. Place: Honolulu, HI.

[78] S. Cho, E. E. Bachynski, A. R. Nejad, Z. Gao, and T. Moan. Numerical modeling of the hydraulic blade pitch actuator in a spar-type floating wind turbine considering fault conditions and their effects on global dynamic responses. Wind Energy, 23(2):370–390, 2020. eprint: https://onlinelibrary.wiley.com/doi/pdf/10.1002/we.2438.

[79] M. H. Hansen and B. S. Kallesoe. Servo-elastic dynamics of a hydraulic actuator pitching a blade with large deflections. Journal of Physics: Conference Series, 75:012077, 2007.

[80] L. J. Fingersh and K. E. Johnson. Controls advanced research turbine (CART) commissioning and baseline data collection. Technical Report NREL/TP-500-32879, 15002211, National Renewable Energy Laboratory, 2002.

[81] E. A. Bossanyi, P. A. Fleming, and A. D. Wright. Validation of individual pitch control by field tests on two- and three-bladed wind turbines. IEEE Transactions on Control Systems Technology, 21(4):1067– 1078, 2013. Conference Name: IEEE Transactions on Control Systems Technology.

[82] C. J. Bay, R. R. Damiani, L. J. Fingersh, S. Hughs, M. Chetan, S. Yao, D. T. Griffith, G. K. Ananda, M. S. Selig, D. Zalkind, L. Y. Pao, D. Martin, K. E. Johnson, M. Kaminski, and E. Loth. Design and testing of a scaled demonstrator turbine at the national wind technology center. In AIAA Scitech 2019 Forum, page 1068. American Institute of Aeronautics and Astronautics, 2019.

[83] J. Dai, Y. Hu, D. Liu, and X. Long. Calculation and characteristics analysis of blade pitch loads for large scale wind turbines. Science China Technological Sciences, 53(5):1356–1363, 2010.

[84] F. Zhang, J. Dai, D. Liu, L. Li, and X. Long. Investigation of the pitch load of large-scale wind turbines using field SCADA data. Energies, 12(3):509, 2019.

[85] M. Shan. Load Reducing Control for Wind Turbines: Load Estimation and Higher Level Controller Tuning based on Disturbance Spectra and Linear Models. Doctoral dissertation, University of Kassel, 2017.

[86] M. Stammler, F. Schwack, N. Bader, A. Reuter, and G. Poll. Friction torque of wind-turbine pitch bearings – comparison of experimental results with available models. Wind Energy Science, 3(1):97– 105, 2018. Publisher: Copernicus GmbH.

[87] A. S. Escalera Mendoza, D. T. Griffith, M. Jeong, C. Qin, E. Loth, M. Phadnis, L. Y. Pao, and M. S. Selig. Aero-structural rapid screening of new design concepts for offshore wind turbines. Renewable Energy, 219:119519, 2023.

[88] Srinivas Guntur, Jason Jonkman, Ryan Sievers, Michael A. Sprague, Scott Schreck, and Qi Wang. A validation and code-to-code verification of FAST for a megawatt-scale wind turbine with aeroelastically tailored blades. Wind Energy Science, 2(2):443–468, 2017.

[89] J. M. Jonkman, G. J. Hayman, B. J. Jonkman, R. R. Damiani, and R. E. Murray. AeroDyn v15 user’s guide and theory manual. Technical Report NREL/TP-XXX-XXXXX, National Renewable Energy Laboratory, 2017.

[90] National Renewable Energy Laboratory. Turbsim stochastic inflow turbulence simulator.

[91] M. Phadnis, A. S. Mendoza Escalera, M. Jeong, E. Loth, D. T. Griffith, M. Pusch, and L. Y. Pao. Comparison of 25 MW downwind and upwind turbine designs with individual pitch control. Journal of Physics: Conference Series, 2767(3):032039, 2024. Publisher: IOP Publishing.

[92] M. Pusch, M. Phadnis, M. Jeong, C. Qin, E. Loth, and L. Y. Pao. Impact of blade pitch actuation system on wind turbine cost and energy production. Journal of Physics: Conference Series, 2767(8):082006, 2024. Publisher: IOP Publishing.

[93] J. Jonkman, S. Butterfield, W. Musial, and G. Scott. Definition of a 5-MW reference wind turbine for offshore system development. Technical Report NREL/TP-500-38060, 947422, National Renewable Energy Laboratory, 2009.

[94] Daniel S. Zalkind, E. Dall'Anese, and L. Y. Pao. Automatic controller tuning using a zeroth-order optimization algorithm. Wind Energy Science, 5(4):1579–1600, 2020.

[95] K. E. Johnson, L. Y. Pao, M. J. Balas, and L.J. Fingersh. Control of variable-speed wind turbines: standard and adaptive techniques for maximizing energy capture. IEEE Control Systems Magazine, 26(3):70–81, 2006. Conference Name: IEEE Control Systems Magazine.

[96] G. Bir. Multi-blade coordinate transformation and its application to wind turbine analysis. In 46th AIAA Aerospace Sciences Meeting and Exhibit, pages 1300–1314. American Institute of Aeronautics and Astronautics, 2008. Place: Reno, Nevada.

[97] Xiao Chen. Experimental investigation on structural collapse of a large composite wind turbine blade under combined bending and torsion. Composite Structures, 160:435–445, 2017.

[98] Qin. C. (2024). Personal Communication.

[99] Gaertner, E., Rinker, J., Sethuraman, L., Zahle, F., Anderson, B., Barter, G. E., Abbas, N. J., Meng, F., Bortolotti, P., Skrzypinski, W., Scott, G. N., Feil, R., Bredmose, H., Dykes, K., Shields, M., Allen, C., & Viselli, A. (2020). IEA Wind TCP Task 37: Definition of the IEA 15-Megawatt Offshore Reference Wind Turbine (NREL/TP-5000-75698). National Renewable Energy Lab. (NREL), Golden, CO (United States). https://doi.org/10.2172/1603478

[100] Stehly, T., Duffy, P., & Mulas Hernando, D. (2023). 2022 Cost of Wind Energy Review (NREL/PR-5000-88335). National Renewable Energy Lab. (NREL), Golden, CO (United States).

[101] Victor Maldonado, Nicolas Peralta, Wolduamlak Ayele, Dioser Santos, and Guilherme Dufflis. Effect of blade aspect ratio on the performance tradeoff between figure of merit and bending-torsion dynamics of wind turbines with synthetic jets. Energy Reports, 9:4830–4843, 2023.

[102] New & Remanufactured Pitch Motors | GE & AMD Electric Motors For Wind Turbine | Pitch Motors Repair. (n.d.). Warfield Electric. Retrieved November 22, 2024, from https://www.warfieldelectric.com/pitch-motors.html

[103] McKinney, W., & DeLaurier, J. (1981). Wingmill: An Oscillating-Wing Windmill. Journal of Energy, 5(2), 109–115. https://doi.org/10.2514/3.62510

[104] Browning, E. (2022). An Analysis of Turbulent Effects on Hydrokinetic Power Generation [Master's Thesis, University of Alaska Fairbanks]. https://www.proquest.com/openview/e46f49b7f6c7fcad2794949c0cc99445/1?pq-origsite=gscholar&cbl=18750&diss=y&casa_token=z-IsUR_ubFQAAAAA:nCQzprpqRv5PPGxsq3WKxPO7qL0QFpgzWPrzjBlI4OCool8HOX-MQ94TFkbIO_1-dcImNMbhkg

[105] Birjandi, A. H., Woods, J., & Bibeau, E. L. (2012). Investigation of macro-turbulent flow structures interaction with a vertical hydrokinetic river turbine. Renewable Energy, 48, 183–192. https://doi.org/10.1016/j.renene.2012.04.045

[106] Zhu, J., White, C., Wainwright, D. K., Di Santo, V., Lauder, G. V., & Bart-Smith, H. (2019). Tuna robotics: A high-frequency experimental platform exploring the performance space of swimming fishes. Science Robotics, 4(34), eaax4615. https://doi.org/10.1126/scirobotics.aax4615

[107] Kinsey, T., & Dumas, G. (2012). Three-Dimensional Effects on an Oscillating-Foil Hydrokinetic Turbine. Journal of Fluids Engineering, 134(071105). https://doi.org/10.1115/1.4006914

[108] Ribeiro, B. L. R., Frank, S. L., & Franck, J. A. (2020). Vortex dynamics and Reynolds number effects of an oscillating hydrofoil in energy harvesting mode. Journal of Fluids and Structures, 94, 102888. https://doi.org/10.1016/j.jfluidstructs.2020.102888

[109] Lahooti, M., & Kim, D. (2019). Multi-body interaction effect on the energy harvesting performance of a flapping hydrofoil. Renewable Energy, 130, 460–473. https://doi.org/10.1016/j.renene.2018.06.054

[110] Sitorus, P. E., & Ko, J. H. (2019). Power extraction performance of three types of flapping hydrofoils at a Reynolds number of 1.7E6. Renewable Energy, 132, 106–118. https://doi.org/10.1016/j.renene.2018.07.116

[111] Yao, H., Wang, L., Zhang, H., & Liu, Y. (2024). Flow physics behind the wake of a flapping hydrofoil turbine near a wall. Physics of Fluids, 36(7), 075159. https://doi.org/10.1063/5.0209270

[112] Kim, D., Strom, B., Mandre, S., & Breuer, K. (2017). Energy harvesting performance and flow structure of an oscillating hydrofoil with finite span. Journal of Fluids and Structures, 70, 314–326. https://doi.org/10.1016/j.jfluidstructs.2017.02.004
[113] Xiao, Q., & Zhu, Q. (2014). A review on flow energy harvesters based on flapping foils. Journal of Fluids and Structures, 46, 174–191. https://doi.org/10.1016/j.jfluidstructs.2014.01.002
[114] Zhu, Q., Haase, M., & Wu, C. H. (2009). Modeling the capacity of a novel flow-energy harvester. Applied Mathematical Modelling, 33(5), 2207–2217. https://doi.org/10.1016/j.apm.2008.05.027
[115] Li, W., Wang, W.-Q., Yan, Y., & Tian, F.-B. (2018). Effects of pitching motion profile on energy harvesting performance of a semi-active flapping foil using immersed boundary method. Ocean Engineering, 163, 94–106. https://doi.org/10.1016/j.oceaneng.2018.05.055
[116] Liu, Z., Qu, H., & Shi, H. (2019). Performance evaluation and enhancement of a semi-activated flapping hydrofoil in shear flows. Energy, 189, 116255.https://doi.org/10.1016/j.energy.2019.116255
[117] Zhu, Q., & Peng, Z. (2009). Mode coupling and flow energy harvesting by a flapping foil. Physics of Fluids, 21(3), 033601. https://doi.org/10.1063/1.3092484
[118] Huxham, G. H., Cochard, S., & Patterson, J. (2012, December). Experimental Parametric Investigation of an Oscillating Hydrofoil Tidal Stream Energy Converter. 18th Australasian Fluid Mechanics Conference, Launceston, Australia.
[119] Engineering Business Limited. (2005). Stingray Tidal Stream Energy Device - Phase 3. U.K. Dept. of Trade and Industry, ETSU-T/06/00230/00/REP, URN No 05/864;
[120] Roberts, A., Thomas, B., Sewell, P., Khan, Z., Balmain, S., & Gillman, J. (2016). Current tidal power technologies and their suitability for applications in coastal and marine areas. Journal of Ocean Engineering and Marine Energy, 2(2), 227–245. https://doi.org/10.1007/s40722-016-0044-8
[121] Vinod, A., Han, C., & Banerjee, A. (2021). Tidal turbine performance and near-wake characteristics in a sheared turbulent inflow. Renewable Energy, 175, 840-852. https://doi.org/10.1016/j.renene.2021.05.026
[122] Qadri, M. N. M., Shahzad, A., Zhao, F., & Tang, H. (2019). An experimental investigation of a passively flapping foil in energy harvesting mode. Journal of Applied Fluid Mechanics, 12(5), 1547–1561. https://doi.org/10.29252/jafm.12.05.29648
[123] Moored, K. (n.d.). Unsteady Flow Interactions Laboratory. Lehigh University. https://wordpress.lehigh.edu/kwm213/
[124] Kinsey, T., & Dumas, G. (2014). Optimal Operating Parameters for an Oscillating Foil Turbine at Reynolds Number 500,000. AIAA Journal, 52(9), 1885–1895. https://doi.org/10.2514/1.J052700
[125] Vennell, R. (2013). Exceeding the Betz limit with tidal turbines. Renewable Energy, 55, 277–285. https://doi.org/10.1016/j.renene.2012.12.016
[126] Wang, Y., Huang, D., Han, W., YangOu, C., & Zheng, Z. (2017). Research on the mechanism of power extraction performance for flapping hydrofoils. Ocean Engineering, 129, 626–636. https://doi.org/10.1016/j.oceaneng.2016.10.024
[127] Li, X., Liang, C., Chen, C., Xiong, Q., Parker, R. G., & Zuo, L. (2020). "Optimum power analysis of a self-reactive wave energy point absorber with mechanically-driven power take-offs," Energy, 195, 116927. https://doi.org/10.1016/j.energy.2020.116927.
[128] Wang, Y., Sun, X., Huang, D., & Zheng, Z. (2016). Numerical investigation on energy extraction of flapping hydrofoils with different series foil shapes. Energy, 112, 1153–1168. https://doi.org/10.1016/j.energy.2016.06.092
[129] Liu, Z., Qu, H., & Shi, H. (2020). Energy-harvesting performance of a coupled-pitching hydrofoil under the semi-passive mode. Applied Energy, 267, 114889. https://doi.org/10.1016/j.apenergy.2020.114889
[130] Zhang, Y., Han, X., Hu, Y., Chen, X., Li, Z., Gao, F., & Chen, W. (2024). Dual-function flapping hydrofoil: Energy capture and propulsion in ocean waves. Renewable Energy, 222, 119956. https://doi.org/10.1016/j.renene.2024.119956
[131] Deng, J., Caulfield, C. P., & Shao, X. (2014). Effect of aspect ratio on the energy extraction efficiency of three-dimensional flapping foils. Physics of Fluids, 26(4), 043102. https://doi.org/10.1063/1.4872224

[132] Xu, J., Sun, H., & Tan, S. (2016). Wake vortex interaction effects on energy extraction performance of tandem oscillating hydrofoils. Journal of Mechanical Science and Technology, 30(9), 4227–4237. https://doi.org/10.1007/s12206-016-0835-9
[133] Kinsey, T., & Dumas, G. (2012). Optimal Tandem Configuration for Oscillating-Foils Hydrokinetic Turbine. Journal of Fluids Engineering, 134(031103). https://doi.org/10.1115/1.4005423
[134] Garrett, C., & Cummins, P. (2007). The efficiency of a turbine in a tidal channel. Journal of Fluid Mechanics, 588, 243–251. https://doi.org/10.1017/S0022112007007781
[135] Lefrancois, J. (2008). Optimisation du rendement d'une turbine multi-ailes `a l'aide d'une m´ethode lagrangienne par particules vortex [Thesis]. FACULTE DES SCIENCES ET DE GENIE UNIVERSITE LAVAL QUEBEC.
[136] Gauthier, E., Kinsey, T., & Dumas, G. (2016). Impact of Blockage on the Hydrodynamic Performance of Oscillating-Foils Hydrokinetic Turbines. Journal of Fluids Engineering, 138(091103). https://doi.org/10.1115/1.4033298
[137] Prandtl, L. (1920, July 1). Theory of lifting surfaces. https://ntrs.nasa.gov/citations/19930080806
[138] Ayancik, F., Zhong, Q., Quinn, D. B., Brandes, A., Bart-Smith, H., & Moored, K. W. (2019). Scaling laws for the propulsive performance of three-dimensional pitching propulsors. Journal of Fluid Mechanics, 871, 1117–1138. https://doi.org/10.1017/jfm.2019.334
[139] Polhamus, E. C. (1955, January 1). A Note on the Drag Due to Lift of Rectangular Wings of Low Aspect Ratio. https://ntrs.nasa.gov/citations/19930084097